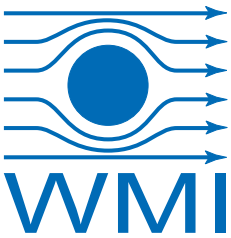

Interrelation of lattice, charge, and spin degrees of freedom in iron based systems

Dissertation

Andreas Christoph Baum

September 2018

Fakultät für Physik
Technische Universität München

TECHNISCHE UNIVERSITÄT MÜNCHEN

Fakultät für Physik
Lehrstuhl E23 für Technische Physik

Walther-Meißner-Institut für Tieftemperaturforschung
der Bayerischen Akademie der Wissenschaften

Interrelation of lattice, charge, and spin degrees of freedom in iron based systems

Andreas Christoph Baum

Vollständiger Abdruck der von der Fakultät für Physik der Technischen Universität München zur Erlangung des akademischen Grades eines

Doktors der Naturwissenschaften

genehmigten Dissertation.

Vorsitzender:		Prof. Dr. Wilhelm Zwerger
Prüfer der Dissertation:	1.	Priv.-Doz. Dr. Rudolf Hackl
	2.	Prof. Dr. Peter Böni

Die Dissertation wurde am 19.09.2018 bei der Technischen Universität München eingereicht und durch die Fakultät für Physik am 07.11.2018 angenommen.

Abstract

Magnetic order is a dominating phase in iron based pnictides and chalcogenides. Neither its origin nor its interplay with the neighbouring phases of nematic order and unconventional superconductivity are well understood yet. Raman spectroscopy allows access to the relevant excitations. This thesis focusses on the role of magnetism on lattice anomalies and the discrimination of localized and itinerant magnetic order. Simulations and experiments show that the magnetism in FeSe results from frustrated localized moments.

Kurzzusammenfassung

Magnetische Ordnung ist eine dominierende Phase in eisenbasierten Pniktiden und Chalcogeniden. Weder ihr Ursprung noch ihre Wechselwirkung mit den benachbarten Phasen der nematischen Ordnung und der unkonventionellen Supraleitung sind wohlverstanden. Raman-Spektroskopie erlaubt Zugang zu den relevanten Anregungen. Im Fokus dieser Arbeit stehen die Rolle des Magnetismus bei Gitteranomalien und die Unterscheidung von lokalisierter und itineranter magnetischer Ordnung. Simulationen und Experiment zeigen, dass der Magnetismus in FeSe von frustrierten lokalisierten Momenten stammt.

Contents

Chapter 1

Introduction

Since its discovery in the ancient world [1] magnetism has been one of the broadest fields of physical studies. Over the centuries ground-breaking work [2–9] has shown that electricity and magnetism are phenomena of the same interaction called electromagnetism. Still, the source of static magnetism in materials remained elusive. It was not until the early 20^{th} century that static magnetization was found to be a macroscopic quantum phenomenon [10, 11] whereby the magnetic moment on a microscopic basis is not only created by moving charges but also carried by elementary particles as an intrinsic property called spin [12, 13]. The spin was found to be a distinguishing feature, dividing elementary particles into bosons and fermions. Via the Pauli exclusion principle [14] and Hund's rules [15, 16] acting on the latter the spin state has direct consequences on the electronic configuration of atoms and condensed matter. With electrons being the main carriers of mobile charge and spin in solids it is no surprise that long range order of magnetic moments is commonly found in highly correlated materials, which are a major point of interest in contemporary solid state physics. There, magnetism is usually part of a rich phase diagram and both its origin and interrelation with nearby ordering phenomena including charge order or superconductivity are in the focus of research.

During the last ten years iron based systems (IBS) attracted major interest because several ordering phenomena can be studied. In materials such as $BaFe_2As_2$ atomic substitution of Ba by K, Fe by Co, and As by P as well as the application of hydrostatic pressure yield very similar phase diagrams [17–20]. Here, the pristine material develops magnetic order below T_{SDW} [21] which is accompanied by an orthorhombic distortion [22, 23]. Upon cobalt substitution the structural distortion at T_{s} starts to precede the magnetic order and a so called 'nematic phase' is created. Its name is taken from the nematic phase of liquid crystals where translational

symmetry persists but rotational symmetry is broken [24]. Several surprisingly large anisotropies were found below T_s [25–30]. Pinning down whether spin or charge order is the driving force of this phase and of the magnetic order that follows is an ongoing challenge. The third major player, superconductivity, arises when the magnetic and nematic order are suppressed by increasing the control parameter (substitution or pressure). This led to the conjecture that superconductivity and magnetism may be competing phenomena in IBS. However, spin fluctuations have emerged as a likely candidate for the interaction contributing to Cooper pairing [31–33].

In contrast to $BaFe_2As_2$, no universal phase diagram exists for the structurally simpler FeSe. The isovalent substitution of Se by Te and S, FeTe and FeS, yields entirely different materials. FeTe undergoes a combined magneto-structural transition at $T_N \approx 65\,K$, but is non-superconducting, whereas FeS remains tetragonal down to lowest temperatures [34] and has a critical temperature $T_c \approx 4\,K$ [35]. FeSe itself is already substantially different from $BaFe_2As_2$ in that the pristine material hosts a nematic phase below $T_s \approx 90\,K$ [36], but no long range magnetic order [36–38], and becomes superconducting below $T_c \approx 9\,K$ [39]. While in $BaFe_2As_2$ the suppression of magnetism seems to promote superconductivity [17–20] in FeSe the application of hydrostatic pressure causes a triplication of T_c [40] and the emergence of magnetic order at the same time [41, 42].

Yet, it is not only the interrelation of superconductivity and magnetism which remains poorly understood but also the magnetism itself:

(i) Various types of ordering vectors are observed across the families or even as a function of temperature [21, 43–46].

(ii) The magnetic moment observed experimentally is substantially different from the predicted one [47].

(iii) Most of the compounds seem to be best described in the weak-coupling limit where the band structure determines the ordering, whereas a few such as FeSe seem to require the existence of localized moments for understanding their properties. This is particularly surprising in a metal and motivated the notion of a Hund's metal [48–57] where the relative magnitudes of the Hubbard U and the Hund energy J_H are similar as opposed to physics of Mott type where the ratio of the hopping energy t and U determines the properties [58].

In a Hund's metal the interrelation of orbital and spin physics follows as a natural consequence, and implies that the strength of the localization of electrons from

different orbitals may be distinctly different. In the IBS, for instance, the electrons in the xy orbital experience an increasing degree of localization upon moving from LaFePO via $BaFe_2As_2$ and FeSe to FeTe, whereas the electrons in the xz and yz orbitals remain itinerant thus maintaining metallicity in all cases [59].

This material-dependent mixture of more localized and more itinerant electrons would naturally explain the elusiveness of the magnetism at least on a qualitative level. The question arises in which way it can be pinned down. Here all methods which can determine the degree of localization can be helpful. Whereas photoemission can determine the electron velocities on different orbitals [59], optical (IR) conductivity is more sensitive to the renormalization of the mass [60, 61]. Electronic Raman scattering measures a similar response function as IR and provides also some sensitivity in momentum space such as observed in the case of the cuprates [62]. In addition, the type of responses in weak-coupling and strong-coupling systems with magnetic order are fundamentally different resembling that of a superconductor [63] and of a Heisenberg magnet [64], respectively. In other words, Raman scattering provides a tool to access the degree of localization.

Beyond directly looking at the response from ordered - localized or itinerant - spins Raman scattering allows one to scrutinize the emerging magnetism via the analysis of the phonon response close to the various phase boundaries or cross-over lines and of resonance effects as a results of band reconstruction. It is the purpose of this study to explore and use the capabilities of light scattering for pinning down properties and aspects of magnetism in the IBS.

This thesis is arranged as follows: Chapter 2 gives an overview of the diverse group of IBS and highlights the properties of the compounds studied. In Chapter 3 the basics of Raman scattering, used as primary experimental method, are introduced. The corresponding set-up for inelastic light scattering, together with set-ups used for complementary measurements of the index of refraction and the magnetic susceptibility, is elucidated in Chapter 4. This chapter also presents details about the sample characterization and preparation. Chapter 5 depicts the results from the experiments which are then discussed in Chapter 6.

Chapter 2

The iron based systems

In 2006 the discovery of superconductivity in compounds containing iron [65] sparked first interest in the IBS. Two years later several new materials brought higher critical temperatures [66–70], reaching the prevailing record of 55 K for bulk IBS [71] and causing a hype [72–75] similar to that after the discovery of the cuprates 20 years before [76, 77]. In parallel the magnetic order of these compounds was studied and found to be of density-wave type [21, 43]. The main attention during the last years rested on the interplay of spin and orbital ordering and their role as the driving force for the magneto-structural transition [23, 25, 78–80]. At the same time FeSe drew interest because its comparably low T_c of 8 K [39] could be tripled by the application of pressure [40]. Additionally, magnetism and nematicity seemed to be well separated in FeSe [38, 81].

This chapter gives an overview over the properties of the IBS with a focus on $BaFe_2As_2$, FeS, and FeSe which were studied in this work.

2.1 Crystal structure and classification

All IBS share Fe-pnictide or Fe-chalcogenide layers [83]. The simplest taxonomy refers to their stoichiometry denoting, e.g., FeSe as 11 material and $BaFe_2As_2$ as Ba-122. Fig. 2.1 shows a selection of the big group of IBS. The quasi two-dimensional iron-pnictide or iron-chalcogenide layers are separated by spacer layers except for the 11 family. These iron layers dominate the electronic properties as the bands crossing the Fermi surface are composed of Fe 3d orbitals [84–86]. The spacer layers only determine whether the shape of the Fermi surface is rather two-dimensional, such as in the 1111 compounds, or more three dimensional for the 122 and 11 compounds [84, 85, 87]. The layered structure also brings about a clear anisotropy of in-plane

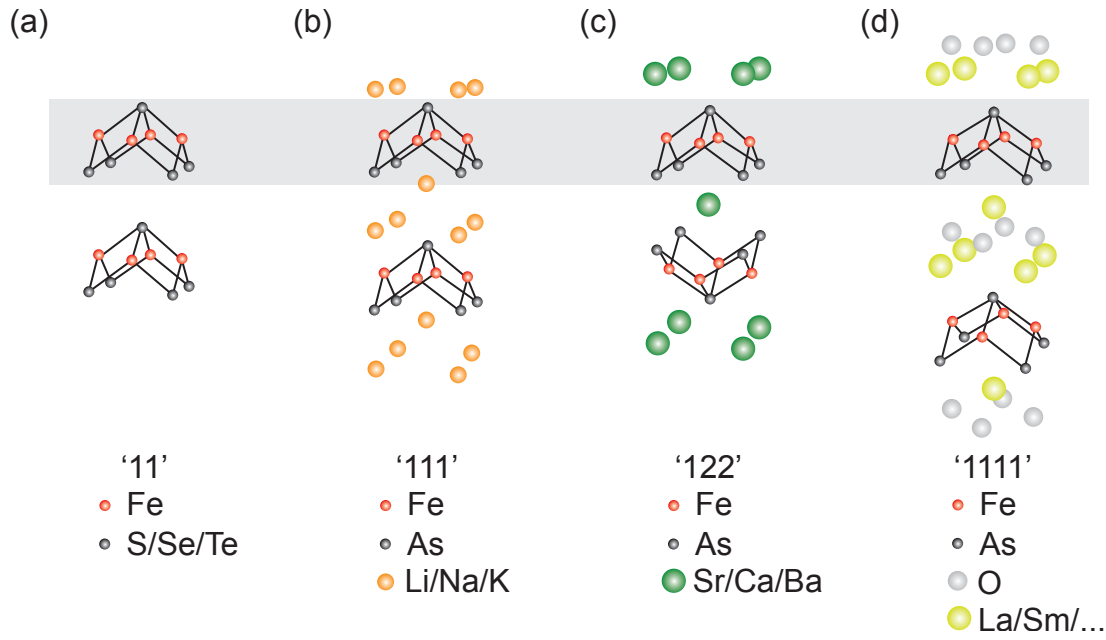

Figure 2.1: Crystal structures of the four main classes of IBS. The common Fe-pnictide/-chalcogenide layer is highlighted by the grey area. Adopted from Ref. [82].

and out-of-plane properties [88, 89], albeit the resistivity anisotropy is less than what is found in the cuprates [90]. Substitution of atoms as a control parameter is possible on almost any lattice site allowing, for example, the substitution of Fe by Co, As by P, or Ba by K in Ba-122, or of Se by Te or S in FeSe. As opposed to doped semiconductors the effect of non-isovalent substitution can not be simply viewed as injection of charge carriers [91]. Even for isovalent substitution the results may differ from the simple expectation of providing chemical pressure [92].

2.1.1 Unit cells and structural distortion

At room temperature almost all IBS exist in the tetragonal crystal structure (point group D_{4h}). Cases with excess Fe such as $Fe_{1+\beta}Se$ displaying hexagonal crystal symmetry shall be ignored here. The crystallographic unit cell contains two iron atoms and is called 2-Fe cell. Typical lattice constants are $a = b \approx 3.96\,\text{Å}$ and $c \approx 12.95\,\text{Å}$ for Ba-122 at room temperature [23]. The crystallographic unit cell is shown as green lines in Fig. 2.2(a). The 1-Fe cell, denoted by dashed red lines, is often sufficient when dealing with electronic properties, as the Fermi surface stems from bands made predominantly from Fe $3d$ orbitals [84–86]. A common feature of many IBS is a structural transition at low temperatures whereby the crystal transforms to an orthorhombic structure (point group D_{2h}). As shown in Fig. 2.2(b)

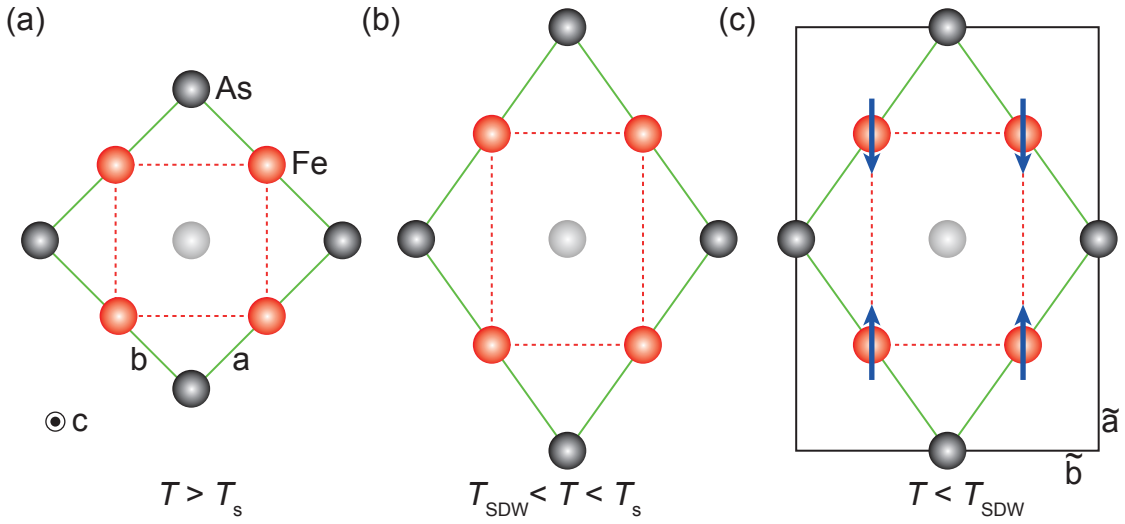

Figure 2.2: Unit cell of $BaFe_2As_2$ in the (a) tetragonal, (b) orthorhombic paramagnetic, and (c) $(\pi, 0)$ magnetically ordered state seen along the c axis. Red and grey spheres are Fe and As atoms, respectively. Blue arrows in panel (c) depict the $(\pi, 0)$ spin alignment. Red dashed lines denote the bonds between Fe atoms, green lines depict the crystallographic 2-Fe cell, and the black rectangle in panel (c) is the 4-Fe cell relevant in the magnetic phase. The orthorhombic distortion is strongly exaggerated.

this orthorhombic distortion does not occur along the main crystallographic axes (green lines) but along the bonds between the iron atoms (dashed red lines). Thus the new unit cell is rotated by 45° with respect to the high temperature 2-Fe unit cell. The relative change of lattice constants, $2\frac{\tilde{a}-\tilde{b}}{\tilde{a}+\tilde{b}}$, due to the structural transformation is less than 1% [23, 93] and can be considered small. However, the orthorhombic phase has shown significant anisotropies in the electronic properties and is often called a 'nematic phase'. In several compounds the structural transition is accompanied by or close to the onset of magnetic order, and the interrelation of nematic and magnetic ordering is still a matter of debate. The small orthorhombic distortion leads to the formation of twin domains below the transition temperature T_s. Between those domains the orientation of the $\tilde{a}$ and $\tilde{b}$ axes is swapped. As the domain size is on the order of 10 µm [94] all measurements lacking a finer spatial resolution yield properties averaged over the $\tilde{a} - \tilde{b}$ anisotropy. As was shown by resistivity measurements [25, 26], optical transport [27–29], and ARPES [30], sufficient detwinning of Ba-122 crystals can be achieved by the application of uniaxial pressure of the order of a few to some tens of mega pascal [95–97].

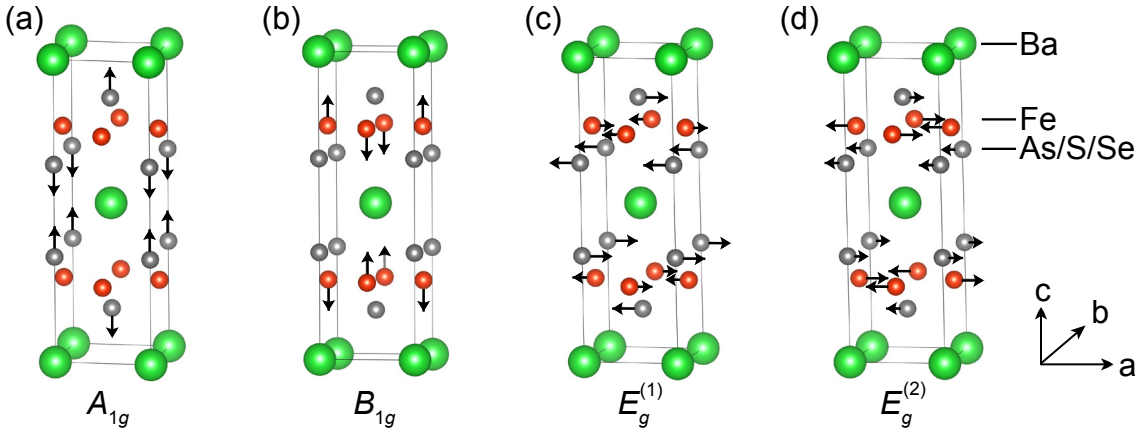

Figure 2.3: Raman active phonons in tetragonal $BaFe_2As_2$ [86]. The c-axis modes in (a) A_{1g} and (b) B_{1g} symmetry incorporate virtually solely pnictogen/chalcogen atoms or iron atoms, respectively. The E_g modes (c,d) are mixed shear vibrations of both types of atoms. Spacer atoms (Ba, green balls) are not involved in any Raman active phonon mode here. The depicted phonon modes are valid for 122-type and 11-type IBS.

2.1.2 Phonons

Raman active phonons reflect the similarities of the crystal structures of the IBS. The four modes for tetragonal $BaFe_2As_2$ are shown in Fig. 2.3. No mode involves the spacer layer since the Ba site is a centre of inversion. Hence, all four modes also exist in the 11-type IBS. The energies of the phonons depend on the sample stoichiometry. Two out of four modes have displacement patterns aligned parallel to the c axis and are dominated by displacements of one type of atoms. The A_{1g} mode involving pnictogen or chalcogen atoms modulates the height of this atoms above the iron plane and was found to couple strongly to the magnetic moment [98]. Hence, it exhibits several peculiarities when entering the magnetically ordered phase of Ba-122 as discussed in Sec. 6.1.2. The eigenvectors of the pnictogen/chalcogen and the iron c-axis modes are unaffected by the change in lattice symmetry at T_s. The mixed E_g modes are doubly degenerate. Upon entering the orthorhombic (D_{2h}) crystal structure this degeneracy is lifted and each E_g phonon splits into one B_{2g} and one B_{3g} mode. This splitting is part of this study (Sec. 6.1.2).

2.2 Phase diagrams

The diversity and proximity of several ordering phenomena are the most intriguing features of the iron based systems. Unlike the cuprates, there is no phase diagram

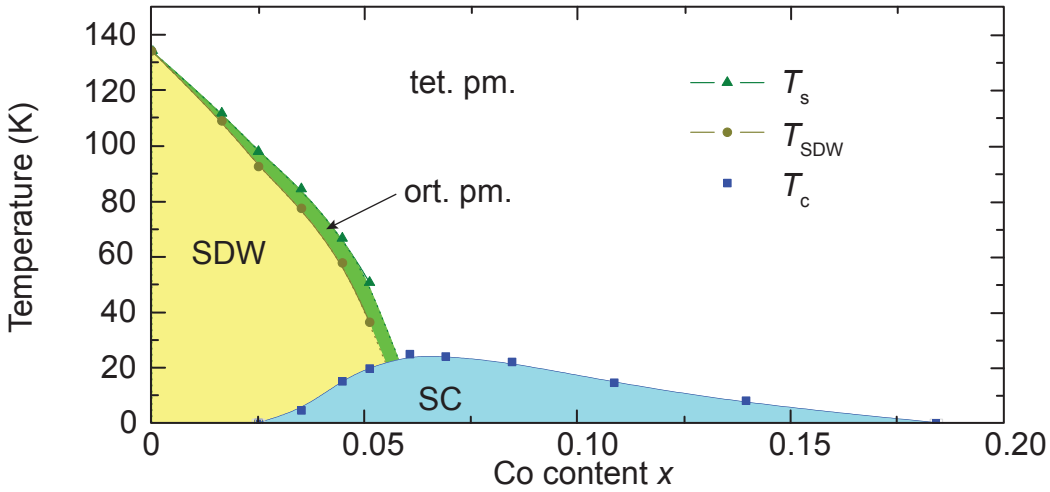

Figure 2.4: Phase diagram of $Ba(Fe_{1-x}Co_x)_2As_2$ adopted from Ref. [17]. The material undergoes a phase transition from the high temperature tetragonal paramagnetic phase (tet. pm.) to an orthorhombic paramagnetic phase (ort. pm., green area) below T_s and acquires a stripe-like magnetic order of SDW type (yellow area) below T_{SDW} for doping levels up to $x \approx 0.06$. Superconductivity (SC, blue area) is found for doping levels of $x \approx 0.025 - 0.18$ with a maximum T_c of 24 K at $x^{opt} \approx 0.06$.

which can be considered universal to all families of IBS. What some publications call "the phase diagram of iron pnictides" [59] is in fact the phase diagram of the Ba-122 compound. Even when focussing on this single material differences arise depending on the type of control parameter. In a coarse classification two groups of IBS can be found.

In one, the stoichiometric parent compounds are non-superconducting but instead order magnetically at low temperatures. The 122 and 1111 compounds belong to this group. Their parent compounds are tetragonal paramagnetic metals at room temperature. As an example comprising all relevant features the phase diagram of $Ba(Fe_{1-x}Co_x)_2As_2$ is shown in Fig. 2.4. When samples with a small control parameter x are cooled below a temperature T_s the crystal structure changes to orthorhombic and at $T_{SDW} \leq T_s$ magnetic stripe order of spin density wave (SDW, yellow area) type sets in. In the case of $T_{SDW} < T_s$ the orthorhombic paramagnetic phase in between is called the nematic phase (green). When the cobalt content is increased both nematic and magnetic order are suppressed. Above $x \approx 2\%$ superconductivity appears and reaches a maximum T_c at $x^{opt} \approx 6\%$ before being suppressed again. A similar phase diagram arises when substituting P for As [18] or K for Ba [19] as well as upon applying uniaxial [99] or hydrostatic [20] pressure.

It is this phase diagram (Fig. 2.4) that bears the most similarities with the

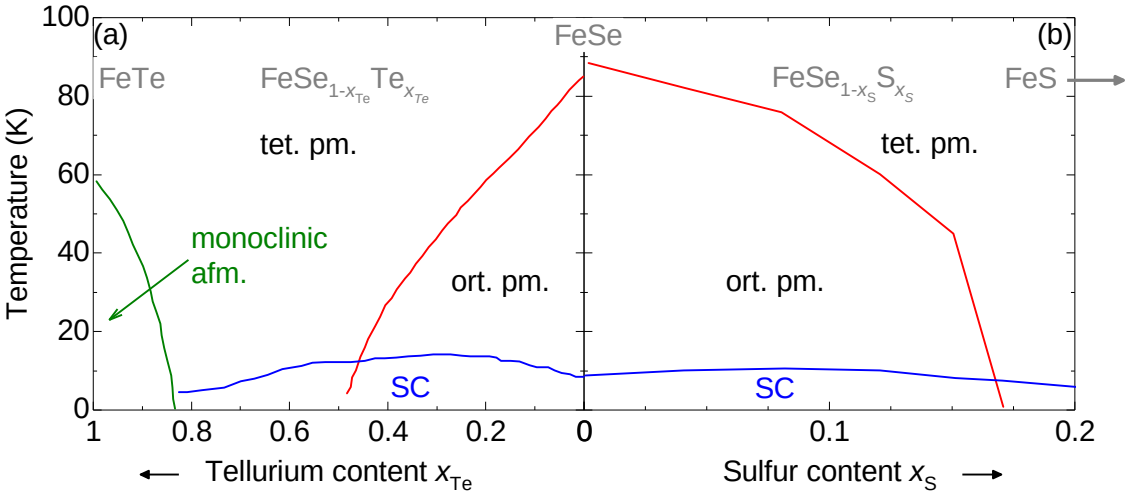

Figure 2.5: Phase diagram of iron chalcogenides representing substitution of selenium in FeSe by (a) tellurium and (b) sulphur. All compounds are tetragonal and paramagnetic (tet. pm.) at high temperatures. Pristine and slightly substituted FeSe exhibits an orthorhombic paramagnetic phase (ort. pm.) at low temperatures (red line). Superconductivity (SC) is found for all substitution levels below T_c (blue line) except for $x_{Te} \geq 0.8$, where at low temperatures the material is monoclinic and hosts antiferromagnetic order (green line). Note the different scales for (a) tellurium and (b) sulphur substitution. Data taken from (a) Ref. [103] and (b) Ref. [104]

cuprates in that superconductivity can arise from a magnetically ordered parent compound by atomic substitution and forms a dome-like structure with a maximum T_c at the optimal value x^{opt} of the control parameter. However, in cuprates the magnetic order is suppressed before superconductivity emerges [100] and the type of magnetic order found is rather different in cuprates and the 122-pnictides (see Secs. 2.4 and 6.2).

2.2.1 111 and 11 compounds

In the second group of IBS, comprising the 111 pnictides such as LiFeAs and the 11 chalcogenides (FeSe, FeTe, FeS), superconductivity can be found already in the stoichiometric parent compounds, with the exception of FeTe. The change of T_c upon increasing the control parameter is not universal but depends on the material and the type of parameter. In LiFeAs substitution of Fe by Co drastically reduces T_c [101]. Application of hydrostatic pressure p to NaFeAs leads to a slight increase of T_c up to $p = 3\,\mathrm{GPa}$ followed by a strong suppression when the pressure is increased further [102].

The case is even more complex in the 11 systems. Out of three undoped com-

pounds only FeSe and FeS exhibit superconductivity, at $T_c^{Se} = 9\,K$ [39] and $T_c^{S} \approx 5\,K$ [35], respectively. FeSe, being the most studied of the three, is considered as a quasi parent compound. As shown in Fig. 2.5 pristine FeSe exhibits a structural transition from a tetragonal to an orthorhombic crystal structure at $T_s \approx 90\,K$ but no long range magnetic order down to 4.2 K [38, 105]. Substitution of Se by either S or Te suppresses the orthorhombic nematic phase but enhances superconductivity to slightly higher $T_c^{max,S} \approx 10\,K$ and $T_c^{max,Te} \approx 14\,K$, respectively, before suppressing it again. FeTe is non-superconducting but undergoes a transition from a paramagnetic tetragonal state to a monoclinic structure hosting a double-stripe antiferromagnetic order below $T_N \approx 65\,K$ [44, 45, 106–108]. Pristine FeS, on the other hand, is superconducting below $T_c^{S} \approx 5\,K$ [35] and remains tetragonal down to low temperature [34]. Reports on long range magnetic order in FeS are controversial [35, 109–112].

2.2.2 Fluctuations

Above T_s fluctuations are a common phenomenon in IBS. Mainly studied in the Ba-122 compounds [31, 113–122], the response from fluctuations found by Raman spectroscopy covers a broad region extending up to $T_f \approx 220\,K$ in pristine $BaFe_2As_2$ [118]. Though not a phase in the strict thermodynamic sense this zone is of particular interest regarding the study of the corresponding ordered phases found below. The nature of these fluctuations was discussed in the context of the dichotomy between charge [116, 119, 123, 124] and spin order [31, 117, 118, 120, 125]. In FeSe a similar response was found in the Raman spectra and was associated to charge-nematic fluctuations [126].

2.3 Nematicity

A peculiarity of several IBS is the so called nematic phase where the crystal changes to an orthorhombic structure but no long-range magnetic order is established. The nematic order breaks rotational symmetry while maintaining translational symmetry [24]. While anisotropies are expected in an orthorhombic crystal, these are expected to be minor due to the small change in the lattice constants ($2\frac{\tilde{a}-\tilde{b}}{\tilde{a}+\tilde{b}} < 1\%$) [23, 25, 93]. Rather the main effect occurs in the electronic properties. Measurements of the resistivity on de-twinned crystals of Ba-122 reveal an anisotropy between $\tilde{a}$ and $\tilde{b}$ of 40 %, which sets in already above T_s and may reach 100 % at low temperatures in

the SDW phase [25]. In addition, the resistivity is higher along the shorter $\tilde{b}$ axis in contrast to what is expected given that the overlap of orbitals is higher along the shorter axis [25]. ARPES measurements on similarly de-twinned samples found an anisotropy of the bands at the X and Y point, caused by different shifts in energy of the d_{xz} and d_{yz} orbitals [30]. Experimentally access to the anisotropic properties of the nematic phase is hampered by the formation of dense crystal twins due to the concomitant orthorhombic distortion [94]. While the crystals can be de-twinned easily by the application of moderate uniaxial stress [25, 127] it was found that its effect on the rather soft materials [128] exceeds the simple de-twinning and also causes a shift [95, 129] and splitting [97] of the transition temperatures T_s and T_SDW. Strong uniaxial pressure was even found to serve as control parameter within the phase diagram [99]. All effects observed on stressed samples, especially if found at temperatures above the ordered phases, need to be evaluated carefully with respect to their possible origin from the applied pressure. The nematic phase appears in the 1111-compounds [130], Pt-substituted Sr-122 [131], and Co-substituted Ca-122 [132] and Ba-122 [133] as a precursor to the magnetic ordering when the temperature is lowered. This and its similar suppression upon increased substitution gave rise to the question as of whether magnetic or orbital ordering is the driving force of these intimately linked phases. In the case of stoichiometric FeSe only a nematic phase exists below $T_\mathrm{s} \approx 90\,\mathrm{K}$.

2.4 Magnetic order

Magnetic order in the vicinity of superconductivity with possibly high critical temperatures seems to be a universal feature of unconventional superconductors. While the exact interaction between magnetism and the nearby phases is still elusive, it is obvious that clarifying the nature of the magnetic order is an important piece of the puzzle. To this end the IBS provide a broad experimental ground.

The magnetism in IBS is diverse by itself [134] with different types of order found experimentally [21, 43–45] and more suggested to be energetically close [46, 135–137] as shown in Fig. 2.6. The most important types of magnetic order are shown as insets. Undoped and underdoped 122 and 1111 compounds host a $(\pi, 0)$ ordered phase below $T_\mathrm{SDW} \leq T_\mathrm{s}$ (cf. Fig. 2.4) with the spins aligned antiferromagnetically along the longer $\tilde{a}$ and ferro-magnetically along the shorter $\tilde{b}$ axis [21, 43]. This magnetic order was identified as a spin density wave (SDW) [23], i.e. originating in an instability of the Fermi surface [138] caused by nesting between the hole-like bands around the

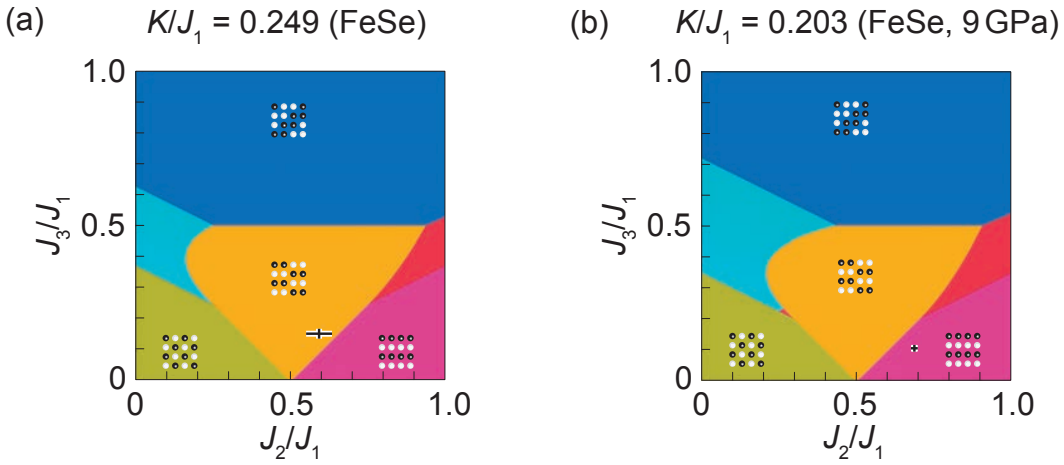

Figure 2.6: Magnetic phase diagram of 11 chalcogenides in the $J_1 - J_2 - J_3 - K$ model from Ref. [46]. White and black spheres in the insets depict spin up and down, respectively. The crosses mark the set of parameters determined for (a) FeSe and (b) FeSe at a hydrostatic pressure of 9 GPa. Light blue and red mark spiral configurations which are disregarded here.

Γ point and the electron-like bands around the X and Y points [117, 139]. Signs of the density wave formation appearing in spectroscopic measurements at low energies include the formation of a gap [113, 140], although the material remains metallic at all temperatures above T_c [23, 25, 141, 142]. In this picture the 122 compounds could be seen as prototypical materials for itinerant magnetism. However, spectroscopical features at higher energy were interpreted as response from localized spins [115, 143] and were treated on the basis of an anisotropic Heisenberg model [144]. In principle, both itinerant and localized magnetism may coexist. It was suggested that the SDW competes with superconductivity by gapping out parts of the Fermi surface [145]. Upon increasing the control parameter x the nesting is diminished and the SDW is suppressed, facilitating the emergence of superconductivity. In detail the interplay of magnetic order and superconductivity is more involved as both phases coexist in a small doping range [146, 147] and additional phases were found where tetragonal lattice symmetry is restored within the magnetic phase [147, 148]. Regarding the relationship between magnetic order and the lattice a strong coupling of the iron magnetic moment to the z position of the As atoms was found [98, 149]. This intimate relationship is confirmed by the existence of several phonon anomalies at and below T_{SDW} [97, 113, 150–152]. Two of these anomalies are subject to this thesis in Sec. 6.1.2.

The 11 chalcogenides are found closer to localized magnetism. Their magnetic order appears less uniform when tuning through the phase diagram (Fig. 2.5).

FeTe below $T_N \approx 65\,K$ hosts magnetism with an ordering vector of $(\pi/2, \pi/2)$ [44, 45, 106, 107], also called double stripe order. Raman spectra of FeTe show a broad high-energy feature similar to what was interpreted as two-magnon peak in $BaFe_2As_2$ [115, 143]. In pristine FeSe no long-range magnetic order was found down to lowest temperatures [36–38]. However, recent neutron scattering experiments and the results presented within this thesis (Ref. [153] and Sec. 6.2) suggest that the magnetic ground state of FeSe is a $(\pi, 0)$ order of localized spins whereby the emergence of long-range order is suppressed by frustration. For the newest member of the 11-systems, FeS, the existence of putative magnetic order is still unsettled. While some studies found no magnetic order [35, 109], two μSR experiments [110, 111] report short-range order below $T^* \approx 20\,K$, which even may coexist with superconductivity. Recently, neutron scattering provided evidence for magnetic order below $T_N \approx 120\,K$ [112]. Raman scattering data on phonons obtained during this work (see Sec. 6.1.1 and Ref. [154]) are compatible with a transition at T^*. Still, the precise magnetic state of tetragonal iron sulphide is a matter of ongoing research.

2.5 Superconductivity

The finding of high-temperature superconductivity in the iron based systems spurred the interest in these materials. Superconductivity in IBS was first found in 1996 [155], but remained largely unknown until the publication by Kamihara *et al.* [65] ten years later. While the T_c of 6 K did not seem impressive, the mere existence of superconductivity in a material containing iron already was seen as a surprise [72]. Then, in 2008, the finding of $T_c \approx 26\,K$ in doped $LaO_{1-x}F_xFeAs$ triggered a rapid series of discoveries, including $T_c > 40\,K$ in La-1111 [68] and Sm-1111 [69], and the synthesis of $Ba_{0.6}K_{0.4}Fe_2As_2$ having $T_c \approx 38\,K$ [67]. To date the highest $T_c \approx 56\,K$ in bulk IBS is found in Sm-substituted SrFeAsF [156] and makes the IBS second only to cuprates in the quest for ever higher critical temperatures. In single layer FeSe on $SrTiO_3$ T_c as high as 100 K was reported [157, 157].

The search for the 'superconducting glue' in IBS mainly revolves around the question regarding the symmetry of the pairing interaction and, correspondingly, of the gap [31, 74, 158]. Superconductivity based solely on electron-phonon interaction was ruled out already by early theoretical works [159, 160] as it could not explain the high critical temperatures. Reports on the gap symmetry range from s-wave in Ba-122 compounds [145], Te-substituted FeSe [161], potassium intercalated FeSe [162], and FeS [110], over combined $s + d$-wave in FeS [163], to d-wave in KFe_2As_2

[164–166] and FeS [167, 168]. This indicates that superconductivity in IBS is also a complex phenomenon along the lines of the diverse phase diagram. Recent studies of the Ba-122 materials found Bardasis-Schrieffer in-gap modes [169] which provide evidence for sub-dominant interactions of significant strength [31, 32, 120, 169, 170]. The study of these modes as a function of potassium substitution brought about some systematics and, combined with fRG and RPA calculations, was interpreted as a signature of superconductivity mediated by spin fluctuations [31, 32]. Though no 'smoking gun' experiment exists so far, this mechanism emerged as a likely candidate over the last years [33, 83, 171, 172] and accentuates the importance of understanding magnetic interactions in the IBS in general [173].

Chapter 3

Raman spectroscopy

Multiple methods are employed to investigate highly correlated systems such as the cuprate superconductors and the IBS. Raman spectroscopy contributes by accessing phonons, magnetic and electronic excitations over a wide energy range and by offering symmetry selection rules. In this chapter the essential properties of Raman spectroscopy relevant to the evaluation of the data acquired in this work will be pointed out. A more thorough treatment of Raman scattering from correlated systems can be found in Ref. [174].

3.1 Principle

Raman scattering denotes the inelastic scattering of light from matter. First predicted by Smekal in 1923 [175] and treated on a quantum mechanical basis by Kramers and Heisenberg [176] in 1925, the experimental realization was achieved by Landsberg and Mandelstam in crystals in 1928 [177], and by Raman and Krishnan in liquids almost simultaneously [178]. The basic principle of Raman scattering is shown in Fig. 3.1. The incident photon of energy ω_i and momentum $\mathbf{k}_\mathrm{i}$ is absorbed, thus exciting the electronic system from its initial state $|I\rangle$ to an intermediate state $|\nu\rangle$. This state can couple to the low energy excitations such as phonons and magnons, creating or destroying such an excitation of energy Ω and transitioning to a second intermediate state $|\nu'\rangle$ from which the system relaxes to its final state $|F\rangle$ by emission of the scattered photon (ω_s,$\mathbf{k}_\mathrm{s}$). The creation of an excitation is called Stokes process, as shown in Fig. 3.1(a), whereby the emitted photon is red-shifted with respect to the incident photon. The second case of annihilating an excitation is denoted Anti-Stokes process and yields a scattered photon at higher energy. In both cases the momentum $\mathbf{q}$ transferred to the sample can be considered

small given that the wavelength of the light is approximately 1000 times the size of a unit cell, hence several unit cells are excited in phase. This limits first order Raman scattering to a region $q = |\mathbf{q}| \approx 0$ near the Γ point of the Brillouin zone.

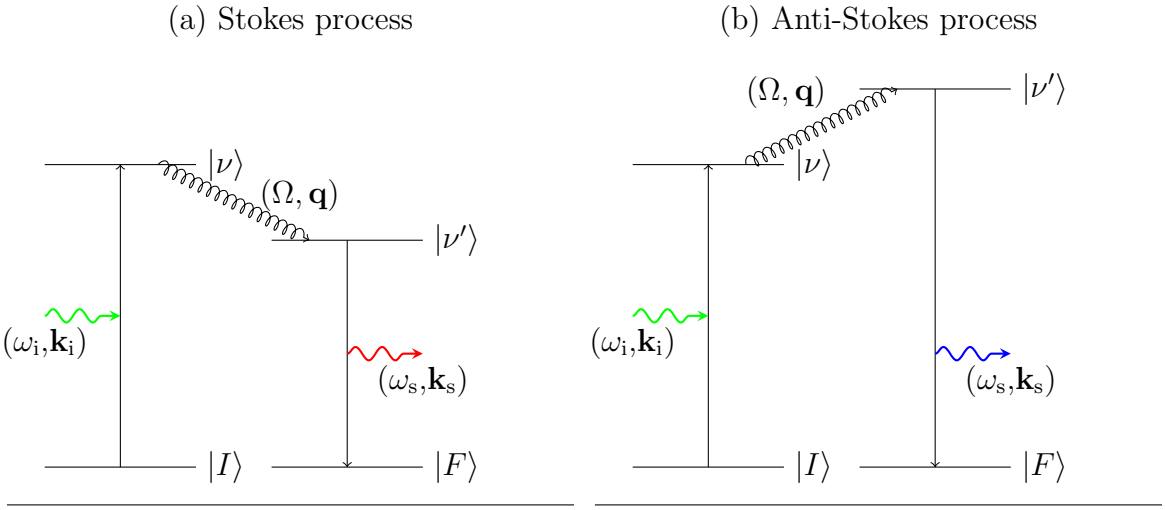

Figure 3.1: Simplified scheme of a Raman scattering process. The incident photon $(\omega_\mathrm{i},\mathbf{k}_\mathrm{i})$ (green sinuous line) excites the system from its initial state $|I\rangle$ to an intermediate state $|\nu\rangle$. By either (a) creating or (b) destroying an excitation $(\Omega, \mathbf{q})$ (curled line) the system transitions to a second intermediate state $|\nu'\rangle$, and relaxes to its final state $|F\rangle$ by emission of a (a) red- or (b) blue-shifted photon $(\omega_\mathrm{s},\mathbf{k}_\mathrm{s})$.

The involvement of two dipole transitions $|I\rangle \rightarrow |\nu\rangle$ and $|\nu'\rangle \rightarrow |F\rangle$ is the basis of the Raman selection rules and differentiates between Raman scattering and measurements of the optical conductivity, where only one photon is absorbed.

One particular case merits a more detailed consideration. In general the intermediate states $|\nu\rangle$ and $|\nu'\rangle$ are virtual states, existing only for a very short time within uncertainty, but can also be eigenstates of the system. From the viewpoint of second order perturbation theory [179] an energy denominator is involved for every transition which becomes zero if the transition occurs between electronic eigenstates of the system. This causes the scattering tensor, which governs the scattering intensity, to diverge, and provides some sensitivity to the electronic structure of the sample by determining the resonance behaviour of different excitations. To this end the energy of the incident light ω_i needs to be tuned over the appropriate range. The matrix element governing the scattering process can be written as [180]

$$M_\mathrm{FI}^{is} \propto \sum_{\nu,\nu'} \frac{\langle F|H_\mathrm{exR}|\nu'\rangle \langle \nu'|H_\mathrm{exL}|\nu\rangle \langle \nu|H_\mathrm{exR}|I\rangle}{(\omega_\mathrm{s} - E_{\nu'})(\omega_\mathrm{i} - E_\nu)} \tag{3.1}$$

Here $E_{\nu'}$ and E_{ν} are the respective energies of the intermediate states $|\nu'\rangle$ and $|\nu\rangle$, respectively. H_{exR} and H_{exL} are the respective parts of the Hamiltonian governing the coupling to the light and to the excitation Ω. Eq. 3.1 shows that the cross section can be enhanced for matching energies of both the incident and the scattered photons.

From the experimental point of view the scattered light is analysed as a function of the Raman shift, $\Omega = \omega_{\mathrm{i}} - \omega_{\mathrm{s}}$.

3.2 Raman matrix elements and selection rules

The scattering process is described by the probability for an incident photon of momentum $\mathbf{k}_{\mathrm{i}}$, energy ω_{i}, and polarization $\mathbf{e}_{\mathrm{i}}$, $|\mathbf{k}_{\mathrm{i}}, \omega_{\mathrm{i}}, \mathbf{e}_{\mathrm{i}}\rangle$, to be scattered into a solid angle interval $\left[\tilde{\Omega}_{\mathrm{s}}, \tilde{\Omega}_{\mathrm{s}} + \Delta\tilde{\Omega}_{\mathrm{s}}\right]$ and energy range $[\omega_{\mathrm{s}}, \omega_{\mathrm{s}} + \Delta\omega_{\mathrm{s}}]$. This probability corresponds to a transition rate given by Fermi's golden rule and is expressed in terms of the differential cross section [174],

$$\frac{\partial^2\sigma_{is}}{\partial\tilde{\Omega}_{\mathrm{s}}\partial\omega_{\mathrm{s}}} = \hbar r_0^2 \frac{\omega_{\mathrm{s}}}{\omega_{\mathrm{i}}} \frac{1}{Z} \sum_{I,F} e^{-\frac{E_{\mathrm{I}}}{k_{\mathrm{B}}T}} \left|M_{\mathrm{FI}}^{is}\right|^2 \delta(E_{\mathrm{F}} - E_{\mathrm{I}} - \hbar\Omega) \tag{3.2}$$

with Z the partition function, r_0 the classical electron radius, and $E_{\mathrm{I,F}}$ the energies of the initial and final state $|I\rangle$ and $|F\rangle$, respectively. M_{FI}^{is} contains all information about the initial, final, and intermediate states, as well as the energies and polarizations of the incident and scattered light. Typically simplifications are needed to facilitate calculations. Often only the transition from the initial state $|I\rangle$ to the final state $|F\rangle$ is considered and can be written either as a structure factor S or as a susceptibility χ''_{is},

$$\frac{\partial^2\sigma_{is}}{\partial\tilde{\Omega}_{\mathrm{s}}\partial\omega_{\mathrm{s}}} = -\hbar r_0^2 \frac{\omega_{\mathrm{s}}}{\omega_{\mathrm{i}}} \frac{1}{\pi} \underbrace{\{1 + n(\Omega, T)\}\, \chi''_{is}}_{S}. \tag{3.3}$$

For the As phonon in $BaFe_2As_2$ (Sec. 6.1.2) the resonant behaviour is pivotal. The corresponding calculation of the Raman tensor will be discussed there. The relationship between the quantities measured in the experiment and the differential cross section will be established in the next section. χ''_{is} is composed of two parts whereby one governs the spectral shape and the second one comprises the polarization dependent selection rules. These selection rules govern the projection of different symmetries by choice of polarization for the incident and scattered light.

A convenient notation is a 3×3 matrix called Raman tensor $\hat{\alpha}$. The form of this tensor is tabulated for different point groups in Ref. [179]. For a given $\hat{\alpha}$ the relative intensity projected for a set of polarizations ($\mathbf{e}_\mathrm{i}$,$\mathbf{e}_\mathrm{s}$) is

$$I_{is} \propto \left|\mathbf{e}_\mathrm{s}^* \cdot \hat{\alpha} \cdot \mathbf{e}_\mathrm{i}\right|^2 . \tag{3.4}$$

Phonons are projected when their symmetry matches the projected symmetry. In the case of electronic excitations [174], fluctuations [181], and magnons [64] a momentum-dependent form factor has to be included.

It is important to note that the relevant coordinate system of the polarizations is given by the sample unit cell. Therefore within this thesis the polarizations are given in Porto notation ($\mathbf{e}_\mathrm{i}$,$\mathbf{e}_\mathrm{s}$), whereby $\mathbf{e}_\mathrm{i}$ and $\mathbf{e}_\mathrm{s}$ are given by the unit cell axes introduced in Fig. 2.2. Switching between the 1-Fe/4-Fe cell and the 2-Fe cell permutes the projection of B_{1g} and B_{2g} symmetry for the same polarization settings, but has no influence on the projection of the A symmetries as can be seen from Fig. 3.2.

3.3 Intensity calibration

As shown in the previous section the quantity of interest χ''_{is} is directly linked to the differential cross section which is accessible experimentally. In the experiment the data are acquired as a count rate $\dot{N}^*_{is}$ for a certain wavelength of the scattered light. This count rate originates from the rate of photons scattered from the focal area A_foc where a laser power $P_\mathrm{i} = I_\mathrm{i}\hbar\omega_\mathrm{i}$ is absorbed. This photon rate is measured by an instrument having a resolution $\Delta\omega_\mathrm{s}$, angle of acceptance $\Delta\tilde{\Omega}$, and efficiency $r(\omega_\mathrm{s})$. The indices i, s denoting properties for incident and scattered light refer to both a dependence on energy and polarization.

In general the rate of scattered photons is given by the rate of incident photons multiplied by the probability for a scattering event to occur. The latter is governed by the total cross section σ_{is} assigning a 'target area' to each scatterer, of which N_T exist in the illuminated area A_foc. Experimentally the rate of detected photons is the observed quantity and thus the efficiency of the instrument $r(\omega_\mathrm{s})$ is included. The observed count rate is given by the differential cross section multiplied by the instrument resolution and angle of acceptance and the rate of incident photons is

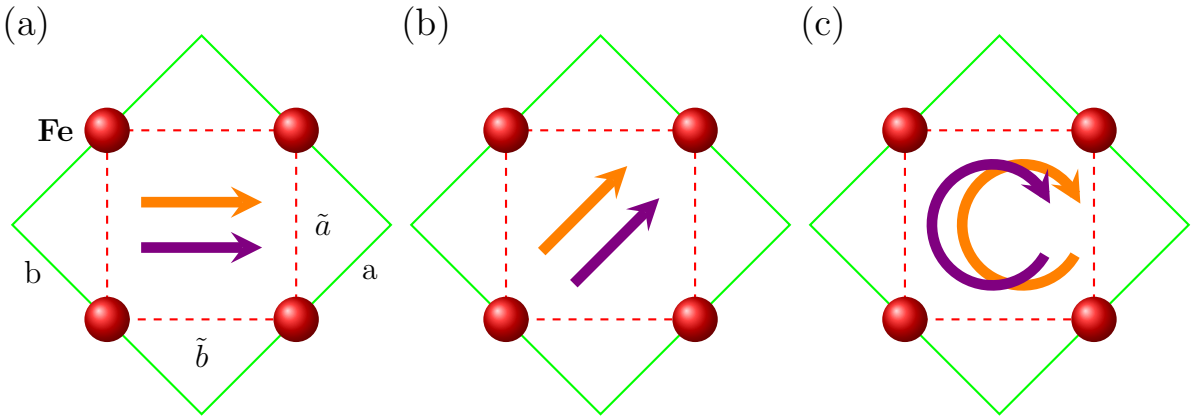

	(a)	(b)	(c)
1-Fe/4-Fe:	A_{1g} $+B_{1g}$	A_{1g} $+B_{2g}$	A_{1g} $+A_{2g}$
2-Fe:	A_{1g} $+B_{2g}$	A_{1g} $+B_{1g}$	A_{1g} $+A_{2g}$

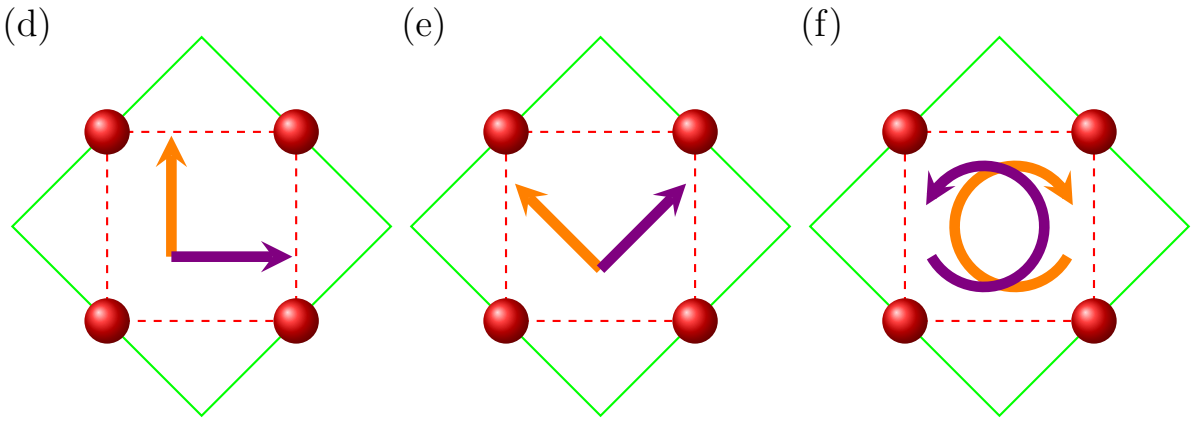

	(d)	(e)	(f)
1-Fe/4-Fe:	A_{2g} $+B_{2g}$	A_{2g} $+B_{1g}$	B_{1g} $+B_{2g}$
2-Fe:	A_{2g} $+B_{1g}$	A_{2g} $+B_{2g}$	B_{1g} $+B_{2g}$

Figure 3.2: Raman selection rules in tetragonal IBS. Red spheres represent iron atoms. The unit cell containing 1-Fe atom is shown as dashed red line, the crystallographic cell comprising 2-Fe atoms as solid green line. The polarizations of the incident and scattered light, $\mathbf{e}_\mathrm{i}$ and $\mathbf{e}_\mathrm{s}$, are denoted by violet and orange arrows, respectively. As the system is tetragonal rotating linear polarizations by 90° or permuting left and right circular polarization, for both the incident and scattered light in each case, does not change the selection rules. Figure adopted from Ref. [97].

given by the laser power as

$$\dot{N}^*_{is}(\Omega,T) = \frac{\partial^2\sigma_{is}(\Omega,T)}{\partial\tilde{\Omega}_\mathrm{s}\partial\omega_\mathrm{s}} \underbrace{\Delta\omega_\mathrm{s}\Delta\tilde{\Omega}_\mathrm{s}\cdot r(\omega_\mathrm{s})}_{s(\omega_\mathrm{s})\Delta\omega_\mathrm{s}(\omega_0)\Delta\tilde{\Omega}(\omega_0)} \cdot N_\mathrm{T}\cdot\frac{P_\mathrm{i}}{A_\mathrm{foc}\hbar\omega_\mathrm{i}}. \tag{3.5}$$

The energy-dependent sensitivity of the instrument $s(\omega_\mathrm{s}) = r(\omega_\mathrm{s})\frac{\Delta\omega_\mathrm{s}\Delta\tilde{\Omega}(\omega_\mathrm{s})}{\Delta\omega_\mathrm{s}(\omega_0)\Delta\tilde{\Omega}(\omega_0)}$ was determined by calibration. It was approximated by a polynomial of 5^{th} order and is used to correct the data [182]. After the installation of a new CCD it was updated as shown in Appendix B. The sensitivity is normalized to unity at $\omega_0 = 408\,\mathrm{nm}$ and 640 nm. In the next step the differential cross section is replaced by the Raman susceptibility according to Eq. 3.3, and Eq. 3.5 is converted to

$$\dot{N}^*_{is}(\Omega,T) = \underbrace{-\frac{r_0^2 N_\mathrm{T}}{\pi\cdot A_\mathrm{f}}\Delta\omega_\mathrm{s}(\omega_0)\Delta\tilde{\Omega}_\mathrm{s}(\omega_0)}_{R}\cdot\chi''_{is}(\Omega,T)\cdot\frac{\omega_\mathrm{s}}{\omega_\mathrm{i}^2}\cdot P_\mathrm{i}\cdot s(\omega_\mathrm{s})\cdot\{1+n(\Omega,T)\}\,. \tag{3.6}$$

Additionally dividing by $\tilde{\omega} = 20\,000\,\mathrm{cm}^{-1}$ allows for corrections close to unity. After including the temperature- and energy-independent factors in a constant R the relationship between the count rate and the Raman susceptibility is obtained as

$$R\chi''_{is}(\Omega,T) = \frac{\dot{N}^*_\mathrm{is}}{P_\mathrm{i}\cdot s(\omega_\mathrm{s})}\frac{\omega_\mathrm{i}^2}{\omega_\mathrm{s}\tilde{\omega}}\left\{1-\exp\left(-\frac{\hbar\Omega}{k_\mathrm{B}T}\right)\right\}. \tag{3.7}$$

Chapter 4

Experimental set-up and sample preparation

4.1 Spectroscopic set-up

The set-up as shown in Fig. 4.1 shows all parts required to ensure the quality of the incident beam and sufficient filtering on the scattered light side.

Today's light source of choice for spectroscopy are ion gas lasers and solid state lasers. The latter excel in cost efficiency but are usually limited to single wavelength operation. For this reason most measurements during this work were performed using a diode pumped solid state laser of model Coherent Genesis MX SLM emitting at $\lambda_\mathrm{i} = 575\,\mathrm{nm}$. Additionally an Ar^+-Ion laser (Coherent Innova 304C) provides five lines in the range from 458 nm to 514 nm. To facilitate the full range resonance analysis of the A_{1g} phonon in $BaFe_2As_2$ (Sec. 6.1) a Kr^+-Ion laser (Coherent Innova 400) was used allowing for measurements in the deep blue (407 nm and 413 nm) and red (647 nm and 676 nm) colour range. In 2017 a Laser Quantum Ignis solid state laser emitting at $\lambda_\mathrm{i} = 660\,\mathrm{nm}$ was employed for measurements in the red colour range. The beam from each laser is expanded to the same diameter of approximately 2.5 mm and redirected on a common optical axis using mirrors M1 and M1′, respectively. The spatial filter (SP1) with its 30 µm pinhole removes off-axis portions of the beam. The prism monochromator (PMC) in combination with the second spatial filter (SP2) serves as a single stage spectrometer to filter lines from plasma excitations in the ion lasers. The polarization of the incident laser beam is selected by means of a polarizer (P1) and a Soleil-Babinet compensator (SB), the combination of which facilitates the generation of any polarization via the variable phase shift between ordinary and extraordinary direction in the compensator. The

$\lambda/2$ plate in front of (P1) is used for setting the power of the beam by rotating its polarization relative to (P1), making use of the fact that the laser beam is already polarized (100:1). The power is measured using a photo detector power meter (PM) (Gentec Maestro with a PH100-Si-UV photodetector) after lens (L1).

The polarized beam is again spatially filtered (SP3) and focused by lens (L1) ($f = 240\,\mathrm{mm}$) into a spot of roughly $50 \times 100\,\mu\mathrm{m}$ on the sample. Mirror (M4) can be tilted in two directions to position the laser spot on the sample surface. The sample is mounted on a sample holder the details of which are described in Ref. [97]. The sample holder is mounted inside a continuous-flow ^{4}He cryostat and can be set to temperatures from 2 K to 350 K. All samples studied within this thesis were mounted with their c axis parallel to the lab z axis pointing towards the spectrometer. The samples were cleaved in air. After closing and pumping the cryostat the vacuum was better than $10^{-3}\,\mathrm{mbar}$ within 2 min.

Scattered light from the sample is collected by an objective lens (O1, $f/1.4$). The desired polarization is selected via a $\lambda/4$ retarder and a polarizer (P2). The $\lambda/2$ waveplate rotates the light into the direction of highest efficiency of the spectrometer (x direction). The light is focused on the entrance slit (SL1) of the spectrometer (Jarrell-Ash 25-100 double monochromator equipped with 2400 gr/mm gratings). The resolution of the spectrometer operated in subtractive mode is given by the width M of the intermediate slit (SL2). The absolute wavelength of the transmitted light is chosen by the rotation angle of the gratings which are positioned via a sine drive [183] powered by a stepper motor. The computer interface to this drive is described in Ref. [97].

The light leaving the exit slit is focussed onto the CCD chip by lens (L2) and objective lens (O2). The spot on the CCD thus integrates the information from the transmitted spectrum $\omega_\mathrm{s} \pm \frac{\Delta\omega_\mathrm{s}}{2}$ where ω_s is given by the grating position and $\Delta\omega_\mathrm{s}$ is the bandwidth transmitted through M at ω_s. The typical setting for the CCD thus involves binning the full area of the spot to a single superpixel yielding the desired count rate. The unilluminated part of the CCD chip is used for background correction. Both CCD and spectrometer are controlled by a computer program. The output of this program is the count rate $\dot{N}^*_{is}$ as a function of the Raman shift with respect to the laser line measured and needs to be corrected as described in Sec. 3.3.

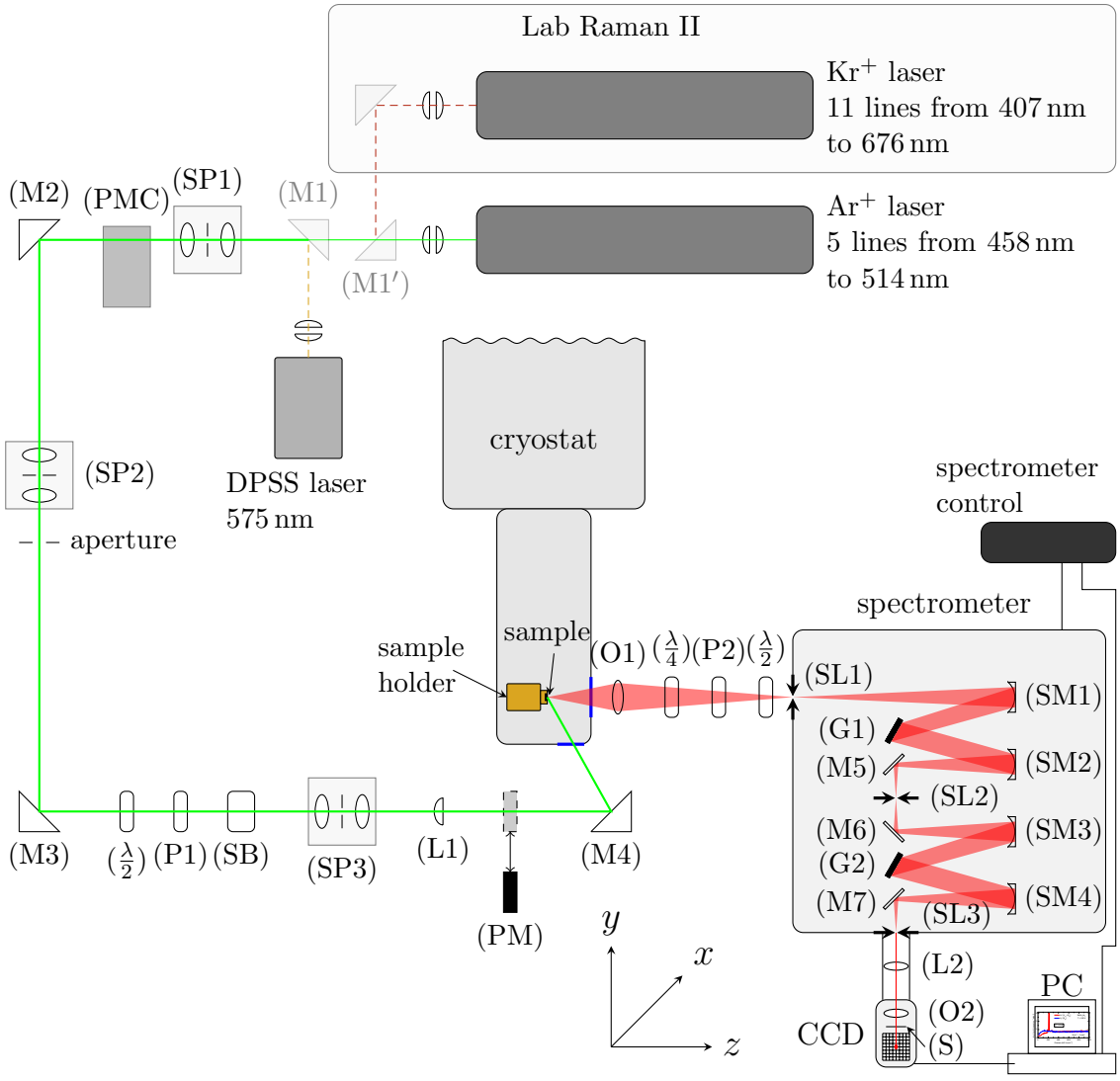

Figure 4.1: Optical set-up of the lab Raman I. The light (green line) from the chosen laser is spatially and frequency filtered, and polarized before being focussed onto the sample. The scattered light (red) is collected, selected by polarization, and spectrally filtered before being measured by the CCD detector.
(M1-7) mirrors; (SP1-3) spatial filters; (PMC) prism monochromator; (P1,2) polarizers; ($\lambda/_{2,4}$) half-/quarter-wave plates; (O1,2) objectives; (L1,2) lenses; (SB) Soleil-Babinet compensator; (PM) power meter; (SM1-4) spherical mirrors; (G1,2) gratings; (SL1-3) entrance/intermediate/exit slit; (S) shutter of the CCD detector

4.1.1 *c*-axis projection

As shown in Fig. 4.2 the light transmitted into the sample has a polarization projection onto the z axis (red line), and therefore onto the sample c axis, if the incident light has a polarization contribution along the y axis ($\mathbf{e}_\mathrm{i} \,||\, y$). Due to this projection c-axis contributions to the Raman tensor can be measured. This allows access to the E_g symmetry in tetragonal systems, and the B_{2g} and B_{3g} symmetries in orthorhombic crystals [179]. The percentage of the c-axis polarized light depends on the angle of the light in the sample, θ_a, which in turn depends on the angle of incidence θ_i and the index of refraction $n = n(\theta_\mathrm{i})$. It can be calculated via [184]

$$n(\theta_\mathrm{i}) = \frac{1}{\sqrt{2}} \left\{ n^2 - k^2 + \sin^2\theta_\mathrm{i} + \left[\left(n^2 - k^2 - \sin^2\theta_\mathrm{i} \right)^2 + 4n^2k^2 \right]^{1/2} \right\}^{1/2} \tag{4.1}$$

and

$$\theta_\mathrm{a} = \arcsin\left(\frac{\sin\theta_\mathrm{i}}{n(\theta_\mathrm{i})} \right). \tag{4.2}$$

The polarization inside the sample is $y^* \,||\, y + z \cdot \sin\theta_\mathrm{a}$. A technically similar projection onto the c axis also holds for the scattered light but is negligible due to the small angle of acceptance $\pm 15°$ of the collection optics (Objective O1 in Fig. 4.2). The index of refraction is determined for $\theta_\mathrm{i} = 66°$.

4.1.2 Determination of the optical constants

The Raman selection rules introduced in Section 3.2 require a precise setting of the light polarizations and absorbed power inside the sample. Unlike in the case of incidence normal to the sample surface, in the set-up used here the polarization inside the sample differs from the polarization of the incident beam due to the angle of incidence $\theta_\mathrm{i} = 66°$. The propagation direction of the light inside the sample also depends on the index of refraction $\tilde{n}$ of the sample according to the Fresnel equations. Hence, $\tilde{n} = n + \imath k$ was determined for each sample by ellipsometry. Based on $\tilde{n}$ both the settings required to achieve the correct polarization inside the sample and the power factor between incident and absorbed light can be calculated. The technique employed here was developed during the PhD theses of F. Venturini [185] and W. Prestel [186] and is described in more detail there.

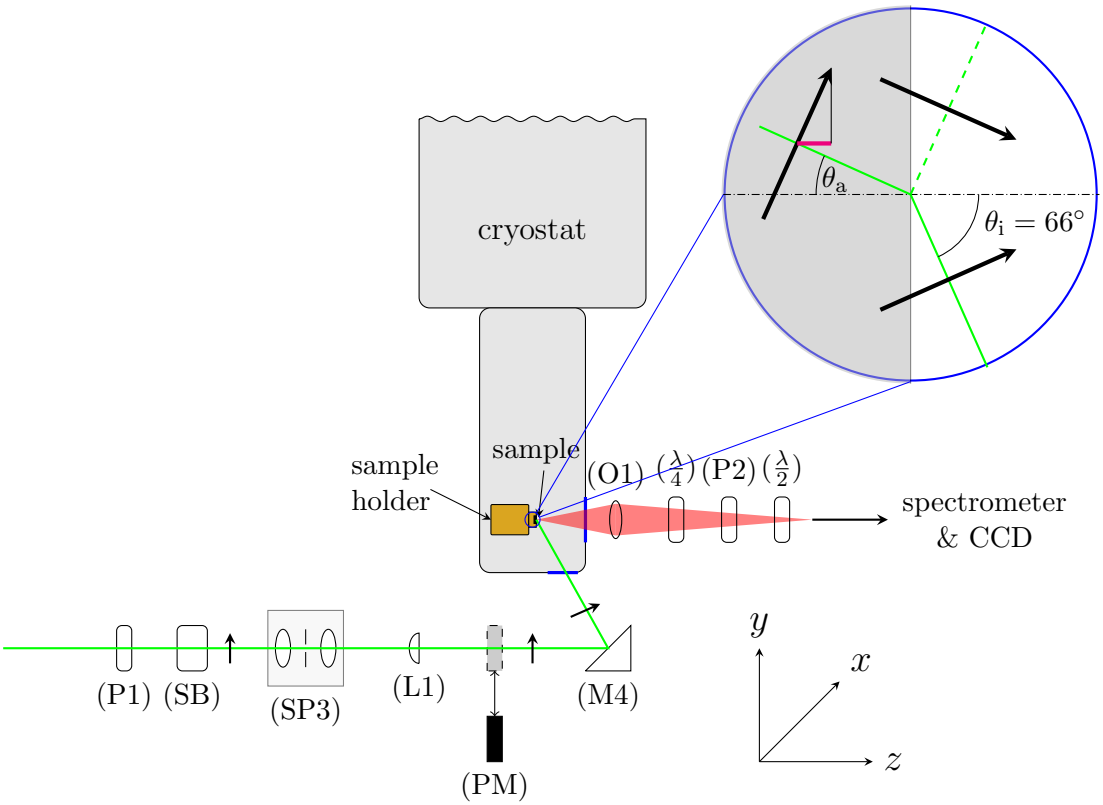

Figure 4.2: Non-normal incidence and z-axis projection in the lab Raman I. This is an excerpt of the spectroscopy set-up elucidated in Fig. 4.1 with the shown elements listed below. The magnified part (blue circle) highlights the incidence of the laser light (green line) onto the sample (grey). Black arrows denote the light polarization. Part of the light is reflected (dashed green line). Light transmitted into the sample has a projection of the polarization onto the z axis (red line) when the incident light has a polarization contribution parallel to the y axis.
(P1,2) polarizers; (SB) Soleil-Babinet compensator; (SP3) spatial filter; (L1) lens; (M4) mirror; (O1) objective; ($\lambda/_{2,4}$) half-/quarter-wave plates; (PM) power meter

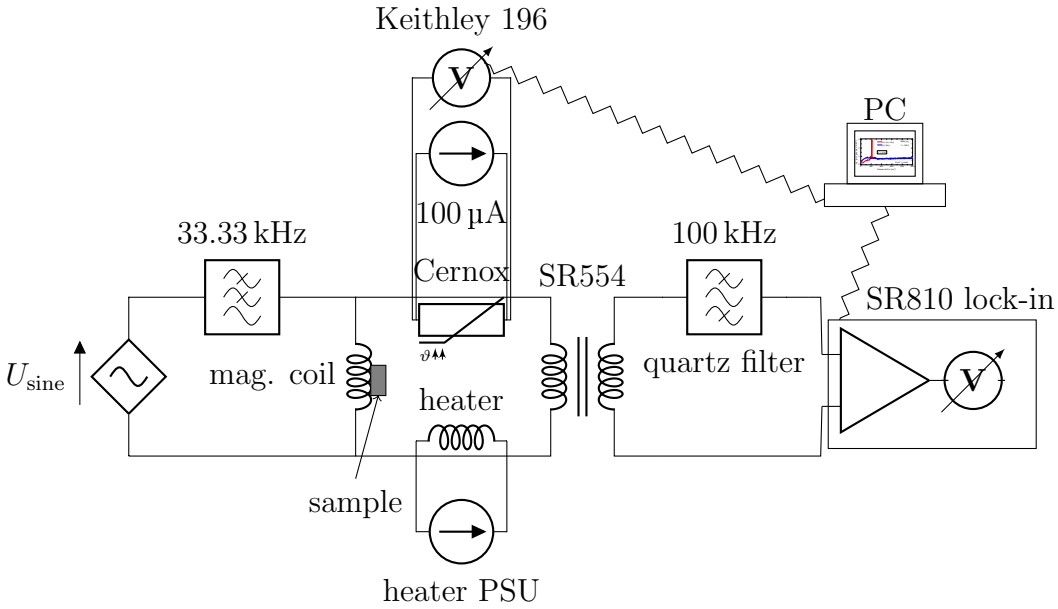

Figure 4.3: Setup to determine the critical temperature of superconducting samples. The excitation voltage U_{sine} is filtered to suppress higher harmonics and is applied to the magnet coil. The voltage induced in the coil is amplified by the SR554 transformer and filtered at three times the frequency of U_{sine} before being detected by the lock-in amplifier. The sample temperature is measured via four-probe measurement of a Cernox resistor. The temperature can be fine-tuned by controlling the current through the heater.

4.2 Measurement of the magnetic susceptibility

The temperatures at which the multiple phase transitions found in the IBS occur are characterizing properties of the samples. While Raman spectroscopy can be used to probe transition temperatures, as shown e.g. in Ref. [97], the recording of multiple Raman spectra in small temperature increments is usually a very time consuming process. It is therefore adjuvant to characterize samples by methods which allow for continuous measurements during temperature sweeps. The determination of the temperature dependence of the magnetic susceptibility conforms to this requirements. In particular the measurement of the third harmonic of the magnetic susceptibility was found to be a useful probe to the bulk superconducting properties of high-temperature superconductors. The measurement is contactless, probes the bulk properties, and is sensitive to inhomogeneities [185]. The physical concept to model the expected response, a peak with onset at T_c, is described in Refs. [185, 187, 188].

The experimental set-up used to measure the third harmonic of the magnetiza-

tion is described in detail in Ref. [185]. A simplified schematic is shown in Fig. 4.3. A sine generator creates the excitation voltage $U_{\mathrm{sine}}(f)$ which is then filtered to suppress higher harmonics and is applied to the magnetic coil to create the oscillating magnetic field $H_{\mathrm{appl}}(\omega = 2\pi f)$. The signal picked up by the coil is first amplified and then filtered at $3f$ using a quartz filter before being detected by the lock-in amplifier. The sample is placed on a Vespel support, which also hosts the coil, mounted on a copper base as any good conductors close to the sample will attenuate the magnetic field and signal. In the copper base a platinum resistor and heating coil are placed to measure and control the temperature.

Modifications to the original set-up made during this work include the installation of an additional transformer (Stanford Research SR554) to optimize the signal-to-noise ratio, of a second temperature sensor (calibrated Lakeshore Cernox CX-1050-AA-1.4L) suitable for low temperatures $T < 20\,\mathrm{K}$, and of a linear current amplifier (home-made up to 500 mA) to provide a fine grained control of the heater. The latter are prerequisites for measuring low critical temperatures such as $T_{\mathrm{c}} \approx 9\,\mathrm{K}$ in FeSe.

To determine T_{c} the sample is placed on the support and held in place by a Kapton spring. The dipstick is then evacuated and the inner volume is filled with He gas at ambient pressure whereas the outer volume contains He gas at merely low pressure to provide suitable but not too high thermal coupling to the environment. Finally the dipstick is placed in a LHe vessel and cooled down. By sweeping the temperature across T_{c} the change in the induced voltage U_3, which is proportional to the third harmonic of the magnetic susceptibility, $U_3 \propto \chi_3$, can be recorded. Measurements performed this way to characterize the FeSe sample are shown in Sec. 4.3.4. Based on this set-up a more evolved version was developed by R. Roßner [187] for in situ determination of T_{c} inside a diamond anvil cell. This set-up was further optimized during the course of this work in collaboration with A. Walter [188] and is described in more detail in Appendix A.2.

4.3 Sample preparation and characterization

4.3.1 Overview

Table 4.1 gives an overview of the samples studied. The properties of $BaFe_2As_2$ (#111129) were determined in the author's diploma thesis [97]. The determination of the critical temperatures T_{c} and the structural transition temperature T_{s} of the

Material	Sample Batch & ID	Details	T_s (K)	T_{SDW} (K)	T_c (K)
FeS	E151, #160922a2 (R)	[189]	n/a	n/a	4.5
FeS	E256, #170426 (R)	[189]	n/a	n/a	
FeS	E256, #170504	[189]	n/a	n/a	4.1
$BaFe_2As_2$	LS2712, #111129 (R)	[17]	135.3 [97]		n/a
	#111129 detwinned (R)		140.4 [97]	137.9 [97]	n/a
$BaFe_2As_2$	4398, #151019	[17]	134 [17]		n/a
FeSe	TWOX1295, #151207	[93]		n/a	
FeSe	TWOX1295, #151209 (R)	[93]	89.1	n/a	8.8
FeSe	TWOX1555, #170311 (R)	[93]		n/a	Sec. A.3.1

Table 4.1: Studied samples and their transition temperatures. Sample batch and sample ID refer to the documentation by the crystal grower and, respectively, of this thesis. Samples marked with (R) were used for Raman spectroscopic measurements. T_s, T_{SDW}, and T_c are the transition temperatures to the orthorhombic, the magnetically ordered, and the superconducting phase, respectively.

FeS and FeSe samples is described in the following sections. FeSe TWOX1555 (#170311) was used for testing the DAC set-up. The corresponding measurements are shown in Sec. A.3 of Appendix A.

4.3.2 FeS

Sample classification and preparation

Two sample batches of tetragonal *t*-FeS, labelled E151 and E256, were obtained from the group of C. Petrovic. The samples were grown by de-intercalation of potassium from $K_xFe_{2-y}S_2$ [189]. Out of each batch two samples were selected, one for magnetization measurements in the SQUID magnetometer and the other one for Raman measurements. Samples selected for Raman spectroscopy were chosen to provide large flat areas and were mounted on a copper block clamped in the sample holder described in Ref. [97].

Determination of the critical temperature T_c

T_c is a sensitive probe of stoichiometry [105, 190]. Therefore one sample from each batch (E151 and E256) was selected for a magnetization measurement in the SQUID

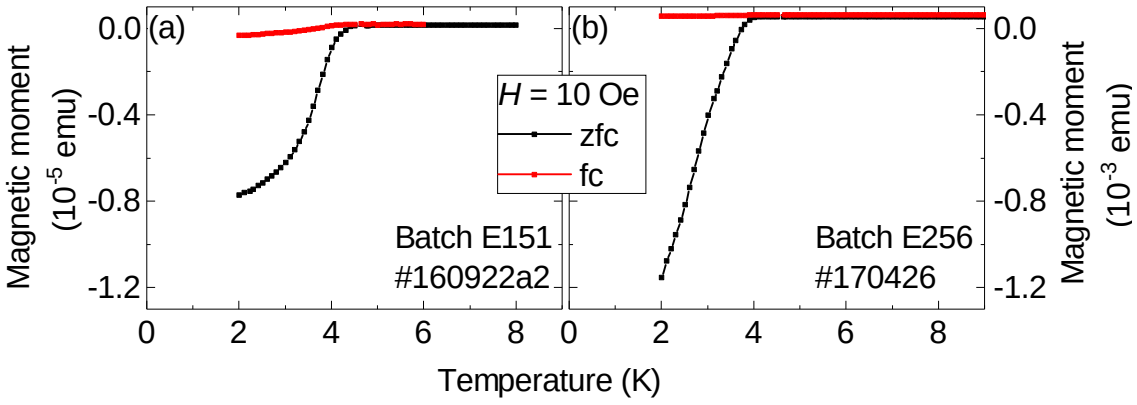

Figure 4.4: Magnetization measurements of the two FeS samples selected from (a) batch E151 (#160922a2) and (b) batch E256 (#170504). Both curves show measurements done in low fields of $H = 10\,\mathrm{Oe}$ after cooling the sample without (zfc, black curves) and with applied field (fc, red curves).

magnetometer of the WMI (Quantum Design MPMS XL-7). The samples were attached using Fixogum glue. From the first batch (E151) the sample #160922a2 was investigated by Raman spectroscopy and the second part (after cleaving) was measured in the SQUID magnetometer. For the second batch (E256) two separate samples were used for the magnetometry (#170504) and spectroscopic measurements (#170426), respectively.

Figure 4.4 shows magnetization measurements of the two FeS samples. The measurements were done in an applied field of $H = 10\,\mathrm{Oe}$. For both samples the zero-field cooled (zfc) curves show a steep decrease below a temperature T_c^on. For the sample from batch E151 the curve tends to saturate towards 2 K. The field cooled curves (fc, red curves), measured after cooling down to 2 K with applied field, show only a very small decrease below T_c^{on}. As the absolute magnetic moment is shown the difference in magnitude of the signal between the two samples results from the difference of the sample volumes. The fc curves show the response from the Meissner effect and their weak change below T_c indicates strong flux pinning. T_c^on is approximately 4.5 K for the sample from batch E151 and 4.1 K for batch E256. Both the critical temperatures and functional dependences are in good agreement with the measurements of Lai *et al.* [35].

Optical constants

The ellipsometry was performed by M. Grujić-Brojčin in Belgrade [154] using a SOPRA GES5E - IRSE ellipsometer. The results for the real and imaginary parts

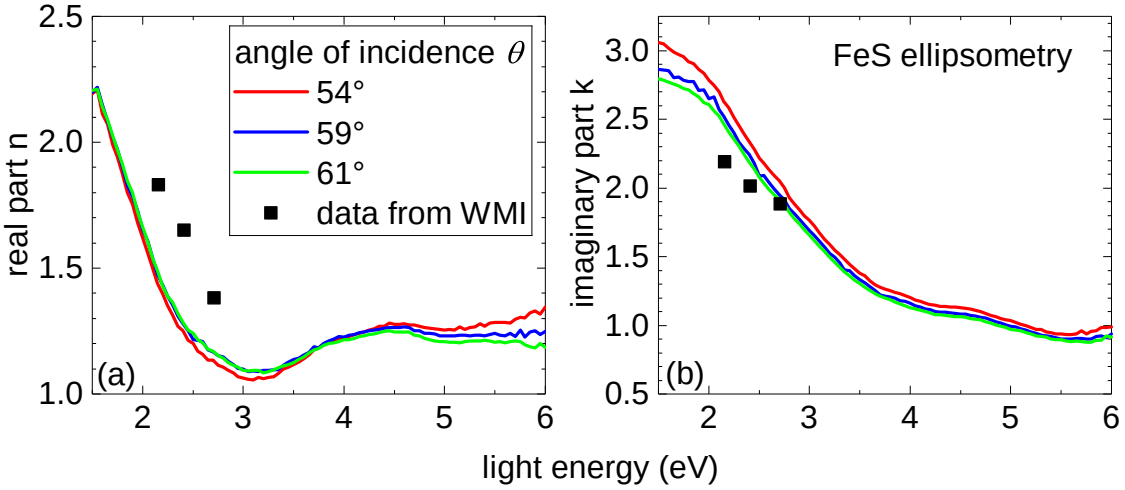

Figure 4.5: Index of refraction of t-FeS as a function of the energy of the incident light for three different angles of incidence as indicated. Black squares indicate data measured at the WMI. Both (a) real part and (b) imaginary part show a pronounced dependence on the energy but little dependence on the angle of incidence. Courtesy of M. Grujić-Brojčin and N. Lazarević

of the index of refraction $\tilde{n} = n + \imath \cdot k$ are shown in Fig. 4.5 as a function of the energy of the incident light and the angle of incidence. While both n and k show a strong dependence on the light energy below 3.5 eV, the dependence on the angle of incidence is weak to negligible in the relevant energy region from 2 eV to 3 eV. For comparison the values obtained with the set-up described in chapter 4.1.2 are shown as black squares. While some agreement with the data from Belgrade exists for the imaginary part the real part measured this way shows a significant offset, though the overall trend is reproduced. The data from Belgrade for an angle of incidence $\theta = 61°$ were used to calculate the settings for the light polarizations and absorbed laser power.

Sample orientation

The FeS sample was oriented along the crystal edges which typically are identical to crystal axes. To test the correct orientation the Fe phonon having B_{1g} symmetry has proven to be a useful probe in the IBS. Figure 4.6 shows Raman spectra of t-FeS at $T = 314\,\mathrm{K}$ taken with a resolution of $\Delta\tilde{\nu} \approx 5\,\mathrm{cm}^{-1}$ and a step width of $\Delta\Omega = 5\,\mathrm{cm}^{-1}$. The B_{1g} phonon appears in aa polarization (blue line) but vanishes in ab (green) indicating a good orientation of the sample whereby the crystallographic axes a, b are at parallel to the lab coordinate system, $(a, b)||(x, y)$.

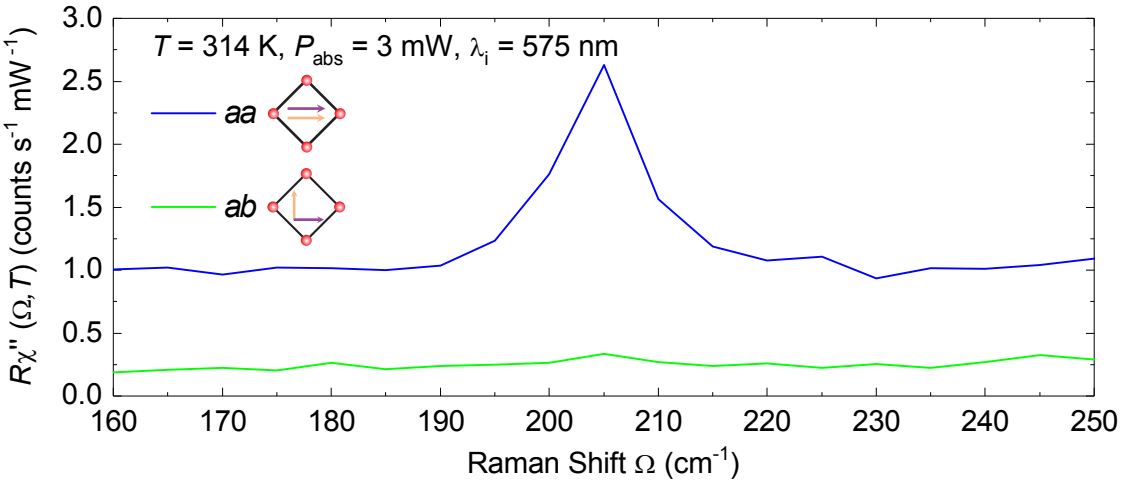

Figure 4.6: Raman spectra of t-FeS at $T = 314\,\mathrm{K}$ for light polarizations as indicated. Violet and orange arrows denote the polarizations of the incident and scattered light, respectively. The appearance of the B_{1g} phonon at $205\,\mathrm{cm}^{-1}$ in the aa and disappearance in the ab spectrum indicates that the sample is well aligned with respect to the lab coordinate system.

4.3.3 $BaFe_2As_2$

Sample classification and preparation

Samples of stoichiometric $BaFe_2As_2$ from Batches LS2712 and 4398 were provided by the group of I. R. Fisher from Stanford. The sample growth is described in Ref. [17]. The transition to the orthorhombic magnetic state in the non-strained sample (#111129) was determined in the authors' diploma thesis [97] as $T_\mathrm{s} \approx T_\mathrm{SDW} \approx 135.3\,\mathrm{K}$ using the low-energy B_{1g} Raman response as probe. The same measurements on the sample under uniaxial pressure yielded $T_\mathrm{SDW} \approx 137.9\,\mathrm{K}$ and $T_\mathrm{s} \approx 140.4\,\mathrm{K}$.

Optical constants

The index of refraction for the $BaFe_2As_2$ sample (#100310a1) from batch LS2712 was determined for $\lambda_\mathrm{i} = 458\,\mathrm{nm}$ and 514 nm in 2010 and is shown in Fig. 4.7 as orange circles. These data were used in three previous studies [97, 114, 191] assuming a negligible energy dependence. During the Master's thesis of F. Löffler [192] the index of refraction of a sample from batch 4398 (#151019) was measured by ellipsometry. The results are shown in Fig. 4.7 as red squares. Both measurements yield similar but not equal values of k and significantly different ones for the real part n.

From n and k the reflectivity R can be calculated as

$$R = \frac{(n-1)^2 + k^2}{(n+1)^2 + k^2}. \tag{4.3}$$

The resulting values are shown in Fig. 4.7(c) as orange circles (#100310a1 from 2010) and red squares (#151019 from 2017). The calculated reflectivity is identical for both measurements.

The ellipsometry measurements can be compared to data from infrared studies provided by L. Degiorgi (black lines in Fig. 4.7) and taken from Refs. [193] (green lines) and [29] (blue line). The reflectivity values from these three studies vary by a factor of almost two. Within the error bars set by this variation the reflectivity from the ellipsometry (red squares) agrees well for the red and yellow light ($\lambda_\mathrm{i} > 530\,\mathrm{nm}$) but is higher for shorter wavelengths. Two points are noteworthy regarding the discrepancies:

(1) The determination of n and k from the reflectivity alone (not from ellipsometry) is not unique. Obviously, the reflectivities calculated from n and k according to Eq. 4.3 (orange circles and red squares) are identical though n and k are different.

(2) Significant leakage due to possible inaccuracies of the polarizations was found neither in the previous Raman studies [97, 114, 191] using the index of refraction determined in 2010, nor in the recent study [192] using the values determined in 2017.

Phase transitions and laser heating

As the measurements shown below were all performed at temperatures far below the phase transitions T_s and T_SDW the exact value of the heating by the laser is of little relevance. Therefore the laser heating was not determined again but the values from Refs. [97] and [194] determined on the very same sample were used to estimate an upper limit of the heating of $\Delta T_\mathrm{L}(P_\mathrm{abs} = 4\,\mathrm{mW}) \leq 10\,\mathrm{K}$.

4.3.4 FeSe

Sample classification and preparation

Samples of tetragonal β-FeSe from Batch TWOX1295 were provided by T. Wolf from the KIT in Karlsruhe. The samples were grown as described in Ref. [93] and cleaned with ethanol after growth. For Raman spectroscopy the sample having the largest flat areas was chosen.

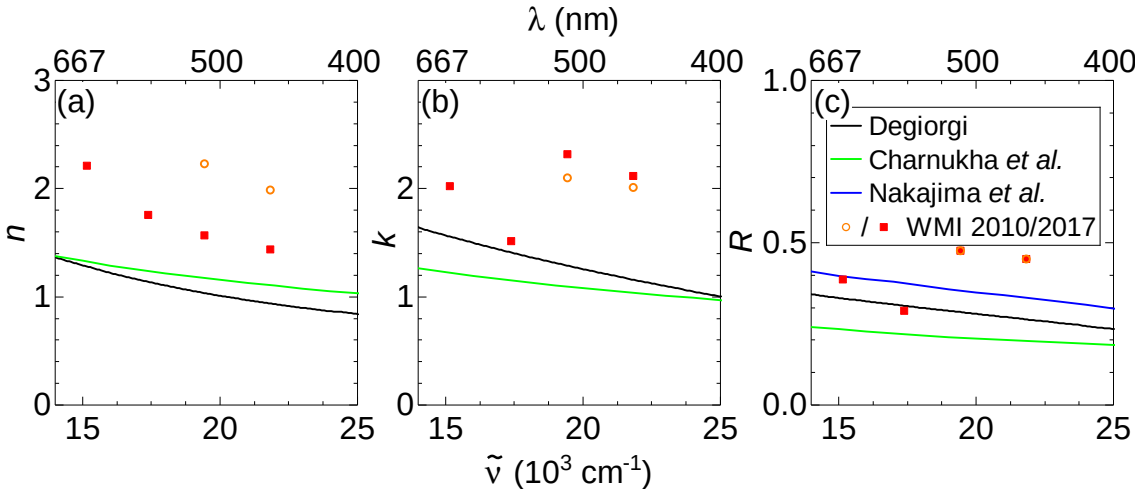

Figure 4.7: Index of refraction $\tilde{n}$ and reflectivity R of undoped $BaFe_2As_2$ as a function of the energy $\tilde{\nu}$ of the incident light. The top axis shows the corresponding wavelength. (a) Real part n and (b) imaginary part k of $\tilde{n}$. (c) Reflectivity R as provided (black), calculated from the optical conductivity (green and blue), or calculated from n and k (red squares). The data measured by ellipsometry at the WMI [114, 192] are shown as orange circles and red squares. Black lines are data provided by L. Degiorgi. Data for the green and blue lines are taken from Ref. [193] and [29], respectively.

Superconducting properties

To determine T_c the set-up described in Sec. 4.2 was used. The measurements performed on FeSe are shown in Fig. 4.8(a). A well defined peak is visible in the heating curve, the onset of which can be identified by taking the intersection of its linear high temperature flank and a linear fit of the signal offset. This yields $T_c^{heat} = 9.6\,K$. T_c determined upon cooling is shown as blue curve. From the peak onset one obtains $T_c^{cool} = 7.9\,K$. The critical temperatures determined upon cooling and heating differ due to the thermal hysteresis of the set-up. The average $T_c^{avg} = \frac{1}{2}(T_c^{heat} + T_c^{cool}) = 8.8\,K$ agrees well with the values expected for nearly-stoichiometric FeSe [105].

As an additional test of the sample quality the signatures of the superconducting state visible in Raman spectroscopy were recorded. Fig. 4.8(b) shows spectra in *ab* polarization for temperatures above (orange curve) and below (black curve) the critical temperature T_c. Both spectra show a steep increase below $10\,cm^{-1}$ due to elastically scattered light from surface layers accumulating at low temperatures. Subtracting the spectrum for $T > T_c$ from the superconducting spectrum, as shown in the inset, illustrates the suppression below $13\,cm^{-1}$ coming from the supercon-

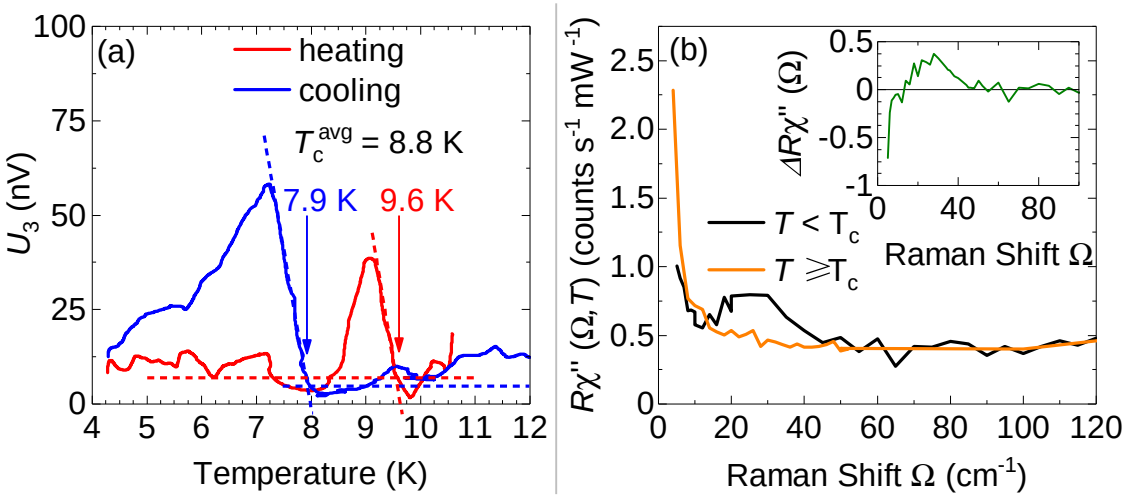

Figure 4.8: (a) Voltage induced at three times the excitation frequency in the magnetization measurement reflecting the magnetic response of the FeSe sample upon heating (red) and cooling (blue). (b) Raman spectra of FeSe in *ab* polarization above (orange) and below (black) the superconducting transition. The inset shows the difference of the two spectra $[\Delta R\chi''(\Omega) = R\chi''(T < T_c) - R\chi''(T \geq T_c)]$.

λ_i (nm)	n	k
458	2.12	2.13
514	2.29	2.33
575	2.59	1.56

Table 4.2: Complex index of refraction of FeSe for three laser wavelengths λ_i.

ducting gap, as well as the pair breaking peak at 25 cm^{-1}. These measurements agree with previously published data [126], though in the spectra here the double structure of the pair breaking peak was not resolved due to the step size of $\Delta\Omega = 5\,\mathrm{cm}^{-1}$.

Optical constants

The index of refraction, needed to set the correct polarizations and laser power for the spectroscopic measurements, was determined by ellipsometry using the set-up described in Sec. 4.1.2 for the FeSe sample #151207. The results are shown in Table 4.2 and are comparable to values obtained for $BaFe_2As_2$ (see Sec. 4.3.3 and Ref. [192]).

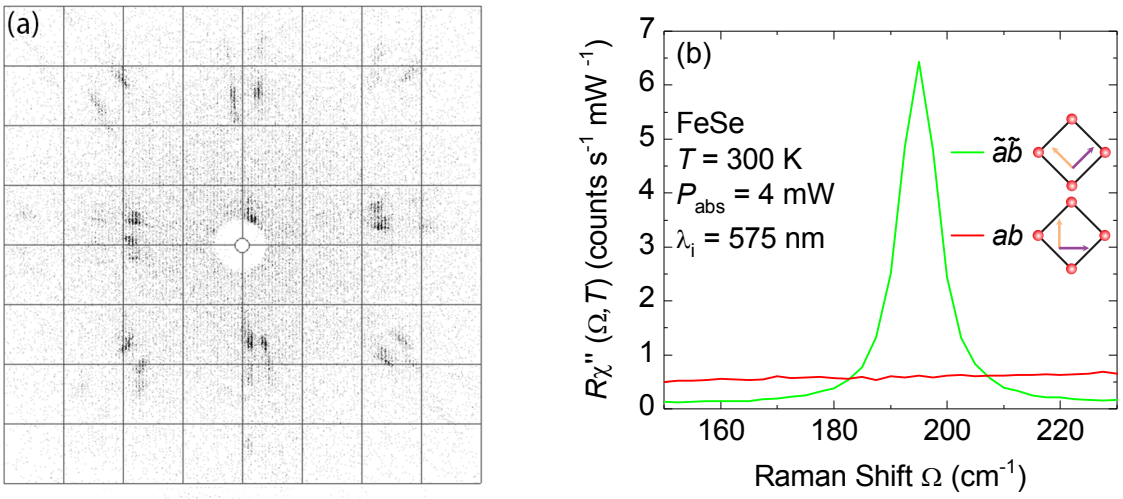

Figure 4.9: (a) Laue diffraction image of the FeSe sample. (b) Raman spectra of FeSe at $T = 300\,\mathrm{K}$ in polarizations as indicated. Violet and orange arrows denote the polarizations of the incident and scattered light, respectively. The B_{1g} phonon at $195\,\mathrm{cm}^{-1}$ appears in $\tilde{a}\tilde{b}$ polarization and shows no leakage in ab polarization.

Sample orientation

To correctly align the sample inside the cryostat it was was examined using the Laue imaging system in the crystal lab of the TUM. The alignment was optimized using the degrees of freedom provided by the sample holder.

Fig. 4.9(a) shows the image of the best sample orientation achieved. The most striking features are the double peaks which indicate the existence of two crystals in the sample which are slightly rotated about the c axis with respect to each other. As no deviations from the selection rules due to this imperfection appeared in the measurements it is likely that either one of the crystallites was removed by cleaving or that solely the top crystallite was measured by optical spectroscopy due to its thickness.

As a further test of the sample alignment the selection rules themselves can be used. In IBS the Fe phonon in B_{1g} symmetry is a useful probe. It appears for crossed linear polarizations ($\mathbf{e}_\mathrm{i} \perp \mathbf{e}_\mathrm{s}$) at 45° with respect to the crystal axes. From Fig. 4.9(b) it can be concluded that the sample is mounted with its crystal axes $(a, b)||(x, y)$.

Structural transition and laser heating

As was shown by Kretzschmar *et al.* [118] the twin domains forming below T_s increase the amount of elastically scattered light, thus making them visible in the

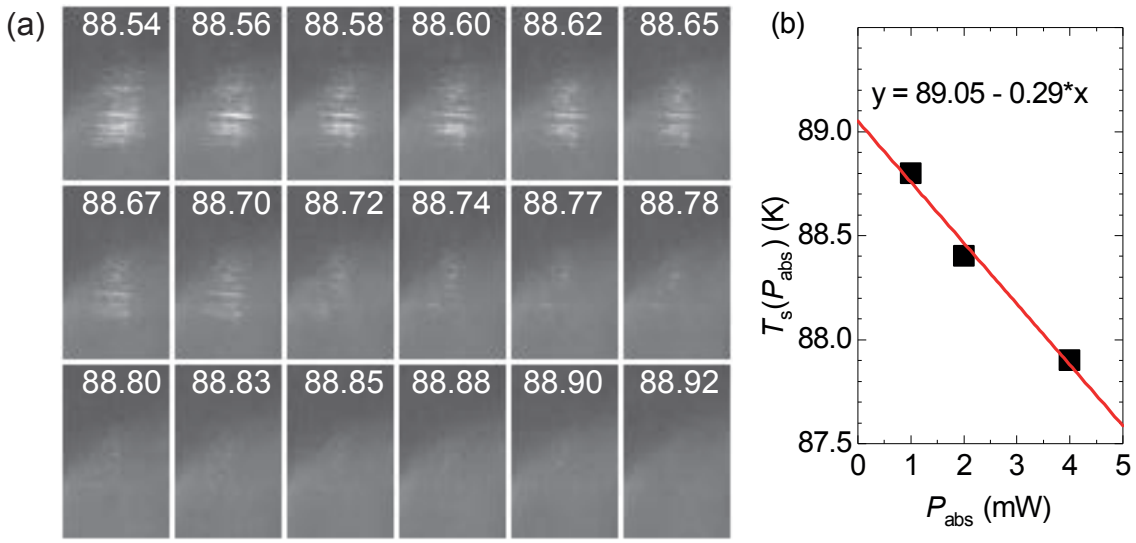

Figure 4.10: (a) Images of the laser spot with an absorbed power $P_{\mathrm{abs}} = 1\,\mathrm{mW}$ at temperatures of the sample holder in Kelvin as indicated. Stripes due to twin domains are visible below T_{s} and vanish abruptly at the phase transition. (b) Apparent transition temperature $T_{\mathrm{s}}(P_{\mathrm{abs}})$ as a function of the absorbed laser power P_{abs}. From the linear fit equation T_{s} and the laser heating can be read directly.

laser spot as stripes. By recording visual images of the laser spot at different values of the absorbed laser power while sweeping the temperature of the sample across the structural phase transition both T_{s} and the laser induced heating can be determined. Images of the laser spot on the FeSe sample for an absorbed laser power $P_{\mathrm{abs}} = 1\,\mathrm{mW}$ are shown in Fig. 4.10(a). The numbers shown indicate the temperature measured at the sample holder. Below the structural phase transition the spot appears brightly and shows stripes caused by the crystal twins. Upon heating the sample the spot dims and vanishes within 0.1 K when reaching the phase transition which can be determined as $T_{\mathrm{s}}^{1\,\mathrm{mW}} = 88.8\,\mathrm{K}$. The real transition temperature is lower by the laser heating. Repeating this procedure for different values of P_{abs} yields a linear relationship between $T_{\mathrm{s}}(P_{\mathrm{abs}})$ and P_{abs} as shown in Fig. 4.10(b). From the linear fit (red line) the real phase transition temperature can be read directly as the axis intercept and is $T_{\mathrm{s}} = 89.1(2)\,\mathrm{K}$. The laser heating is given by the negative of the slope and is $\Delta T_{\mathrm{L}} = 0.3(1)\,\mathrm{K\,mW^{-1}}$.

Chapter 5

Results

This chapter presents the results of the Raman experiments on three families of IBS which will be further analysed and discussed in Chap. 6.

5.1 FeS

Spectra on FeS were measured in the range from $175\,\mathrm{cm}^{-1}$ to $335\,\mathrm{cm}^{-1}$ where the phonons are found. As phonon peaks are narrow these spectra were measured in small steps of $\Delta\Omega = 1\,\mathrm{cm}^{-1}$ with a resolution of $\Delta\tilde{\nu} \approx 5\,\mathrm{cm}^{-1}$. The data are normalized as described in Sec. 3.3 except for the factor $\omega_\mathrm{i}/\omega_0$ as only one laser line at $\lambda_\mathrm{i} = 575\,\mathrm{nm}$ was used. Temperatures shown are measured at the sample holder and are not corrected for heating from the laser.

5.1.1 Phonons

Figure 5.1(a) shows spectra measured on sample #160922a2 from batch E151 at $T = 80\,\mathrm{K}$ and an absorbed power of $P_\mathrm{abs} = 3\,\mathrm{mW}$. In parallel light polarizations (aa and bb) three peaks are visible. Out of those the peaks at $305\,\mathrm{cm}^{-1}$ and $265\,\mathrm{cm}^{-1}$ vanish for both crossed polarizations ($\tilde{a}\tilde{b}$ and ba) whereas the third peak at $215\,\mathrm{cm}^{-1}$ appears in all polarizations except ba. Based on their symmetry a preliminary identification of the $215\,\mathrm{cm}^{-1}$ mode as Fe phonon in B_{1g} symmetry and of the $305\,\mathrm{cm}^{-1}$ mode as S phonon in A_{1g} symmetry can be done, but the identification of the third peak labelled P1 is not trivial. Additionally the peak at $305\,\mathrm{cm}^{-1}$ exhibits a clear asymmetry. Therefore the assignment shown in Fig. 5.1 is considered preliminary and a detailed discussion of the modes is given in chapter 6.1.1. To verify the correct identification and especially to test the possibility that peak P1 might appear

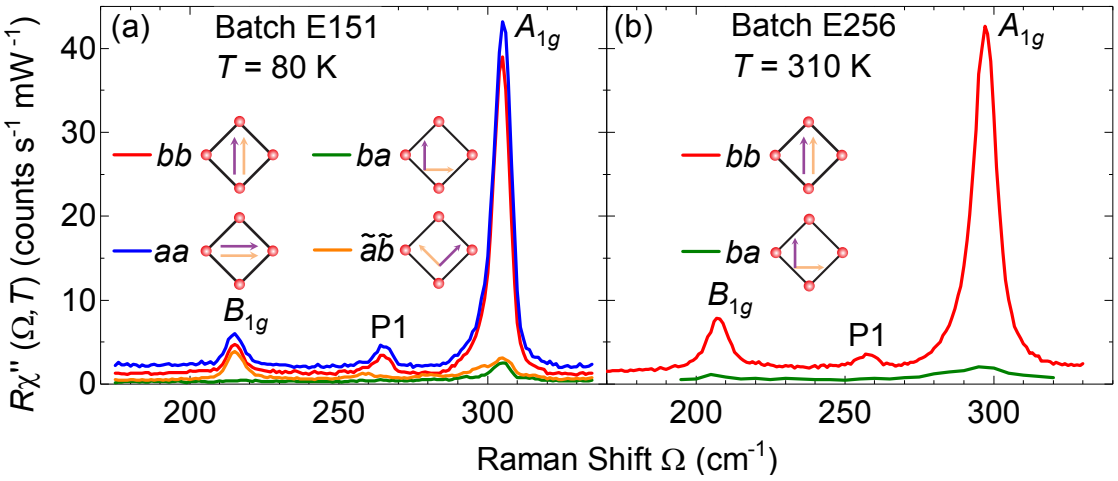

Figure 5.1: Low-energy Raman spectra of two t-FeS samples at temperatures of the sample holder and polarizations as indicated. Violet and orange arrows denote the polarizations of the incident and scattered light, respectively. The denomination of the peaks is preliminary.

due to sample issues (defects) measurements were performed on a second sample (#170426) from a different batch (E256). These spectra, shown in Fig. 5.1(b), were measured at $T = 310\,\mathrm{K}$ and an absorbed power of $P_{\mathrm{abs}} = 2\,\mathrm{mW}$ with all other settings as given above. Similarly as in Fig. 5.1(a) all three peaks appear in parallel light polarizations, albeit at slightly lower energies, but vanish when the polarization for the scattered light is rotated by 90°.

5.1.2 Temperature dependence of the phonon modes

To study the temperature dependence of the phonons spectra in *bb* polarization were measured because all phonon modes can be identified in a single spectrum as shown in the previous section. The spectra for all temperatures are shown in Figure 5.2(a). The absorbed laser power was set at $P_{\mathrm{abs}} = 3\,\mathrm{mW}$ for high to medium temperatures and reduced to $P_{\mathrm{abs}} = 2\,\mathrm{mW}$ at $T = 21\,\mathrm{K}$ and below to reduce the additional heating caused by the laser. Figure 5.2(b) highlights three spectra from panel (a) for 300 K, 40 K and 8 K. Three peaks are visible at all temperatures and exhibit a monotonous shift to higher energies upon cooling.

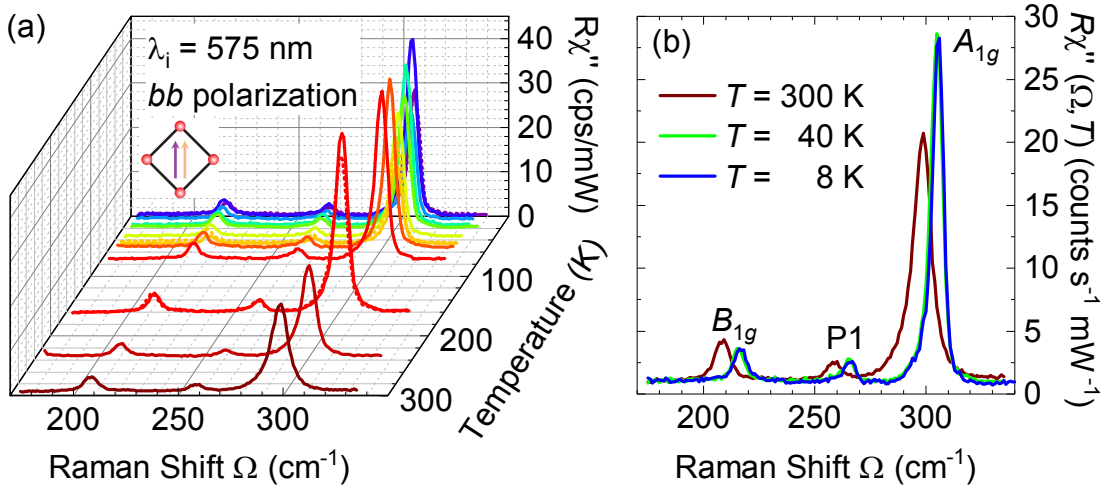

Figure 5.2: Low-energy Raman spectra of t-FeS sample #160922a2 measured with bb polarized light at temperatures as indicated.

5.2 $BaFe_2As_2$

De-twinned $BaFe_2As_2$ [97] was studied for pinning down the anomalous intensity of the As phonon. To this end spectra in four polarizations ($\tilde{a}\tilde{a}$, $\tilde{b}\tilde{b}$, aa, and ab) were measured for wavelengths λ_i of the incident laser light ranging from 407 nm to 676 nm and are shown in Fig. 5.3. The As phonon appears as strong symmetric peak at 180 cm^{-1}. As the spectra were taken with a fixed width $M = 550\,\mu m$ of the spectrometer intermediate slit (1100 µm for $\lambda_i = 647$ nm to 676 nm) the resolution depends on the wavelength and the peak width does not directly reflect the intrinsic line width of the phonon. The spectra are normalized as described in Sec. 3.3. As some of the spectra were measured in 2013 [191] and some in 2017 [192] the background below the phonon peak varies due to a slight degradation of the sample surface. The spectral weight $A_{is}^{(As)}$ of the phonon was extracted by fitting a Voigt profile to the peak, whereby the width Γ_G of the Gaussian part is given by the known resolution $\Delta\tilde{\nu}$ of the spectrometer (Appendix C), after subtracting a linear background. The results were found to be reproducible in both series of measurements (see Sec. 6.1.2 and Ref. [192]). For some spectra the peak position deviates from the expected value of 180 cm^{-1}. These deviations occurred occasionally and were ascribed to mechanical issues of the spectrometer. For $\tilde{a}\tilde{a}$ light polarization the As phonon peak shows an almost monotonous decrease with increasing λ_i. For $\tilde{b}\tilde{b}$ polarization the phonon is strong at $\lambda_i < 420$ nm but is almost indiscernible in the range from 450 nm to 490 nm due to its low spectral weight and the strong broadening due to the coarse resolution. The peak becomes well defined for $\lambda_i > 490$ nm

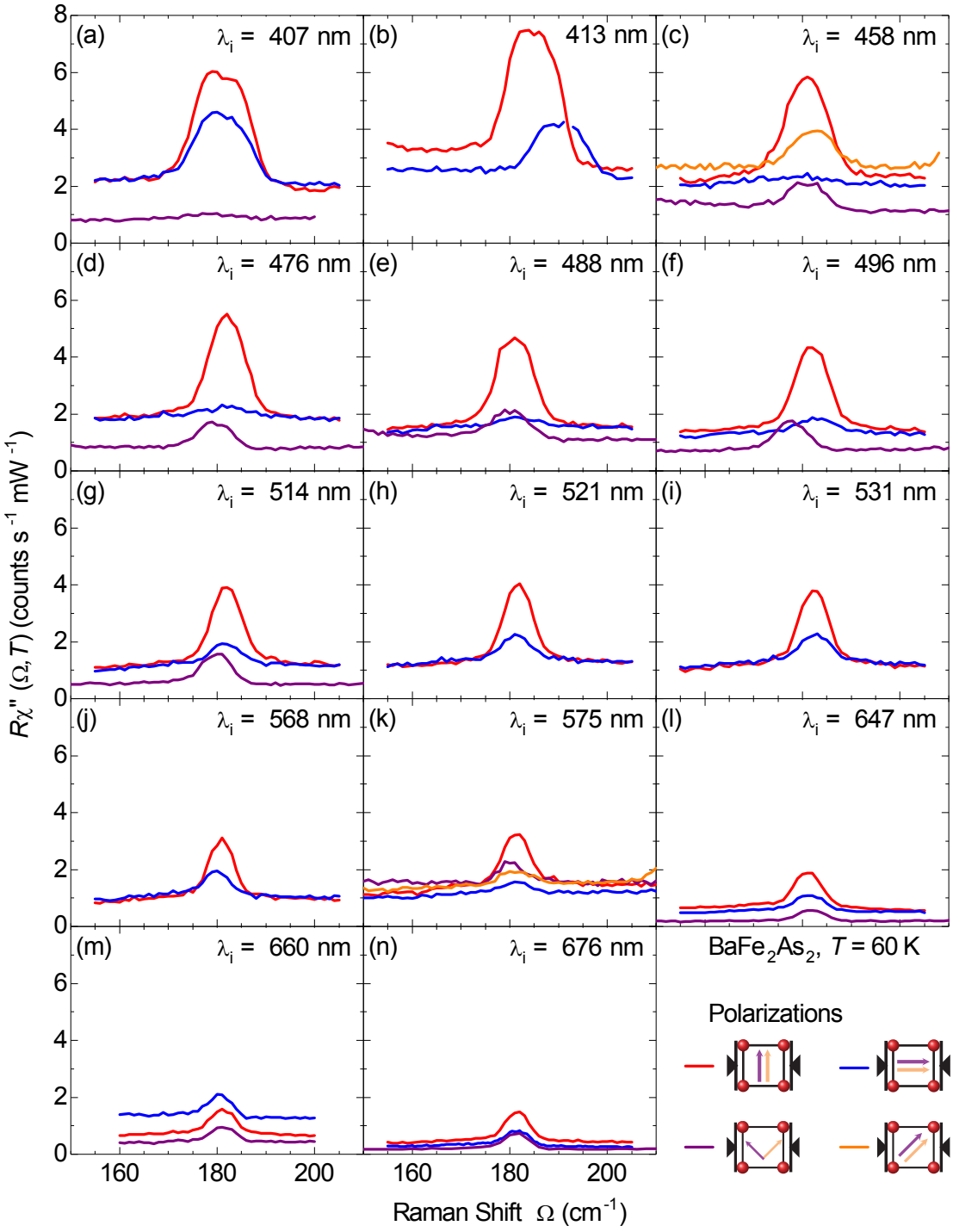

Figure 5.3: Raman spectra of de-twinned $BaFe_2As_2$ measured at $T = 60\,\mathrm{K} < T_{\mathrm{SDW}}$ for wavelengths $\lambda_i = 407\,\mathrm{nm}$ to $676\,\mathrm{nm}$ of the incident light as indicated. The polarizations are indicated as violet and orange arrows for the incident and scattered light, respectively. The black triangles show the direction of the uniaxial pressure. As the spectra were measured with a constant slit width the resolution depends on λ_i and the peak width does not directly reflect the phonon line width.

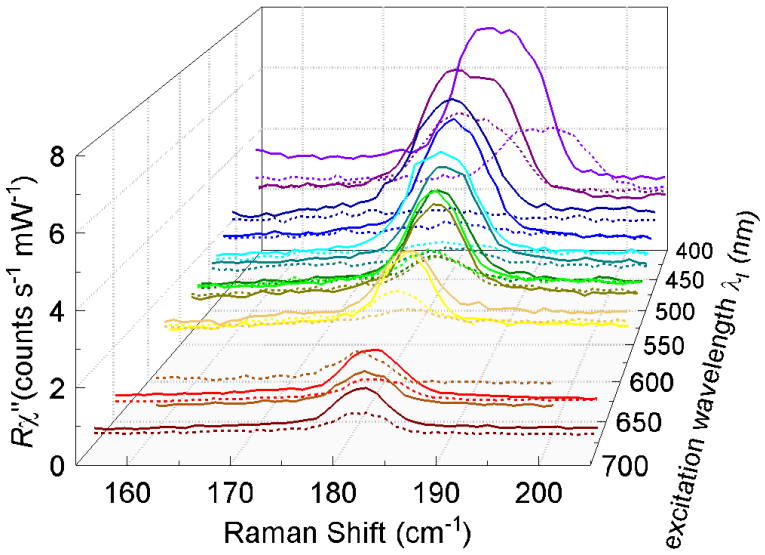

Figure 5.4: Raman spectra of de-twinned $BaFe_2As_2$ measured at $T = 60\,\mathrm{K} < T_{\mathrm{SDW}}$ for wavelengths λ_i of the incident light as shown on the right axis. The spectra are duplicated from Fig. 5.3. For $\tilde{a}\tilde{a}$ polarization (solid lines) the phonon peak grows monotonously when λ_i is reduced to 413 nm and slightly decreases for $\lambda_i = 407\,\mathrm{nm}$. The peak in $\tilde{b}\tilde{b}$ polarization (dashed lines) remains small for $\lambda_i > 450\,\mathrm{nm}$ followed by an abrupt increase in spectral weight for shorter wavelengths.

again. In ab polarization the phonon peak almost vanishes at $\lambda_i = 407\,\mathrm{nm}$, but shows little change at λ_i from 458 nm to 514 nm. Its spectral weight decreases for longer wavelengths.

To better illustrate the main effect in $\tilde{a}\tilde{a}$ and $\tilde{b}\tilde{b}$ polarizations the corresponding spectra from Fig. 5.3 are duplicated in Fig. 5.4 where they are shown in one diagram as a function of both the Raman shift Ω and the wavelength λ_i. This figure shows that the peak height and spectral weight for $\tilde{a}\tilde{a}$ polarization (solid lines) increase monotonously towards shorter wavelengths, but drop slightly for $\lambda_i = 407\,\mathrm{nm}$. In contrast the peak shows little change in $\tilde{b}\tilde{b}$ polarization (dashed lines) for $\lambda_i > 450\,\mathrm{nm}$ but abruptly gains both height and spectral weight for the shortest two laser lines at 413 nm and 407 nm. For both polarizations the peak broadens with decreasing λ_i due to the changing resolution of the spectrometer (Appendix C).

5.3 FeSe

In this section Raman spectra from the FeSe sample characterized in Chap. 4.3 are presented. Temperatures shown include the laser heating determined in Sec. 4.3.4.

5.3.1 Luminescence and resonance behaviour

To study the resonance behaviour of the various excitations and to test for putative luminescence contributions spectra were recorded at 41 K in all six polarizations with excitation at $\lambda_i = 458\,\text{nm}$, 514 nm and 575 nm in steps of $\Delta\Omega = 50\,\text{cm}^{-1}$. These spectra are shown in Fig. 5.5(a-c). The sharp line at $200\,\text{cm}^{-1}$ labelled 'ph' comprises the Se and Fe phonons the line shapes of which are not resolved due to the coarse resolution and which are disregarded here. Spectra with contributions from B_{1g} symmetry (ab, $\tilde{a}\tilde{a}$, RL) are dominated by a broad asymmetric peak centred around $500\,\text{cm}^{-1}$. Spectra comprising B_{2g} symmetry (aa, $\tilde{a}\tilde{b}$, RL) exhibit a broad maximum around $3500\,\text{cm}^{-1}$. For $\lambda_i \leq 514\,\text{nm}$ an additional broad, polarization-dependent peak arises centred at roughly 4000-5500 cm^{-1} depending on λ_i. Fig. 5.5(d-f) shows sums of pairs of corresponding spectra for each laser line λ_i whereby each pair contains all four in-plane symmetries ($A_{1g} + A_{2g} + B_{1g} + B_{2g}$) of the D_{4h} point group. Hence, all sums for one λ_i must be identical and therefore the spectra with incident light polarized along a were multiplied by a factor f_a to match the intensities of the other two sums. Taking into account this factor the pure symmetries can be extracted as linear combinations of the spectra and are shown in Fig. 5.5(g-i). The peak around $500\,\text{cm}^{-1}$ in B_{1g} symmetry gains intensity towards shorter λ_i. For $\lambda_i = 514\,\text{nm}$ the additional high-energy peak centred around $4000\,\text{cm}^{-1}$ contributes almost exclusively to the B_{2g} symmetry. For $\lambda_i = 458\,\text{nm}$ this peak is centred around $5500\,\text{cm}^{-1}$ and appears in all symmetries with different intensity.

Contributions from luminescence

The additional contribution found mainly in the B_{2g} spectra for $\lambda_i = 514\,\text{nm}$ and 458 nm [Figs. 5.5(h-i)] is likely a luminescence effect. As shown in Fig. 5.6 the B_{2g} spectra for all three laser lines are virtually identical up to $\Omega \approx 1500\,\text{cm}^{-1}$ but deviate at higher energies. The broad peak found for $\lambda_i \leq 514\,\text{nm}$ can be modelled qualitatively by a parabola for each laser line multiplied with a hyperbolic tangent to provide a cut-off at $1500\,\text{cm}^{-1}$. Subtracting these functions (light blue and dark green curves in Fig. 5.6) from the experimental data (blue and green solid lines) yields spectra which are identical to the 575 nm spectrum (solid dark yellow line) in the common range. This suggests that the B_{2g} response without luminescence would be rather independent of the excitation energy. Therefore no subtraction was performed for the spectra measured with $\lambda_i = 575\,\text{nm}$ shown in the subsequent sections.

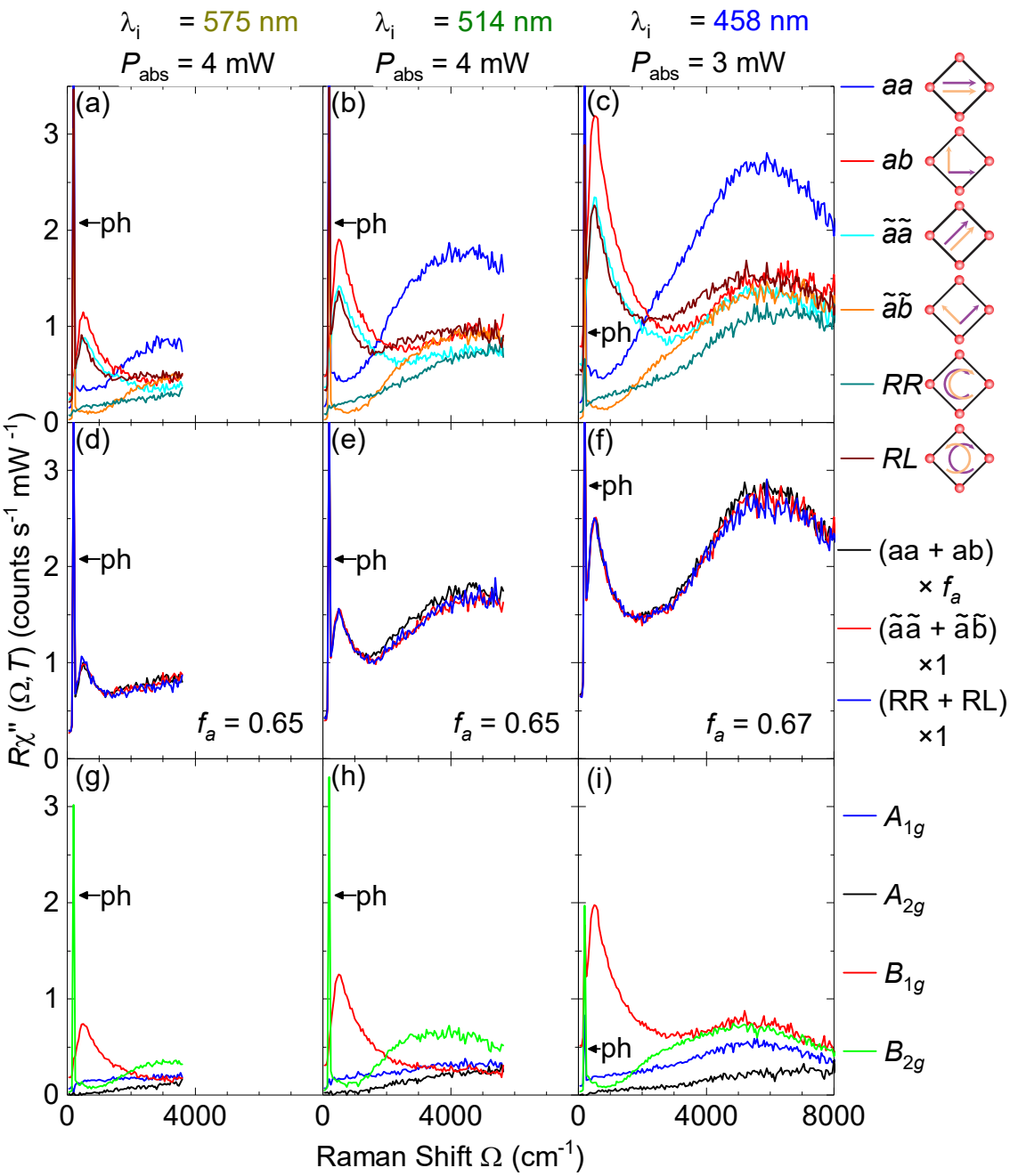

Figure 5.5: Raman spectra of FeSe at $T = 41\,\mathrm{K}$. (a-c) Raw spectra (normalized according to Sec. 3.3) measured with laser lines λ_i and absorbed power P_abs as indicated above. In spectra with $\lambda_\mathrm{i} \leq 514\,\mathrm{nm}$ a broad energy- and symmetry-dependent peak emerges at large Raman shifts. (e-f) Sums of corresponding pairs of spectra including all four in-plane symmetries of the D_{4h} point group. The spectra with a polarization of the incident light were multiplied by a factor f_a as indicated to match the intensity of the other sums. (g-i) Pure symmetries derived from the spectra in panels (a-c) by taking into account the factor f_a. The additional high-energy excitation seen at $\lambda_\mathrm{i} \leq 514\,\mathrm{nm}$ mainly contributes to the B_{2g} and B_{1g} symmetries.

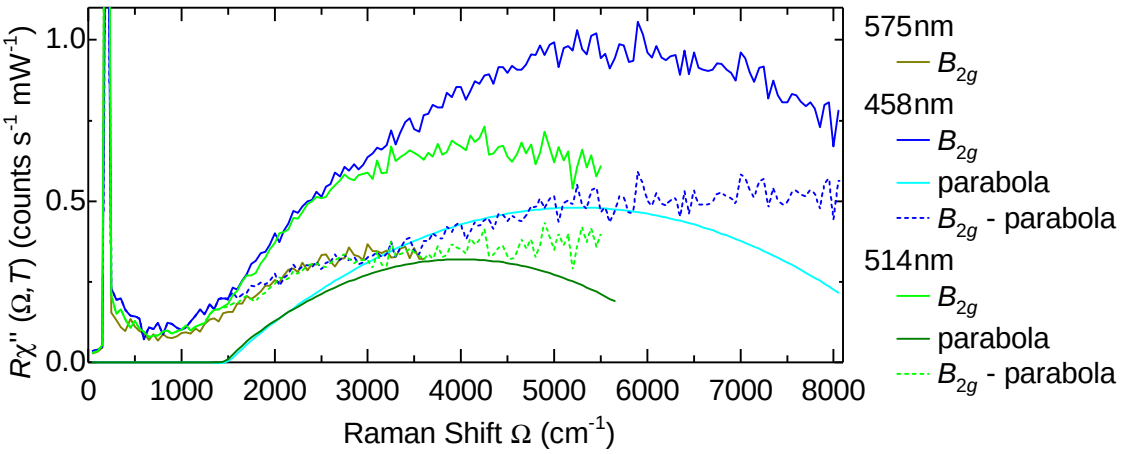

Figure 5.6: Luminescence contribution to the Raman spectra of FeSe in B_{2g} symmetry. Solid lines denote spectra for $\lambda_i = 575\,\mathrm{nm}$ (dark yellow), 514 nm (green), and 458 nm (blue). Above $\Omega \sim 1500\,\mathrm{cm}^{-1}$ the spectra for 514 nm and 458 nm exhibit an additional broad peak which can be described qualitatively by a parabola with a cut-off at $\Omega = 1500\,\mathrm{cm}^{-1}$ (light blue and dark green lines). Subtracting these parabolas from the experimental results yields the spectra shown as dashed green and blue lines, respectively.

For luminescence originating from contaminants one typically expects transitions at fixed energies. This is not the case here as the centre of the peak (maxima of the parabolas) shifts by approximately $1200\,\mathrm{cm}^{-1}$ whereas the green and blue laser line differ by $2400\,\mathrm{cm}^{-1}$. Additionally, the luminescence peak exhibits a pronounced symmetry dependence as shown in Fig. 5.5(h-i). This suggests a crystalline environment. Defects at the crystal surface acting as colour centres may be a possible source for the observed luminescence.

Resonance of the response in B_{1g} symmetry

The Raman response in B_{1g} symmetry shows a strong dependence on the energy of the laser used for excitation [Fig. 5.5(g-i)]. The corresponding spectra are duplicated in Fig. 5.7(a). The peak height almost triplicates when the energy is increased from 2.2 eV ($\lambda_i = 575\,\mathrm{nm}$) to 2.7 eV ($\lambda_i = 458\,\mathrm{nm}$). Multiplying the spectra so as to match the peak height [Fig. 5.7(b)] shows that the peak shape is independent of the excitation energy. This indicates that the resonance condition is met only for a single transition involved in the Raman process (Fig. 3.1).

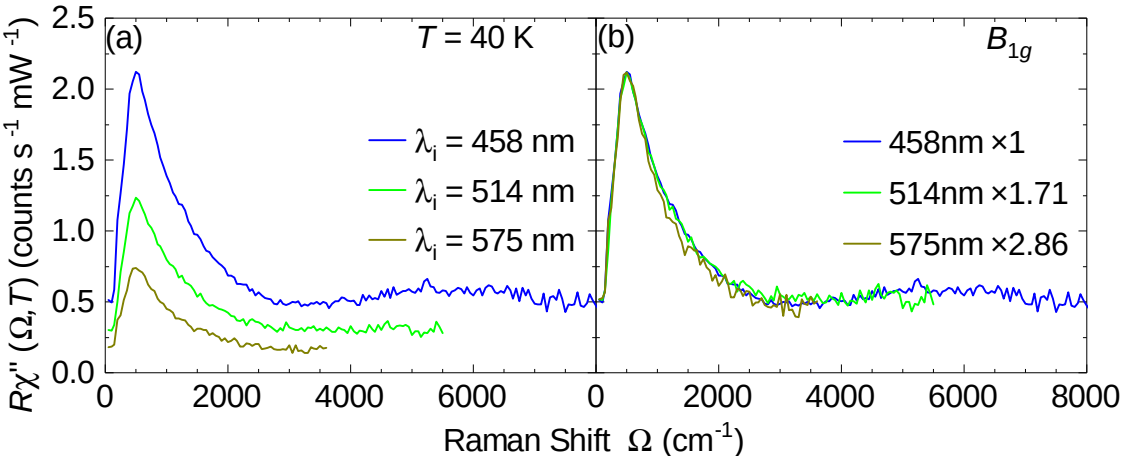

Figure 5.7: Resonance behaviour of the response in B_{1g} symmetry. (a) Spectra of FeSe showing pure B_{1g} symmetry for wavelengths λ_i of the exciting laser as given in the legend. The spectra are duplicated from Fig. 5.5(g-i). (b) Spectra from panel (a) multiplied to match the peak intensity at 500 cm^{-1}. The peak shape is identical for all three laser lines.

5.3.2 Temperature dependence in all symmetries

Spectra up to 3600 cm^{-1} using the $\lambda_i = 575$ nm laser line were measured at 41 K, 91 K, and 301 K for all six polarizations in steps of $\Delta\Omega = 50\,\mathrm{cm}^{-1}$ with a resolution of $\Delta\tilde{\nu} \approx 20\,\mathrm{cm}^{-1}$. Additionally spectra up to 1000 cm^{-1} in steps of $\Delta\Omega = 5\,\mathrm{cm}^{-1}$ with a resolution of $\Delta\tilde{\nu} \approx 5\,\mathrm{cm}^{-1}$ were measured at 91 K and 301 K. The spectra for 91 K and 301 K are shown in Figs. 5.9(a), 5.8(a), 5.10(a), and 5.11(a). Panels (b) of these figures show the sums of corresponding pairs of spectra. The raw and summed spectra for 41 K are shown in Fig. 5.5(a) and (d). Each sum comprises the full set of in-plane symmetries (A_{1g} + A_{2g} + B_{1g} + B_{2g}) of the D_{4h} point group. Some pairs of spectra were multiplied as indicated to match the intensities. These factors were included when pure symmetries were derived as linear combinations of these spectra in Sec. 6.2.5.

5.3.3 Detailed temperature dependence of the B_{1g} channel

To study the excitations in B_{1g} symmetry spectra in ab polarizations were measured in the energy range from 5 cm^{-1} to 1000 cm^{-1} at 16 temperatures between 21 K and 301 K. The spectra are shown in Fig. 5.12. All spectra were measured with an absorbed laser power $P_{\mathrm{abs}} = 4$ mW using the laser line at $\lambda_i = 575$ nm for excitation. The resolution was set at $\Delta\tilde{\nu} \approx 5\,\mathrm{cm}^{-1}$ and data points were taken in steps of $\Delta\Omega = 5\,\mathrm{cm}^{-1}$ up to $\Omega = 250\,\mathrm{cm}^{-1}$ and in steps of 10 cm^{-1} for higher shifts.

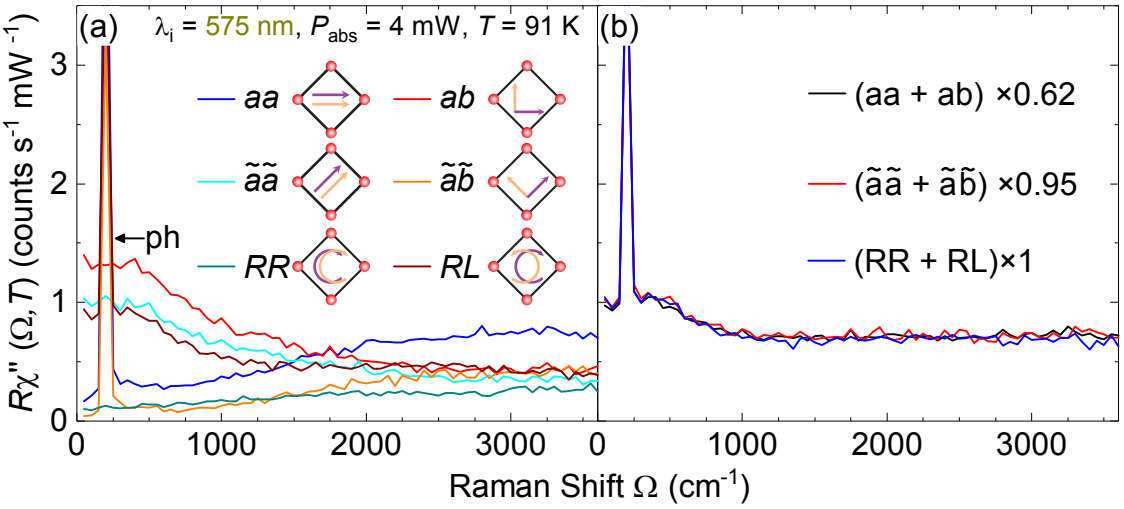

Figure 5.8: Raman spectra of FeSe at $T = 91\,\mathrm{K}$ measured using the $\lambda_\mathrm{i} = 575\,\mathrm{nm}$ laser line and an absorbed power of $P_\mathrm{abs} = 4\,\mathrm{mW}$. (a) Spectra for the polarizations as indicated. Violet and orange arrows denote the polarizations of the incident and scattered light, respectively. The sharp peak at $200\,\mathrm{cm}^{-1}$ comprises the Se and Fe phonon the shape of which is not resolved due to the coarse resolution. (b) Sums of complementary spectra, each comprising all four in-plane symmetries of the D_{4h} point group. The spectra are multiplied as indicated to match their intensities.

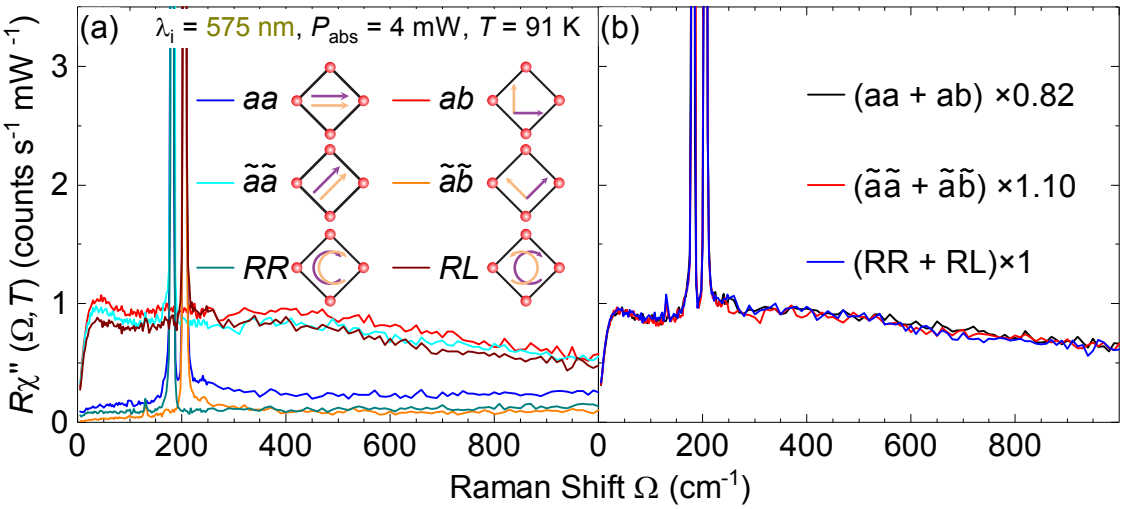

Figure 5.9: Raman spectra of FeSe at $T = 91\,\mathrm{K}$ measured using the $\lambda_\mathrm{i} = 575\,\mathrm{nm}$ laser line and an absorbed power of $P_\mathrm{abs} = 4\,\mathrm{mW}$. (a) Spectra for the polarizations as indicated. Violet and orange arrows denote the polarizations of the incident and scattered light, respectively. (b) Sums of complementary spectra, each comprising all four in-plane symmetries of the D_{4h} point group. The spectra are multiplied as indicated to match their intensities.

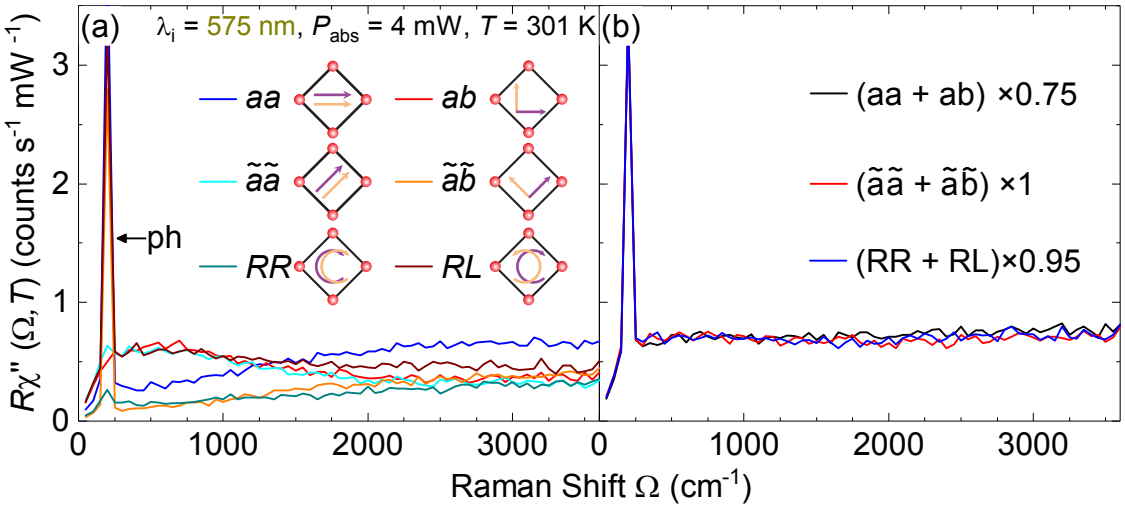

Figure 5.10: Raman spectra of FeSe at $T = 301\,\mathrm{K}$ measured using the $\lambda_\mathrm{i} = 575\,\mathrm{nm}$ laser line and an absorbed power of $P_\mathrm{abs} = 4\,\mathrm{mW}$. (a) Spectra for the polarizations as indicated. Violet and orange arrows denote the polarizations of the incident and scattered light, respectively. The sharp peak at $200\,\mathrm{cm}^{-1}$ comprises the Se and Fe phonon the shape of which is not resolved due to the coarse resolution. (b) Sums of complementary spectra, each comprising all four in-plane symmetries of the D_{4h} point group. The spectra are multiplied as indicated to match their intensities.

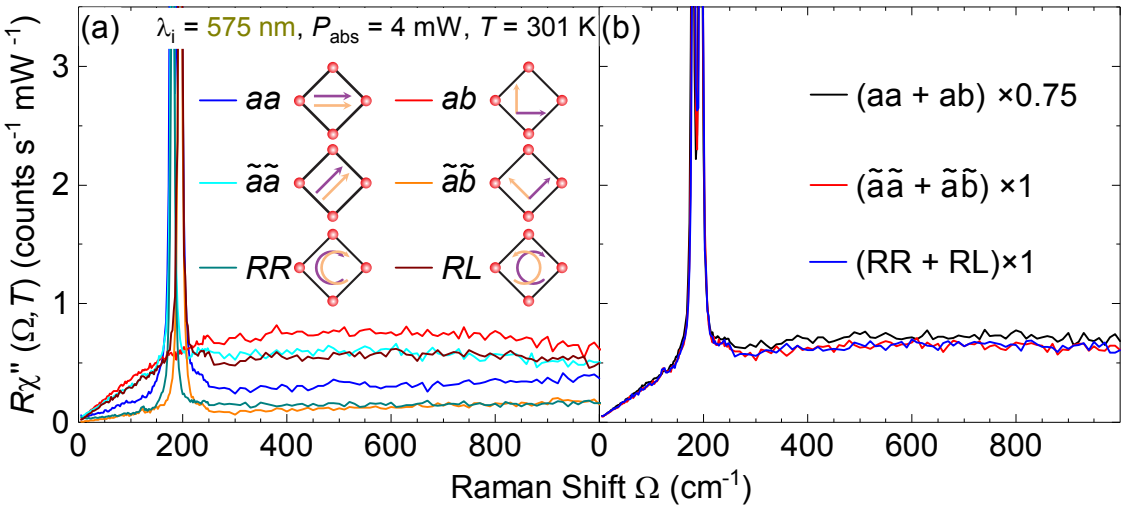

Figure 5.11: Raman spectra of FeSe at $T = 301\,\mathrm{K}$ measured using the $\lambda_\mathrm{i} = 575\,\mathrm{nm}$ laser line and an absorbed power of $P_\mathrm{abs} = 4\,\mathrm{mW}$. (a) Spectra for the polarizations as indicated. Violet and orange arrows denote the polarizations of the incident and scattered light, respectively. (b) Sums of complementary spectra, each comprising all four in-plane symmetries of the D_{4h} point group. The spectra are multiplied as indicated to match their intensities.

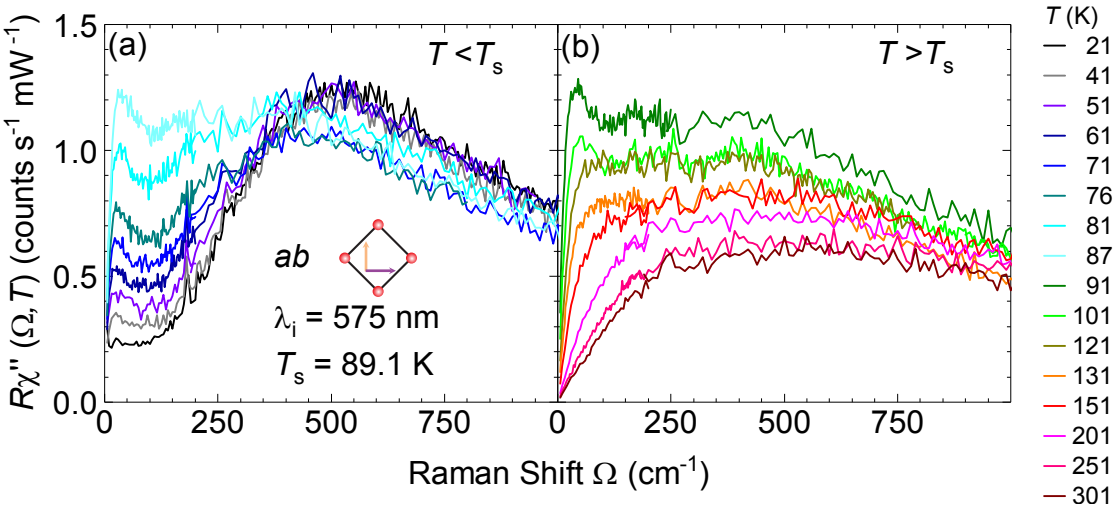

Figure 5.12: Raman spectra of FeSe in *ab* polarizations for temperatures (a) below and (b) above the structural phase transition T_s as given in the legend. The spectra comprise multiple excitations of different line width over the whole energy range all of them varying strongly with temperature.

At high temperature the spectra feature a broad maximum centred around $500\,\mathrm{cm}^{-1}$ which slightly softens when the temperature approaches T_s and hardens again below. Upon cooling from room temperature the spectral weight at $\Omega < 200\,\mathrm{cm}^{-1}$ increases continuously and a small peak forms which softens and reaches its maximum height at 91 K. Below T_s the peak softens further and the spectral weight below $250\,\mathrm{cm}^{-1}$ quickly decreases upon cooling. At $T < 76\,\mathrm{K}$ the Se phonon appears as sharp line at $180\,\mathrm{cm}^{-1}$.

5.3.4 Low-energy response in the A_{1g} channel

To investigate the response in A_{1g} symmetry at low energies, spectra in RR polarization in the range from $5\,\mathrm{cm}^{-1}$ to $350\,\mathrm{cm}^{-1}$ were recorded for temperatures from 40 K to 300 K (Fig. 5.13). The measurements were performed in steps of $\Delta\Omega = 2.5\,\mathrm{cm}^{-1}$ up to at least $\Omega = 200\,\mathrm{cm}^{-1}$ with a resolution of $\Delta\tilde{\nu} \approx 5\,\mathrm{cm}^{-1}$ to resolve narrow structures. Above the step width was increased to $\Delta\Omega = 10\,\mathrm{cm}^{-1}$. The spectra are dominated by the Se phonon at $180\,\mathrm{cm}^{-1}$ which surmounts the continuum by two orders of magnitude. The low intensity continuum is magnified in the inset. The sharp peak at $130\,\mathrm{cm}^{-1}$ is the low energy E_g phonon visible due to the finite projection of the R polarization on the sample c axis (cf. Sec. 4.1). Upon cooling from room temperature to T_s the spectral weight decreases above $200\,\mathrm{cm}^{-1}$ and increases below $130\,\mathrm{cm}^{-1}$. Below T_s the spectral weight below $130\,\mathrm{cm}^{-1}$ decreases.

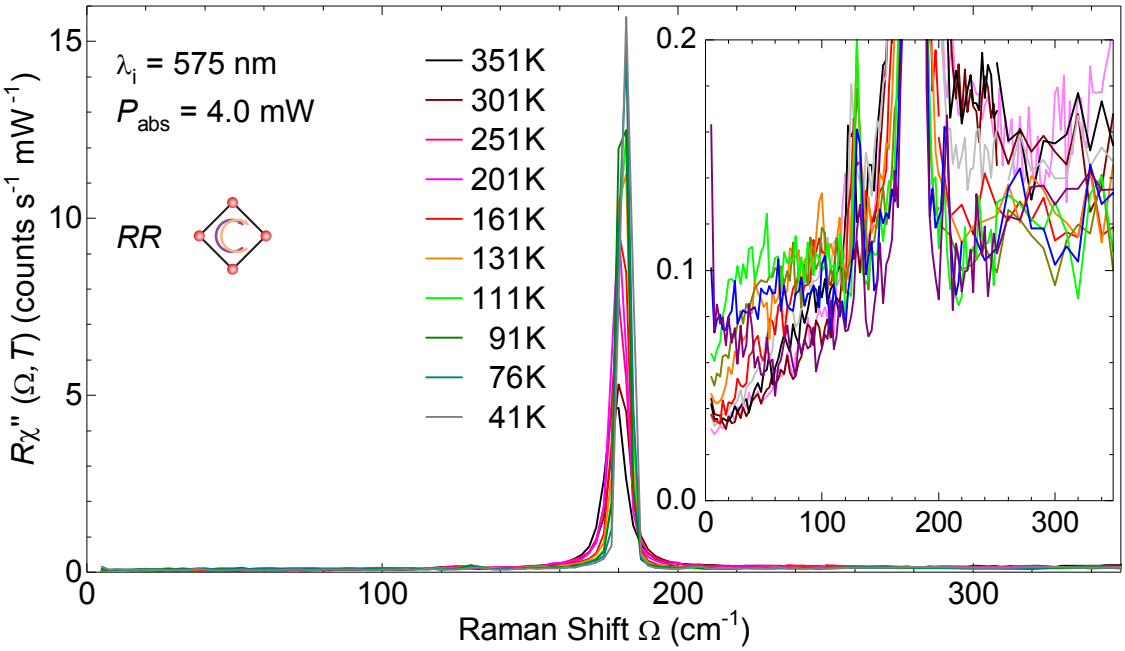

Figure 5.13: Raman spectra of FeSe in RR polarization for temperatures as given in the legend. The inset zooms in on the low energy continuum.

Chapter 6

Discussion

6.1 Interrelation of lattice, spins, and electrons

Lattice excitations were found to be useful probes of the various phases in the IBS [31, 151, 195–202]. Here phonons in FeS, $BaFe_2As_2$, and FeSe were studied with the main focus placed on their relationship to magnetic order. Using Raman spectroscopy the phonon energies and line widths as well as their symmetries were investigated as functions of temperature and excitation energy. From these properties a close connection of several phonon anomalies to spin order can be extracted.

6.1.1 Enhanced electron-phonon coupling and putative magnetism in FeS

The interest in tetragonal FeS increased when superconductivity below $T_c \approx 5\,\mathrm{K}$ was discovered in 2015 [35]. Unlike FeSe and FeTe, FeS remains tetragonal down to lowest temperatures [34]. The evidence for putative magnetic order is elusive. Moessbauer [109] and resistivity measurements as well as magnetic susceptibility [35] do not indicate any magnetic order. Short range magnetism is suggested by μSR [110, 111] and long range antiferromagnetic order was derived from neutron scattering [112].

Assignment of phonon modes

The $P4/nmm$ crystal structure of t-FeS enables four Raman-active phonon modes having symmetries $A_{1g} + B_{1g} + 2E_g$ [203]. Lattice dynamical calculations give their energies as shown in Table 6.1 [154]. Raman spectra of FeS at low energies for different light polarizations are shown in Fig. 6.1(a). Three peaks can be identified.

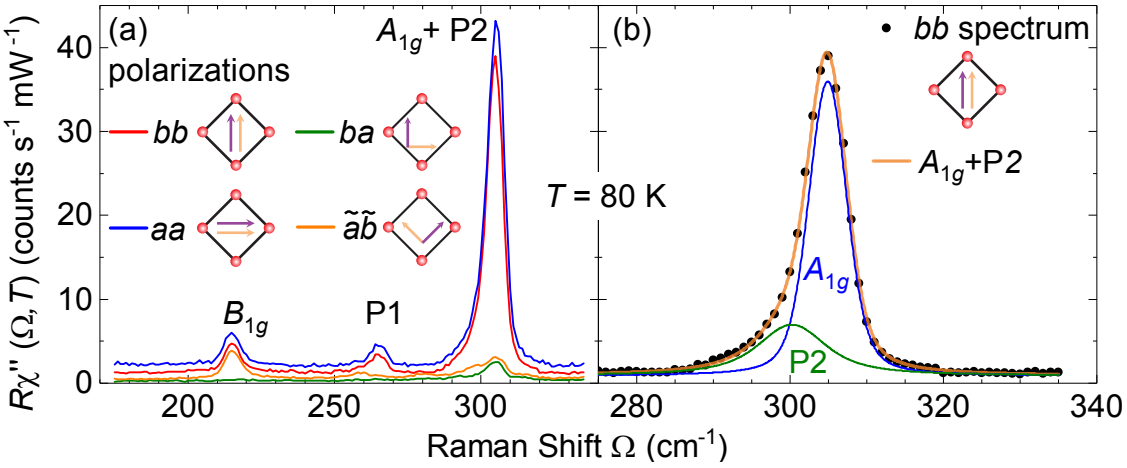

Figure 6.1: (a) Raman spectra of t-FeS at $T = 80\,\mathrm{K}$ with light polarizations as given in the legend. (b) Decomposition of the $305\,\mathrm{cm}^{-1}$ peak. Black dots are experimental data in bb polarization [red line in panel (a)]. The A_{1g} phonon and peak P2 are modelled by Voigt profiles (blue and green line, respectively). The sum of these profiles is shown as orange line.

The strongest peak at $\Omega = 305\,\mathrm{cm}^{-1}$ is asymmetric and is found to be composed of two peaks which cannot be resolved. These two peaks can be described by Voigt profiles which are shown as blue and green lines in Fig. 6.1(b). The strongest peak [blue line in Fig. 6.1(b)] at $305\,\mathrm{cm}^{-1}$ appears for parallel light polarizations indicating A_{1g} symmetry. It has some contribution in spectra measured with crossed polarizations due to leakage or from defect induced scattering. One can therefore identify this peak as in-phase vibration of sulphur atoms having A_{1g} symmetry. The symmetric peak at $215\,\mathrm{cm}^{-1}$ is found in all spectra except for ba polarizations. Hence it has B_{1g} symmetry and is identified as the out-of-phase vibration of Fe atoms. The energies of both phonon modes are shown in Table 6.1 and agree to within 4% with calculations using the experimental lattice parameters.

The remaining two peaks P1 and P2 cannot be identified trivially. Both appear in spectra measured with aa polarizations lacking a projection onto the c axis and thus neither can be one of the missing E_g phonons. Furthermore their energies would be significantly different from the calculated energies of the E_g modes given the good agreement found for the A_{1g} and B_{1g} phonons. Based on the selection rules P1 has pure A_{1g} symmetry as it appears only in spectra measured with parallel light polarizations. P2 has an additional contribution in the $\tilde{a}\tilde{b}$ spectrum indicating mixed $A_{1g} + B_{1g}$ symmetry.

More insight into the origin of these peaks can be gained from the temperature

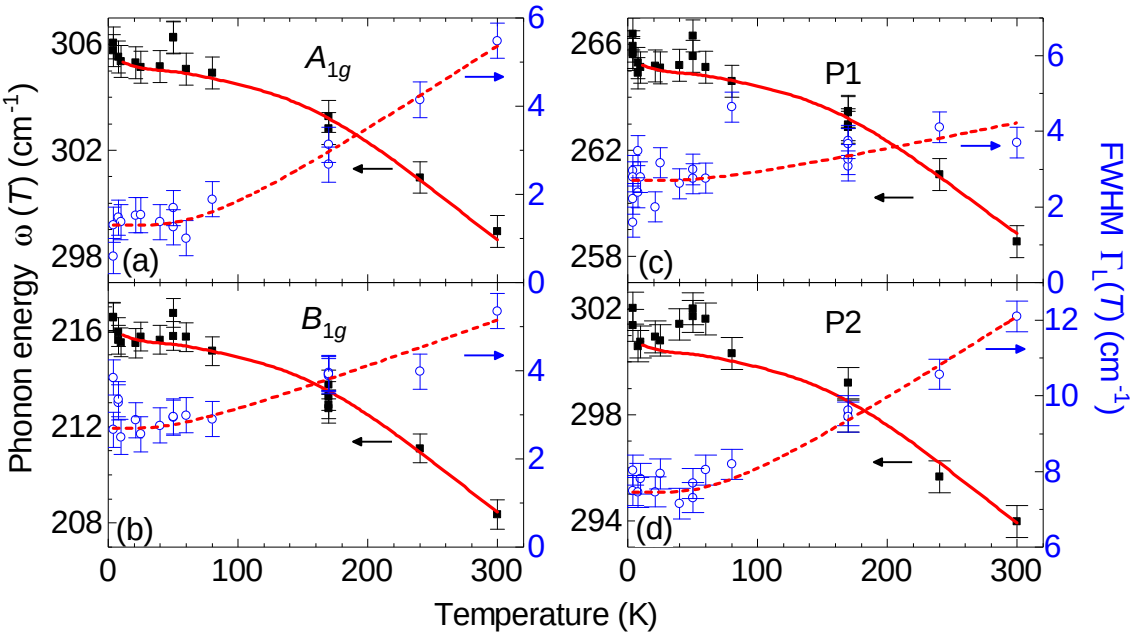

Figure 6.2: Temperature dependence of the four observed phonon modes. Black squares show the phonon energies ω, blue open circles denote the line width Γ_L. Dashed and solid red lines denote the temperature dependence of ω and Γ_L according to Eqs. 6.1 and 6.2, respectively.

dependence of the four modes. As can be seen from Fig. 5.2 all peaks harden and narrow upon cooling. By fitting Voigt profiles to the peaks the energies $\omega(T)$ and intrinsic (Lorentzian) line widths $\Gamma_\mathrm{L}(T)$ can be extracted and are plotted in Fig. 6.2. One can see that deviations from the prototypical monotonous hardening and narrowing occur at 50 K and below 20 K. Disregarding the anomaly at 50 K for now the temperature dependence of the line width Γ_L of all four modes above 20 K can be described by anharmonic decay into other phonon modes [154, 204]:

$$\Gamma_\mathrm{L}(T) = \Gamma_{\mathrm{L},0}\left(1 + \frac{2\lambda_{\mathrm{ph-ph}}}{\exp\left(\frac{\hbar\omega_0}{2k_\mathrm{B}T}\right) - 1}\right) \tag{6.1}$$

Here $\omega_0 = \omega(T \to 0)$ and $\Gamma_{\mathrm{L},0} = \Gamma_\mathrm{L}(T \to 0)$ are extrapolated from the data between 20 K and 50 K, leaving the phonon-phonon coupling $\lambda_{\mathrm{ph-ph}}$ as the only free parameter. The corresponding temperature dependences are shown in Fig. 6.2 as red dashed curves.

Temperature dependent changes to the phonon energy $\omega(T)$ stem from the anharmonic decay as well as from the lattice contraction and are given by [154, 205]

		Phonon energy ω_0 (cm^{-1})			
Mode	Symmetry	Calculation	Experiment	γ	λ_{ph-ph}
S	A_{1g}	316.1	305.3	2.2	1.68
Fe	B_{1g}	220.4	215.8	3.4	0.31
P1	A_{1g}		265.2	2.4	0.25
P2	A_{1g} +B_{1g}		300.5	2.2	0.31
Fe, S	E_g	231.6			
Fe, S	E_g	324.8			

Table 6.1: Mode denomination and atomic displacements, symmetries, calculated and experimental energies ω_0, Grüneisen parameter γ, and phonon-phonon coupling λ_{ph-ph} of the phonon modes in FeS.

$$\omega(T) = \omega_0 \left[1 - \gamma \frac{V(T) - V_0}{V_0} - \left(\frac{\Gamma_{L,0}}{\sqrt{2}\omega_0} \right)^2 \left(1 + \frac{4\lambda_{ph-ph}}{\exp\left(\frac{\hbar\omega_0}{2k_B T} \right) - 1} \right) \right]. \tag{6.2}$$

The unit cell volume data $V(T)$ and $V_0 = V(T \to 0)$ are taken from Ref. [34]. Using the phonon-phonon-coupling parameter λ_{ph-ph} as determined via Eq. 6.1 leaves a single parameter γ, the Grüneisen parameter, which is assumed to be temperature independent. The temperature dependences given by Eq. 6.2 are plotted in Fig. 6.2 as solid red lines. As $\omega_0 \gg \Gamma_{L,0}$ the influence of the anharmonic decay on the phonon energy is negligible.

The Grüneisen parameters γ and phonon-phonon coupling constants λ_{ph-ph} for all four modes are compiled in Table 6.1. One finds that the modes P1 and P2 exhibit Grüneisen parameters similar to that of the A_{1g} mode and close to the typical value of 2 [206] and that the phonon-phonon coupling λ_{ph-ph} parameters are quite similar for P1, P2, and the B_{1g} mode. λ_{ph-ph} for the A_{1g} mode is roughly six times as large and will be discussed below. The temperature dependences indicate that P1 and P2 are phononic in origin and hence can be caused by two processes: (1) In the presence of defects first-order Raman scattering can directly project the phonon density of states (PDOS) [179]. (2) In a second-order scattering process two phonon modes with momenta **k** and **-k**, thus maintaining the $|\mathbf{q}| \approx 0$ selection rule, are excited simultaneously and their energies add up, yielding a single peak in the spectra. Second order scattering requires either the presence of defects, thus

being accompanied by increased first order scattering [cf. case (1)], or enhanced electron-phonon coupling. To clarify the origin of P1 and P2 the phonon dispersion and PDOS were calculated [154] by M. Radonjić on the basis of the experimental lattice parameters[1] and are shown in Fig. 6.3(b). An important feature is a region without phonons between approximately 260 and 280 cm^{-1} and, correspondingly, a gap in the PDOS. As peak P1 is found within this gap it cannot originate from first-order scattering projecting the PDOS and may be identified as a two-phonon process.

While in general no selection rules apply to second-order processes [179] this is clearly not the case here. As a next step the selection rules for second-order processes on high symmetry points of the Brillouin zone (BZ) were determined by B. Nikolić [154], and one finds that pure A_{1g} symmetry can only be achieved by exciting two acoustic phonons of the same branch on a limited set of high-symmetry points or lines. Single points in the BZ can be excluded as they contribute with negligible phase space, leaving only the lines S, Σ, and V [see Fig. 6.3(a)]. The phonon branches along S and Σ concur with a very low PDOS. Along V a phonon branch has a flat dispersion, but is found at 150 cm^{-1}, i.e. 13% off of the expected $\omega_{\mathrm{P1}}/2 = 132.5\,\mathrm{cm}^{-1}$. However, calculations show [154] that phonon branches along $M' - A'$ [$M' = (0.4, 0.4, 0)$ and $A' = (0.4, 0.4, 0.5)$, see Fig. 6.3(b)] cause a high PDOS between 130 and 140 cm^{-1} whereas the contributions to B_{1g} and E_g symmetry can be considered small to negligible as the new line is very close to the high symmetry line V. Therefore peak P1 is found to be a two-phonon process most likely originating from two acoustic phonons from branches close to V.

The reasoning for peak P2 is similar. Assuming second-order scattering to cause P2, with the restriction to $A_{1g} + B_{1g}$ but not E_g symmetry, yields the branches along lines Δ and U as possible origin. However, these branches entail a rather low PDOS. As P2 is not found inside the gap of the PDOS defect-induced first-order scattering can also be considered as the source of this peak. Experimentally P2 is found at an energy slightly below the A_{1g} phonon. In fact, the theoretical PDOS exhibits a maximum at an energy slightly below the calculated energy of the A_{1g} phonon. Hence it is possible that P2 is the projection of this maximum of the PDOS by first-order defect-induced scattering. The low intensity of P2 in spite of the high PDOS would then explain why the contributions from defect-induced scattering are

[1] It was found that using the experimental lattice parameters for the calculations yields good agreement in the energies of the optical phonons (cf. Table 6.1) at the cost of non-linearities in the dispersion of the acoustical phonons. Relaxing the structure lifts those deviations, but the energies of the optical phonons change by 10% or more [154].

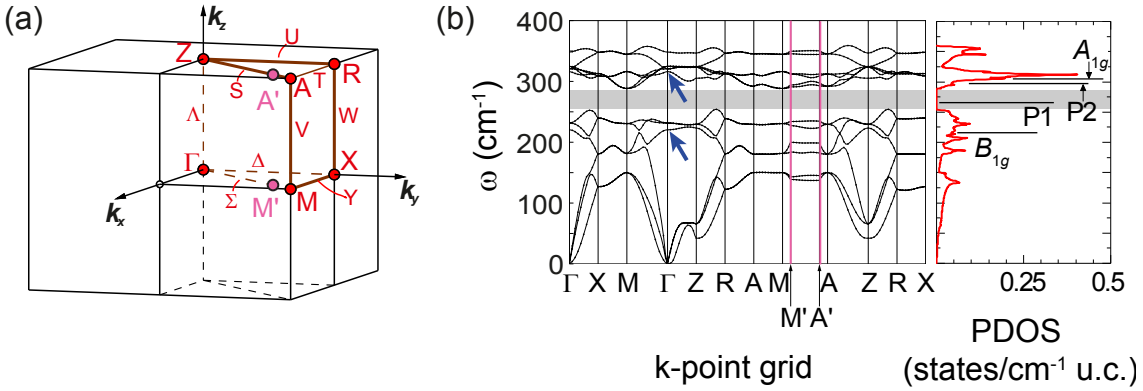

Figure 6.3: (a) Brillouin zone with high symmetry points and lines [207]. $M' = (0.4, 0.4, 0)$ and $A' = (0.4, 0.4, 0.5)$ are shown as magenta dots. (b) Phonon dispersion along the indicated directions and phonon density of states (PDOS). The grey shaded area marks a gap with zero PDOS. Blue arrows denote the two Γ-point modes observed experimentally. Black lines in the PDOS show the experimental energies. M' and A' are shown as magenta lines. Adopted from Ref. [154]

negligible at other energies. One may further speculate that the weak intensity found at the energy of the A_{1g} phonon in crossed polarizations (see Fig. 6.1) could also originate from a projection of the high PDOS in this energy range.

Phonon-phonon and electron-phonon coupling

Among the parameters compiled in Table 6.1 the phonon-phonon coupling $\lambda_{\mathrm{ph-ph}}^{(A_{1g})}$ of the Raman-active sulphur mode is noticeable as it is almost six times as large as $\lambda_{\mathrm{ph-ph}}$ for the other three observed modes. If one assumes a rather symmetric decay of the A_{1g} phonon the resulting modes have energies close to those which form the two-phonon peak P1. The latter process also requires a substantial phonon-phonon coupling.

Phonon-phonon coupling exists in all materials due to the anharmonicity of the phonon potential and can be enhanced by defects [208]. As FeS is metallic [35] an additional channel exists by coupling phonons indirectly via the electrons. One may speculate that the high $\lambda_{\mathrm{ph-ph}}^{(\mathrm{A_{1g}})}$ is indicative of a likewise enhanced electron-phonon coupling $\lambda_{\mathrm{el-ph}}$. Assuming $\lambda_{\mathrm{el-ph}}$ to be the dominant contribution gives the approximation $\lambda_{\mathrm{ph-ph}}^{(\mathrm{A_{1g}})} \propto \lambda_{\mathrm{el-ph}}^2$ and consequently $\lambda_{\mathrm{el-ph}} \sim 0.5 - 1.3$ in FeS. To put this into context the calculated values for $\lambda_{\mathrm{el-ph}}$ in iron pnictides are $\lambda_{\mathrm{el-ph}} \sim 0.2 - 0.35$ [159, 160] and account for critical temperatures $T_c < 1\,\mathrm{K}$ only. Experimentally $\lambda_{\mathrm{ph-ph}} \approx 0.1$ [151] and $\lambda_{\mathrm{el-ph}}^2 < 5 \cdot 10^{-2}$ [209, 210] were found in Ba-122. Beyond the IBS, studies of MgB_2 yield $\lambda_{\mathrm{ph-ph}} \approx 0.9$ for the E_{2g} mode [211], thus $\lambda_{\mathrm{ph-ph}}^2 \approx 0.8$.

This exceeds $\lambda^2_{\mathrm{el-ph}} \approx 0.4$ [212], although MgB_2 is believed to be a conventional superconductor, i.e. Cooper pairing is based on the electron-phonon interaction. Therefore one may speculate that an enhanced $\lambda_{\mathrm{el-ph}}$ may even account for $T_c \approx 5\,\mathrm{K}$ in FeS. In the light of recent theoretical [168] and experimental studies [163, 167, 213] indicating a nodal superconducting gap having d-wave or $s + d$-wave symmetry, it is, however, unlikely that electron-phonon coupling is the only interaction leading to Cooper pairing in FeS. It may still provide a fully symmetric contribution in addition to the d-wave type coupling while for the latter spin fluctuations are a frequent candidate for IBS [33, 83, 171, 172].

Phonon anomalies and magnetic order

While the overall temperature dependence shown in Fig. 6.2 is well described by anharmonic decay and lattice contraction, two anomalies are found. At 50 K the energies of all four modes show an abrupt increase, but return to the values calculated from the unit cell volume for both higher and lower temperatures. This discontinuous behaviour could be reproduced in multiple measurements for the A_{1g} sulphur phonon and the P2 mode, but the values scatter for the B_{1g} Fe and P1 modes. No sudden changes in the lattice constants are found at this temperature [34] and neither measurements of the resistivity [35] nor μSR [110, 111] hint towards a phase transition. The magnetic susceptibility appears to depend strongly on the applied field and exhibits a maximum around 50 K for applied fields $H \leq 500\,G$ [112]. In the same study the scattering intensity from neutron powder diffraction shows a discontinuity in the temperature dependence at 50 K. Only more detailed studies can clarify whether or not the anomaly at 50 K has a magnetic origin. In the same study [112] magnetism with an ordering vector $\mathbf{q} = (0.25, 0.25, 0)$ was found below $T_N = 116\,\mathrm{K}$. No anomalies of the phonons are found in this temperature region, even when measured in smaller temperature increments of 10 K [154]. A small kink in the temperature dependence of the c-axis length can be seen in the XRD data [34], which may be related to the onset of magnetic order but has no discernible effect on the unit cell volume and therefore does not affect the phonon energies.

Below $T^* \approx 20\,\mathrm{K}$ all four observed modes show an abrupt increase in energy. The changes of the line width Γ_L are non-uniform in that the B_{1g} phonon broadens whereas the A_{1g} phonon tends to narrow. No clear changes are seen for the modes P1 and P2. The change in energy reflects the XRD data where an additional decrease in unit cell volume below 20 K is found [34]. No phase transition at this temperature has been reported so far, but a μSR study found short range magnetic order below

T^* [110].

Phonon anomalies related to the onset of long range magnetic order were found in several IBS whereas the temperature dependence of the phonons is continuous in materials without long-range order [214, 215]. In the 122 systems the A_{1g} As phonon softens upon entering the SDW state, whereas the B_{1g} Fe phonon shows no notable change in energy. Both modes narrow substantially when magnetic order is established [151]. The coupling of the A_{1g} phonon to the magnetic order was found to originate from a strong interrelation of the Fe magnetic moment and the z position of the As atom [98], which is modulated by the A_{1g} mode. At the onset T_N of the more localized magnetism in FeTe [107, 143] the B_{1g} Fe phonon softens and narrows, whereas the A_{1g} Te mode is largely unaffected except for a small kink in energy at T_N and a small broadening [195–197]. In all cases the affected phonons soften. In contrast, in FeS all four modes harden rather uniformly below T^*, hence the short range magnetic order found by μSR appears to be different from the localized as well as the itinerant magnetism found in the other IBS.

The two μSR studies differ in the interpretation of the disordered magnetism in that Ref. [110] found a very low magnetic moment of $10^{-2} - 10^{-3}\mu_B$, much lower than in the itinerant material $BaFe_2As_2$ [73] or the more localized FeTe [107]. In the second μSR study [111] the results were interpreted as incorporation of a small percentage $\sim 1\%$ of magnetic moments of $\sim 1\mu_B$ which is consistent with findings by core level photoemission spectroscopy [216]. Theoretical works yield even higher moments up to $2.7\mu_B$ [216] and the reduction of the experimental moment with respect to the theoretical ones was attributed to strong spin fluctuations.

6.1.2 Phonon anomalies in de-twinned $BaFe_2As_2$

Phonons can also be used to probe the band structure by measurements using variable energies of the exciting photons. In $BaFe_2As_2$, multiple anomalies of the Raman active phonons related to nematicity and magnetic order have been observed. For the low energy $E_g^{(1)}$ mode [Fig. 2.3(c)] an unexpectedly large splitting between the resulting $B_{2g}^{(1)}$ and $B_{3g}^{(1)}$ modes was observed when the degeneracy is lifted below T_s [152]. The A_{1g} As mode [Fig. 2.3(a)] exhibits a jump in energy and a narrowing by a factor of three below $T_s \approx T_{SDW} \approx 135\,K$ [151]. Additionally, this mode can be observed in spectra with crossed light polarizations having substantial intensity below T_s [113]. In this work the study of these phonon anomalies was extended by using a mechanically de-twinned sample of $BaFe_2As_2$ [97], which enables the unambiguous definition of the projected symmetries as well as the observation of anisotropies. The

experimental results then are compared to calculations which include the stripe-like magnetic order. These calculations were done by Y. Li, M. Tomić, I. I. Mazin, and R. Valentí, and were published along with the experiments [86].

E_g phonon splitting

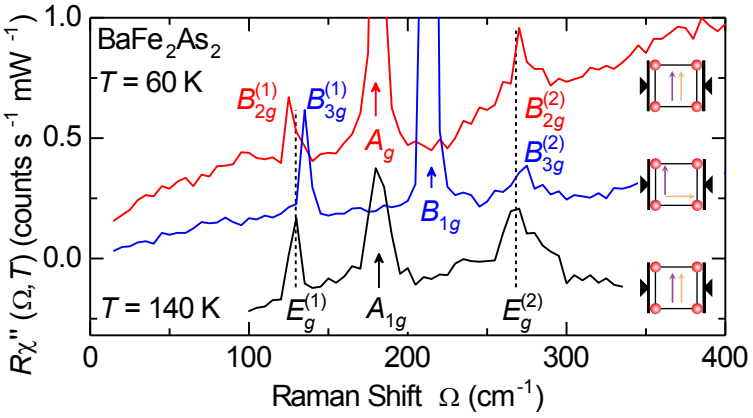

Figure 6.4: Phonons in detwinned $BaFe_2As_2$. The spectra at 60 K $< T_s$ (red and blue lines) are displayed with the experimental intensity. The spectrum at 140 K $> T_s$ (black line) is shifted down by 1.4 counts s^{-1} mW^{-1} for clarity. The tetragonal E_g phonons (vertical dashed lines) split below T_s. The resulting $B_{2g}^{(1)}$ and $B_{3g}^{(1)}$ peaks appear at distinct positions for polarizations of the scattered light parallel (blue) and perpendicular (red) to the applied pressure as indicated in the insets. The $B_{2g}^{(2)}$ and $B_{3g}^{(3)}$ phonons are shifted only slightly upwards with respect to the $E_g^{(2)}$ mode. Orange and violet arrows in the insets indicate the polarizations of the incident and scattered photons, respectively. The black triangles indicate the direction of the applied pressure. The shorter $\tilde{b}$ axis is parallel to the stress. Adapted from Refs. [97] and [86].

The transition from the tetragonal to the orthorhombic crystal structure lifts the degeneracy of the E_g modes. As the orthorhombic crystal axes $\tilde{a}$ and $\tilde{b}$ differ by approximately 0.7% [23], a slight difference in the energies of the resulting B_{2g} and B_{3g} modes can be expected. Previous studies on twinned crystals [152, 217, 218] found, however, that the splitting for the low energy $E_g^{(1)}$ mode is as large as 10 cm^{-1} or about 8% of the phonon energy. Measurements on twinned crystals show the B_{2g} and B_{3g} modes in a single spectrum which hence cannot be identified unambiguously. The measurements on mechanically de-twinned crystals shown in Fig. 6.4 overcome this limitation. Here, the low energy $B_{2g}^{(1)}$ and $B_{3g}^{(1)}$ modes can be observed in separate spectra, distinguished by the choice of polarization for the scattered light. The polarization of the incident light $\mathbf{e}_i||\tilde{a}$ entails the necessary c-

$I4/mmm$				$Fmmm$		
	Exp. (140 K)	Theory			Exp. (60 K)	Theory
A_{1g}	180	168	$\longrightarrow$	A_g	180	172
B_{1g}	215	218	$\longrightarrow$	B_{1g}	215	221
$E_g^{(1)}$	130	140	$\nearrow$	$B_{2g}^{(1)}$	125	110
			$\searrow$	$B_{3g}^{(1)}$	135	133
$E_g^{(2)}$	268	290	$\nearrow$	$B_{2g}^{(2)}$	270	272
			$\searrow$	$B_{3g}^{(2)}$	275	287

Table 6.2: Raman-active phonons in $BaFe_2As_2$. The experimental and theoretically determined energies [86] are given in cm^{-1}. In addition, the symmetry correlations between the tetragonal ($I4/mmm$) and orthorhombic ($Fmmm$) structures are shown.

axis projection (see Fig. 4.2). As the orientation of the longer and shorter crystal axes, $\tilde{a}$ and $\tilde{b}$, respectively, is fixed by the applied pressure (black triangles in the insets of Fig. 6.4) the symmetries can be assigned correctly. The red spectrum in Fig. 6.4 comprises $\tilde{a}\tilde{a}$ and $c\tilde{a}$ polarizations and thus projects the symmetries A_g and B_{2g}. This is confirmed by the As phonon at $180\,cm^{-1}$ appearing in this spectrum. Correspondingly, the blue spectrum comprises B_{1g} and B_{3g} symmetries projected by the $\tilde{a}\tilde{b}$ and $c\tilde{b}$ polarization contributions, respectively, and the Fe phonon at $215\,cm^{-1}$ can be seen. One can therefore assign the lower energy branch of the split $E_g^{(1)}$ mode, found at $125\,cm^{-1}$ in the red spectrum, as the related non-degenerate $B_{2g}^{(1)}$ contribution. Accordingly, the high energy branch at $135\,cm^{-1}$ appears in the blue spectrum and thus has B_{3g} symmetry. Comparing these energies to the theoretical values in table 6.2 shows a good agreement, although the splitting is overestimated in the calculations.

The same assignment of symmetries can be done for the $E_g^{(2)}$ mode, found at $268\,cm^{-1}$ in the tetragonal phase. Here, the theoretically predicted splitting is smaller than for the $E_g^{(1)}$ mode, but still overestimates the experimentally found value $\left(\Omega^{B_{3g}^{(2)}} - \Omega^{B_{2g}^{(2)}}\right) \leq 5\,cm^{-1}$.

The energies and eigenvectors $Q^{(\nu)}$ of all phonon modes were calculated for the high-temperature paramagnetic and the low-temperature ordered phase using *ab initio* DFT calculations. Details are given in Ref. [86]. The theoretical phonon energies, together with the symmetry relations between the phases and the experi-

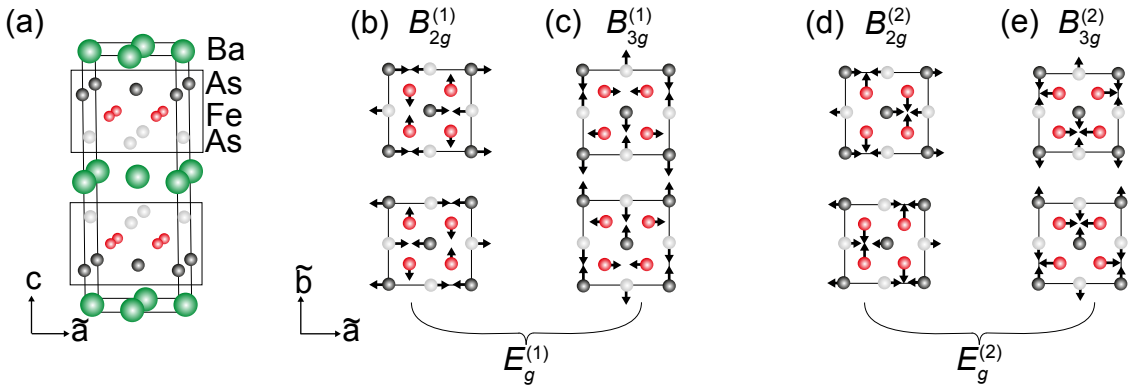

Figure 6.5: B_{2g} and B_{3g} phonon modes of $BaFe_2As_2$ in the orthorhombic unit cell $\tilde{a}\tilde{b}c$ shown in panel (a). The modes (b) $B_{2g}^{(1)}$ and (c) $B_{3g}^{(1)}$ result from the low energy $E_g^{(1)}$ phonon. (d) $B_{2g}^{(2)}$ and (e) $B_{3g}^{(2)}$ result from the high energy $E_g^{(2)}$ phonon. The length of the arrows qualitatively denotes the relative amplitudes of the atomic motion.

mental energies, are compiled in Table 6.2. The experimental and calculated energies agree to within 14%, with the deviation being less than 8% for most modes.

The eigenvectors for the tetragonal $I4/mmm$ phase are shown in Fig. 2.3. To obtain the experimental lattice parameters in a relaxed structure Néel-type order was imposed for the calculations in the tetragonal phase [47]. The eigenvectors for the As and Fe c-axis modes agree with previous calculations [219, 220] and remain unchanged upon entering the orthorhombic $Fmmm$ phase. Calculations for this phase consider the $(\pi, 0)$ magnetic stripe order on a square lattice, thus neglecting the small change of the lattice constants below T_s. The eigenvectors of the B_{2g} and B_{3g} phonons are shown in Fig. 6.5 and agree with previous results [220].

With the calculations for $(\pi, 0)$ stripe order on a square lattice showing good agreement to the experimentally observed modes one can conclude that the splitting of the low energy $E_g^{(1)}$ mode likely originates in the anisotropic magnetic order. The close link of the $B_{2g}^{(1)}$ and $B_{3g}^{(1)}$ modes to magnetism is further supported by previous work on the temperature dependence [194] which suggests that the splitting of the $E_g^{(1)}$ phonon occurs at the magnetic transition at T_{SDW}. The splitting between B_{2g} and B_{3g} modes is less pronounced for the high-energy $E_g^{(2)}$ phonon for the theoretical and experimental results. However, in the calculations the smaller splitting is accounted for by the different reduced mass of this mode with respect to the $E_g^{(1)}$ phonon [86]. The splitting in the experiment is close to the resolution limit and indicates an additional reduction relative to the theoretical values. To date, the source of this additional reduction remains unknown.

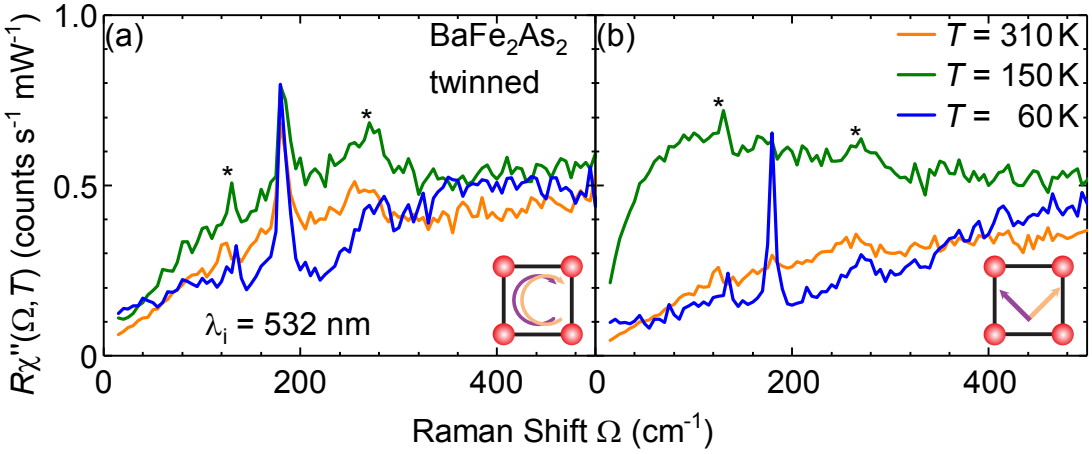

Figure 6.6: Raman spectra of twinned $BaFe_2As_2$ above (310 K, 150 K) and below (60 K) the magneto-structural transition at $T_s \approx T_{SDW} \approx 135\,K$ for (a) parallel (RR) and (b) crossed light polarizations (ab) as indicated by the insets. Asterisks mark the E_g modes discussed in Sec. 6.1.2. At $T = 60\,K < T_s$ the As phonon acquires intensity in crossed polarizations as reported before [113]. Data taken from Ref. [97]

As phonon intensity

A peculiar anomaly of the As phonon was found in the context of the selection rules, as the phonon line can be observed with considerable intensity in Raman spectra measured with crossed ab polarization for $T < T_{SDW}$ [113, 221]. This is shown in Fig. 6.6. In spectra measured with parallel light polarizations [RR, Fig. 6.6(a)] the As phonon is the strongest line at $180\,cm^{-1}$ at all temperatures and gains intensity upon cooling. In crossed polarizations [ab, Fig. 6.6(b)] the phonon is absent for $T > T_s$ as expected, but appears for $T < T_s$ (blue spectrum) with an intensity similar to that in RR polarization shown in panel (a). As both incident light polarizations (R and a) yield a projection onto the c axis the E_g phonons (asterisks), discussed in the previous section, are visible in all spectra. All phonon lines are superposed on a strongly temperature dependent continuum which was discussed in several previous studies [115, 118, 222, 223].

To illustrate the peculiarity of this high intensity in ab polarization it is helpful to have a look at the A_g Raman tensor

$$\hat{\alpha}^{(\mathrm{As})} = \begin{pmatrix} \hat{\alpha}_{11} & 0 \\ 0 & \hat{\alpha}_{22} \end{pmatrix}. \tag{6.3}$$

Here, only the in-plane elements are shown because the c-axis component $\hat{\alpha}_{33}$ is not projected in the experiment as the c-polarized contribution to the collected scattered light is negligible due to the small angle of acceptance of the collection

optics. Using this tensor the theoretical spectral weight of the phonon for different light polarizations ($\mathbf{e}_\mathrm{i}$,$\mathbf{e}_\mathrm{s}$) can be calculated according to Eq. 3.4.

This directly shows that in the tetragonal case, i.e. $\hat{\alpha}_{11} = \hat{\alpha}_{22}$, only parallel light polarizations ($\mathbf{e}_\mathrm{s}||\mathbf{e}_\mathrm{i}$) yield a non-zero response. When the crystal deforms orthorhombically the tensor elements become unequal ($\hat{\alpha}_{11} \neq \hat{\alpha}_{22}$) and non-zero intensity is expected for crossed polarizations $\mathbf{e}_\mathrm{s} \perp \mathbf{e}_\mathrm{i}$. This intensity depends on the difference between $\hat{\alpha}_{11}$ and $\hat{\alpha}_{22}$. Given that the orthorhombicity is small one would expect only a small difference. If the tensor elements would scale linearly with the orthorhombic distortion $2\frac{\tilde{a}-\tilde{b}}{\tilde{a}+\tilde{b}} \approx 0.7\%$ [23], one would expect only a fraction of about 10^{-4} of the spectral weight found in parallel polarizations to appear in crossed polarizations and not similar intensities in RR and ab (Fig. 6.6). This suggests a large anisotropy of the tensor elements and motivated the study of this phonon anomaly on a mechanically de-twinned sample where the squares of the tensor elements can be projected separately in $\tilde{a}\tilde{a}$ and $\tilde{b}\tilde{b}$ polarizations.

A large anisotropy of the spectral weights $A^{(\mathrm{As})}_{\tilde{a}\tilde{a}}$ and $A^{(\mathrm{As})}_{\tilde{b}\tilde{b}}$ was found together with a clear dependence on the energy $\hbar\omega_\mathrm{i}$ of the incident light [97]. Based on these findings the study was extended to the entire available range of $\hbar\omega_\mathrm{i}$ in collaboration with D. Jost [191] and F. Löffler [192]. From the spectra shown in Fig. 5.3 the spectral weight $A^{(\mathrm{As})}_{is}$ can be extracted and is plotted in Fig. 6.7(a) as a function of the excitation energy $\hbar\omega_\mathrm{i}$. Several measurements were repeated to check the reproducibility, and the variation of $A^{(\mathrm{As})}_{is}$ between those measurements can be considered an estimate of the experimental error. For parallel light polarizations along the antiferromagnetically ordered axis ($\tilde{a}\tilde{a}$, red squares) the spectral weight $A^{(\mathrm{As})}_{\tilde{a}\tilde{a}}$ increases continuously with increasing $\hbar\omega_\mathrm{i}$. In contrast $A^{(\mathrm{As})}_{\tilde{b}\tilde{b}}$ (blue squares) is lower at all energies and virtually constant at $\hbar\omega_\mathrm{i} < 2.7\,\mathrm{eV}$ before showing a steep increase at higher energies. The dependence of $A^{(\mathrm{As})}_{\tilde{a}\tilde{a}}$ and $A^{(\mathrm{As})}_{\tilde{b}\tilde{b}}$ on $\hbar\omega_\mathrm{i}$ displays a typical resonance behaviour [224], whereby the intermediate state $|\nu\rangle$ of the Raman scattering process (see Fig. 3.1) is an eigenstate of the electronic system. Then within second order perturbation theory a divergence of the scattering intensity as $|\hbar\omega_\mathrm{i} - E_0|^2$ is expected where E_0 denotes the energy difference between an occupied and an unoccupied Bloch state. In real systems the resonance profile is given by a Lorentzian and therefore Lorentzian functions (solid lines in Fig. 6.7) are used to approximate $A^{(\mathrm{As})}_{is}$ ($is = \tilde{a}\tilde{a}$ and $\tilde{b}\tilde{b}$). From these functions one can extract the resonance energies $E_{0,\tilde{a}\tilde{a}} = 3.1\,\mathrm{eV}$ and $E_{0,\tilde{b}\tilde{b}} = 3.3\,\mathrm{eV}$.

Using these Lorentzian profiles one can also make a prediction for the energy dependence of the spectral weight in other polarizations. To this end the Raman tensor

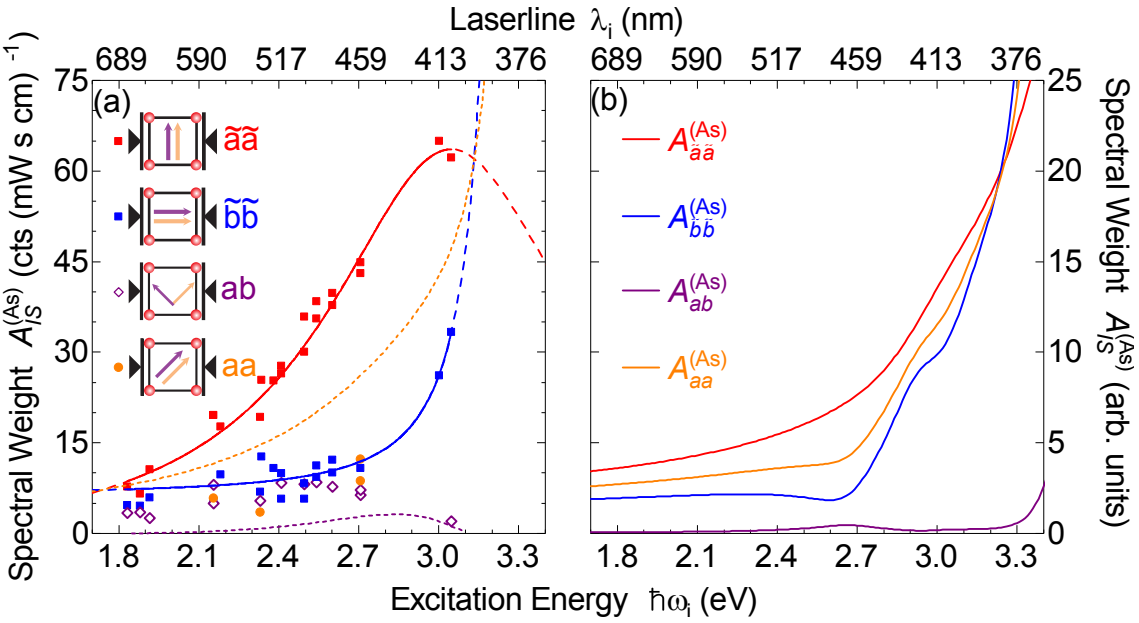

Figure 6.7: Spectral weight $A_{is}^{(\mathrm{As})}(\omega_\mathrm{i})$ of the As phonon as a function of excitation energy $\hbar\omega_\mathrm{i}$ and polarization. The top axis shows the corresponding wavelength λ_i of the exciting photons. (a) Experimental data. The intensity for parallel light polarizations along the ferromagnetically ordered axis ($\tilde{b}\tilde{b}$, blue squares) is virtually constant for $\hbar\omega_\mathrm{i} < 2.7\,\mathrm{eV}$ and shows a steep increase for higher energies. For light polarizations along the antiferromagnetically ordered axis ($\tilde{a}\tilde{a}$, red squares), the phonon intensity shows a monotonous increase with energy. The intensity for crossed (ab, purple diamonds) and for aa polarizations (orange dots) is comparable to the intensity found for $\tilde{b}\tilde{b}$ polarization. The solid lines are fits of Lorentzian functions whose extrapolations beyond the measured energy interval are shown as dashed lines. The purple dashed line is the intensity for ab polarization calculated from the fitted resonance profiles (solid lines) assuming a Raman tensor with real elements. The orange dashed line shows the same calculation for aa polarization. (b) Phonon spectral weight calculated from the theoretical Raman tensor [86]. The curves for $A_{\tilde{a}\tilde{a}}^{(\mathrm{As})}$ (red) and $A_{\tilde{b}\tilde{b}}^{(\mathrm{As})}$ (blue) qualitatively reproduce the experimental data shown in panel (a). For $A_{aa}^{(\mathrm{As})}$ (orange) and $A_{ab}^{(\mathrm{As})}$ (violet) the curves are closer to the predictions for a real Raman tensor [dashed lines in panel (a)].

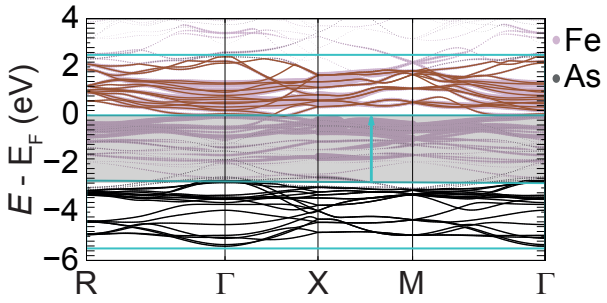

Figure 6.8: DFT band structure of $(\pi, 0)$ ordered $BaFe_2As_2$. Bands predominantly from Fe states are shown in brown and bands predominantly from As states in black. The shaded region from $-2.7\,\mathrm{eV}$ to E_F contains bands of mixed character and is blacked out for the calculation of the dielectric tensor. Only transitions between the bands within the turquoise frames are included. From Ref. [86]

$\hat{\alpha}^{(\mathrm{As})}$ is assumed to have purely real elements, and $\hat{\alpha}_{11} = \sqrt{A^{(\mathrm{As})}_{\tilde{a}\tilde{a}}}$ and $\hat{\alpha}_{22} = \sqrt{A^{(\mathrm{As})}_{\tilde{b}\tilde{b}}}$. From this tensor $A^{(\mathrm{As})}_{aa}$ and $A^{(\mathrm{As})}_{ab}$ can be calculated and are shown in Fig. 6.7(a) as dashed orange and violet line, respectively. Clearly there is no agreement with the experimental data, depicted by orange dots and open purple diamonds, for $\hbar\omega_\mathrm{i} < 3\,\mathrm{eV}$. Obviously the assumption of a Raman tensor having purely real elements does not hold at $T < T_\mathrm{SDW}$. From the clear overestimation of $A^{(\mathrm{As})}_{aa}$ and underestimation of $A^{(\mathrm{As})}_{ab}$ one has to conclude that the imaginary parts of $\hat{\alpha}_{11}$ and $\hat{\alpha}_{22}$ must have opposite sign.

The existence of an appreciable imaginary part of the Raman tensor indicates that absorption plays an important role in the scattering process. This, by itself, is not surprising and a complex Raman tensor was discussed for cuprates already two decades ago [225, 226]. For the IBS, however, this was not considered so far. A complex tensor implies that the effective mass approximation [174] cannot be used as it only yields real tensor elements.

Determining $\hat{\alpha}^{(\mathrm{As})}$ from the dielectric tensor, and in turn from the band structure, includes the imaginary parts of the tensor elements. However, for the calculations performed for this study an important limitation applies. The band structure computed within the framework of density functional theory (DFT) is shown in Fig. 6.8(a). The colours reflect the origin of the bands with those formed from Fe $3d$ orbitals shown in brown and those from As $4p$ orbitals shown in black. The bands below $-2.7\,\mathrm{eV}$ predominantly stem from As $4p$ orbitals, whereas Fe $3d$ orbitals prevail above E_F. The bands in between are of mixed character. For the calculations to be comparable to the experimental results the Fe bands need to be renormalized by a factor of $2 \ldots 3$ [227–230], whereas the band width of the As bands remains

unchanged. Therefore the bands above E_F can be renormalized and the bands below $-2.7\,\mathrm{eV}$ remain unchanged. The bands of mixed character in the range from $-2.7\,\mathrm{eV}$ to E_F are blacked out [shaded grey in Fig. 6.8(a)] as they cannot be renormalized in a simple way. To calculate the complex dielectric tensor $\hat{\varepsilon}_{ll} = \varepsilon'_{ll} + \imath\varepsilon''_{ll}$ transitions between the regions within the turquoise frames are included. The complex Raman tensor for the As phonon mode is given by the derivative of the dielectric tensor with respect to the phonon eigenvector $Q^{(\mathrm{As})}$ as

$$\hat{\alpha}_{ll} = \frac{\partial\varepsilon'_{ll}}{\partial Q^{(\mathrm{As})}} + \imath\frac{\partial\varepsilon''_{ll}}{\partial Q^{(\mathrm{As})}}. \tag{6.4}$$

The energy dependence of $A_{is}^{(\mathrm{As})}$ based on this Raman tensor is shown in Fig. 6.7(b). The anisotropic resonance behaviour for $\tilde{a}\tilde{a}$ (red line) and $\tilde{b}\tilde{b}$ (blue line) polarizations is well reproduced over the whole experimentally accessible energy range. For $\hbar\omega_\mathrm{i} \approx 2.9\,\mathrm{eV}$ there is a shoulder for $A_{\tilde{b}\tilde{b}}^{(\mathrm{As})}$ that is not captured in the experimental data due to a lack of laser lines. No agreement between the theoretical and experimental energy dependence is found for $A_{aa}^{(\mathrm{As})}$ (orange line)and $A_{ab}^{(\mathrm{As})}$ (purple line) for $\hbar\omega_\mathrm{i} < 2.7\,\mathrm{eV}$ due to the vanishing imaginary part of the calculated Raman tensor. Extending the theoretical framework to LDA+DMFT (local density approximation plus dynamical mean field theory) might provide a realistic imaginary contribution to scrutinize if the anisotropy of the tensor elements due to the resonance effect can account for the anomalous intensity in aa and ab polarizations.

With the $\tilde{a}$-$\tilde{b}$ anisotropy well captured by the calculations based on the band structure for the $(\pi, 0)$ magnetic phase one can conclude that the dominating reason for the anomalous intensity of the As phonon mode is the resonant behaviour, i.e. an effect of high energy electronic states. This is in contrast to a recent theoretical study [231] which proposed that the unexpectedly high intensity of the As phonon in ab polarization results from anisotropic changes to the low-energy band structure (near E_F) introduced by the stripe magnetic order.

The relationship of the intensity anomaly with magnetism is further supported by the studies of materials with well separated structural and magnetic phase transitions. In de-twinned $BaFe_2As_2$, where the structural and magnetic transition split up under uniaxial pressure, the As phonon shows an appreciable gain in spectral weight in $\tilde{a}\tilde{a}$ polarizations $\left[A_{\tilde{a}\tilde{a}}^{(\mathrm{As})}(T)\right]$ only at $T < T_\mathrm{SDW}$ [97]. The anomalously high intensity of this phonon mode in crossed polarizations can also be observed in $Ba(Fe_{1-x}Co_x)_2As_2$ where $T_\mathrm{s} > T_\mathrm{SDW}$. In $Ba(Fe_{1-x}Co_x)_2As_2$ ($x = 0.025$) the As phonon is visible in ab polarizations only at $T < T_\mathrm{SDW}$ [118].

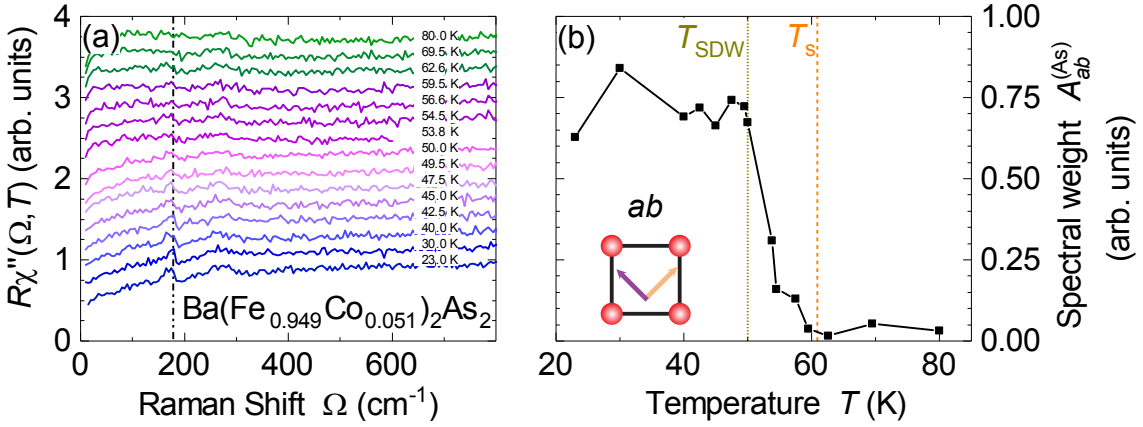

Figure 6.9: As phonon anomaly in $Ba(Fe_{1-x}Co_x)_2As_2$. (a) Raman spectra of $Ba(Fe_{1-x}Co_x)_2As_2$ ($x = 0.051$) in ab polarization at temperatures as indicated. The spectra are shifted for better visibility. The dash-dotted line shows the position of the As phonon. (b) Spectral weight $A_{ab}^{(\mathrm{As})}$ of the As phonon in ab polarization as a function of temperature. Dashed and dotted vertical lines denote T_s and T_SDW, respectively. From [86]

The temperature dependence for $Ba(Fe_{1-x}Co_x)_2As_2$ ($x = 0.051$) is shown in Fig. 6.9. The As phonon again appears in crossed ab polarization upon cooling. The temperature dependence of the spectral weight [Fig. 6.9(b)] reveals that the phonon appears already below T_s and grows in an almost linear fashion, but reaches its low temperature spectral weight only at T_SDW. This confirms that, while the phonon senses the structural distortion, it is indeed the magnetic transition that causes the high intensity in crossed polarizations.

FeSe, where only a nematic phase exists below $T_\mathrm{s} \approx 90\,\mathrm{K}$, is another candidate for providing a touchstone for this relationship. In FeSe, as visible in the spectra shown in Fig. 6.10(a), this phonon mode also appears in spectra with ab polarizations below the structural transition. The spectral weight $A_{ab}^{(\mathrm{Se})}$, shown in Fig. 6.10(b), shows a linear increase similar to that of the nematic phase for $T_\mathrm{SDW} < T < T_\mathrm{s}$ in $Ba(Fe_{1-x}Co_x)_2As_2$ ($x = 0.051$) shown above. In the absence of a magnetic transition there is no saturation of $A_{ab}^{(\mathrm{Se})}$. Most importantly, the spectral weight in crossed polarizations is only about 1% of the spectral weight found in parallel polarizations $\left[A_{RR}^{(\mathrm{Se})}\right]$. This is in contrast to the magnetically ordered state of $BaFe_2As_2$ and $Ba(Fe_{1-x}Co_x)_2As_2$, and further underlines that the magnetic order is at the root of the anomaly where $A_{\mathbf{e}_\mathrm{i}\perp\mathbf{e}_\mathrm{s}}^{(\mathrm{Se,As})} \approx A_{\mathbf{e}_\mathrm{i}||\mathbf{e}_\mathrm{s}}^{(\mathrm{Se,As})}$.

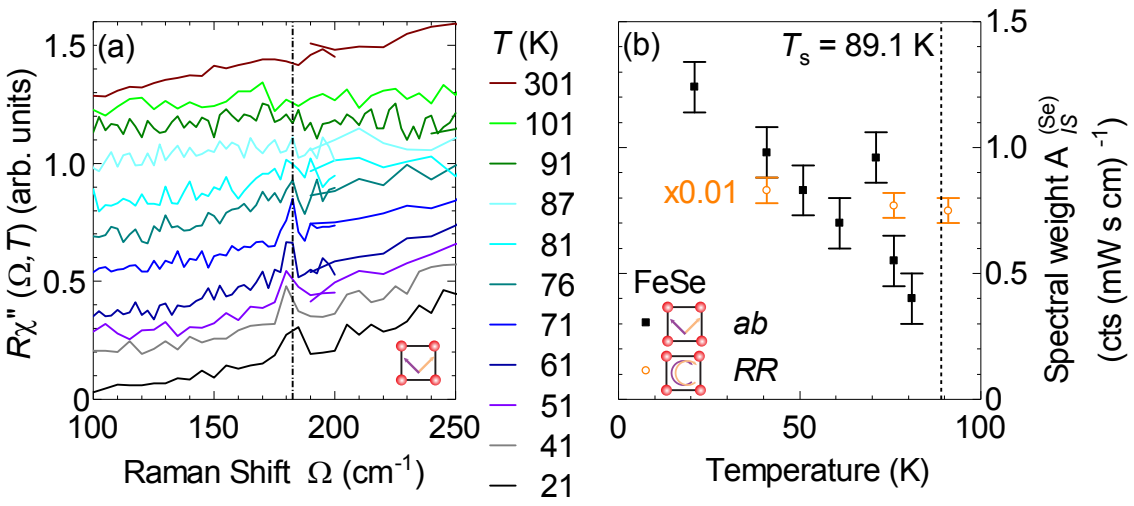

Figure 6.10: Se phonon in FeSe. (a) Raman spectra of FeSe in *ab* polarization at temperatures as given in the legend. The raw data are found in Fig. 5.12. The spectra are shifted for better visibility. The dash-dotted line shows the position of the Se phonon. (b) Spectral weight $A_{is}^{(\mathrm{Se})}$ of the Se phonon in for $is = ab$ and $is = RR$ polarizations as a function of temperature. The data for $A_{RR}^{(\mathrm{Se})}$, extracted from the spectra shown in Fig. 5.13, are multiplied by 0.01. The dashed vertical line denotes T_s.

6.2 Fluctuations and frustrated magnetism in FeSe

To clarify the magnetic ground state of FeSe it is insightful to start by relating the features seen in the Raman spectra to well known examples of localized and itinerant magnets shown in Fig. 6.11. Undoped insulating La_2CuO_4 can be considered a prototypical example of a Néel antiferromagnet of localized spins, the interaction of which can be described by the nearest-neighbour exchange interaction J. In the corresponding Raman spectra [Fig. 6.11(a)] the dominating feature is a peak in B_{1g} symmetry from two-magnon scattering [232–234]. This peak persists across the Néel temperature $T_\mathrm{N} \approx 325\,\mathrm{K}$ and hardens upon cooling.

Undoped $BaFe_2As_2$ is closer to the itinerant case. The material is metallic down to lowest temperatures [17]. Below $T_\mathrm{SDW} = 135\,\mathrm{K}$ magnetic $(\pi, 0)$ stripe order emerges, accompanied by a structural transition as elucidated in Chapter 2. While the high-energy spectra were interpreted in terms of two-magnon scattering [115] and a Heisenberg-type magnetism was considered in early theoretical works [144], the low energy B_{1g} spectra [Fig. 6.11(c)] are reminiscent of the formation of density wave type order [63, 113, 115, 235]. Upon cooling from room temperature a strong low-energy peak arises (with its maximum at $110\,\mathrm{cm}^{-1}$ in the green spectrum). This peak was identified as response from spin fluctuations and vanishes at T_SDW [118].

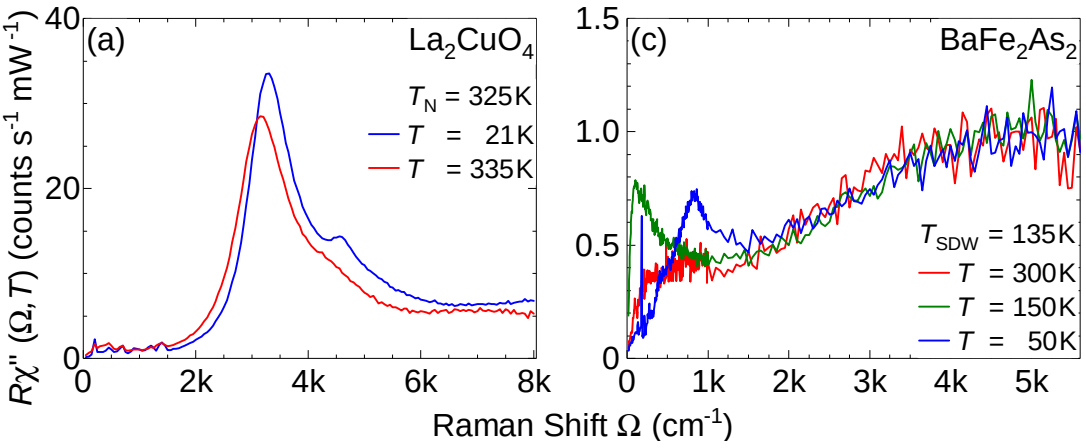

Figure 6.11: Raman spectra in B_{1g} symmetry of systems hosting localized and itinerant magnetic order, respectively. (a) The spectra of La_2CuO_4 are dominated by the two-magnon peak around 3200 cm^{-1} which hardens upon cooling. The second peak at $\Omega \approx 4500\,cm^{-1}$ in the blue spectrum is discussed in Ref. [232]. (b) The high temperature spectrum (red) of $BaFe_2As_2$ is smooth. Close to the magnetic transition (green) a strong low energy peak arises which was identified as spin fluctuations [118]. Below T_{SDW} (blue) a gap opens and spectral weight is shifted from $\Omega < 500\,cm^{-1}$ to a peak centred at $850\,cm^{-1}$. The sharp line at $180\,cm^{-1}$ is the As phonon discussed in Sec. 6.1.2. Above $2000\,cm^{-1}$ the B_{1g} spectra of $BaFe_2As_2$ are virtually temperature independent [114, 153]. Adopted from Refs. [114, 153, 232]

The origin of the magnetic order in $BaFe_2As_2$ is unlikely to be exchange coupling but rather an instability of the Fermi surface [138]. The ordering vector $(\pi, 0)$ is given by the nesting vector between hole and electron-like Fermi surface sheets [21, 117, 139].

The response in B_{1g} symmetry of FeSe [Fig. 6.12(c)] is composed of multiple excitations. The main feature is the broad peak centred around $500\,cm^{-1}$ which persists at all temperatures and gains intensity upon cooling. Its shape at high and low temperatures resembles the two-magnon excitation in the cuprates [Fig. 6.11(a)]. Close to the structural transition at $T_s \approx 90\,K$ (green spectrum) an additional excitation at energies $\Omega < 250\,cm^{-1}$ emerges. In contrast the response for all other symmetries is weak. In A_{2g} symmetry [Fig. 6.12(b)] it is temperature independent. For A_{1g} and B_{2g} symmetries [Fig. 6.12(a) and (d)] additional spectral weight is acquired below T_s shown as blue shaded areas. In A_{1g} the maximum appears at an energy slightly above the maximum of the B_{1g} peak similar to what is found in the cuprates [232]. In B_{2g} a suppression of spectral weight occurs (red shaded area) upon cooling from room temperature to T_s.

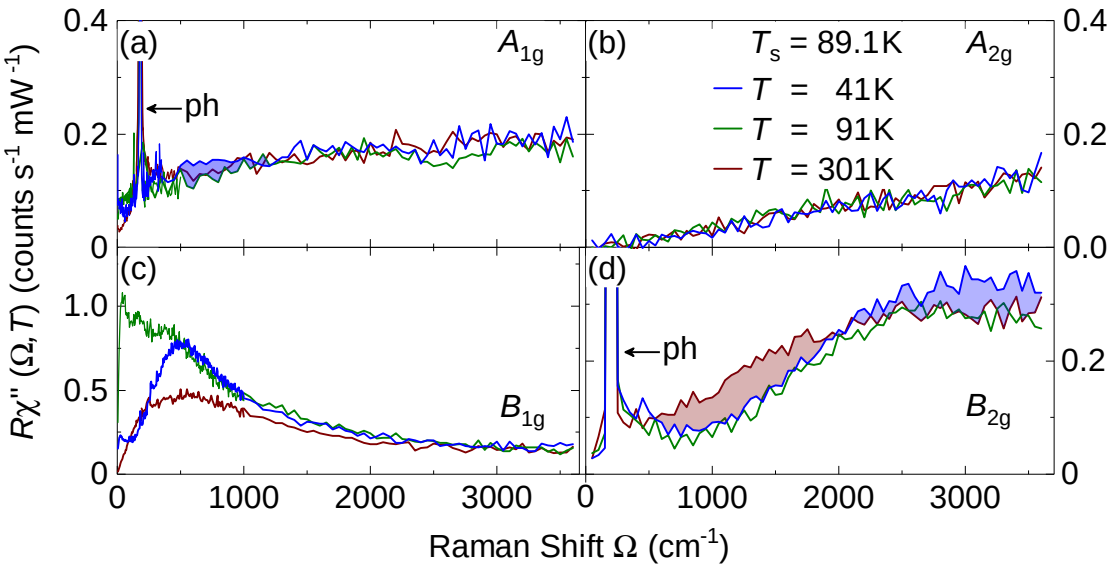

Figure 6.12: Symmetry resolved spectra of FeSe at temperatures as given in the legend. The spectra are linear combinations of the data shown in Figs. 5.5, 5.9, 5.8, 5.10, and 5.11. (c) The main effects occur in B_{1g} symmetry at energies below 1000 cm^{-1} where a broad peak centred at 500 cm^{-1} gains intensity upon cooling and an additional excitation below 250 cm^{-1} arises at intermediate temperatures (green). (a,d) Additional intensity in A_{1g} and B_{2g} symmetries is found at low temperatures (blue shaded areas). Already at higher temperatures a gap-like structure forms in B_{2g} in the range from 600 cm^{-1} to 1900 cm^{-1} (shaded red). (b) The response in A_{2g} symmetry is temperature-independent and weak.

6.2.1 Temperature dependence and decomposition of the response in B_{1g} symmetry

With the most noticeable effects occurring in B_{1g} symmetry the temperature dependence of these spectra merits a closer inspection. Fig. 6.13 shows *ab* spectra. As the contribution from A_{2g} symmetry [Fig. 6.12(b)] is negligible below 1000 cm^{-1}, the spectra here include virtually pure B_{1g} symmetry. Every spectrum comprises several excitations, which can be discriminated by their temperature dependences.

Upon cooling from ambient temperature an excitation at energies below 250 cm^{-1} arises and forms a sharp peak at 40 cm^{-1} for $T = 91$ K. Below T_s this peak quickly looses intensity but is still discernible at $T = 21$ K. The approximate position of the peak maximum is shown as grey shaded area above and as dashed line below T_s. The temperature dependence of this excitation resembles that found in $Ba(Fe_{1-x}Co_x)_2As_2$ [117, 118, 123].

The broad peak around 500 cm^{-1} slightly softens upon cooling as indicated by the blue arrow. Below T_s it hardens again and reaches its low temperature position at

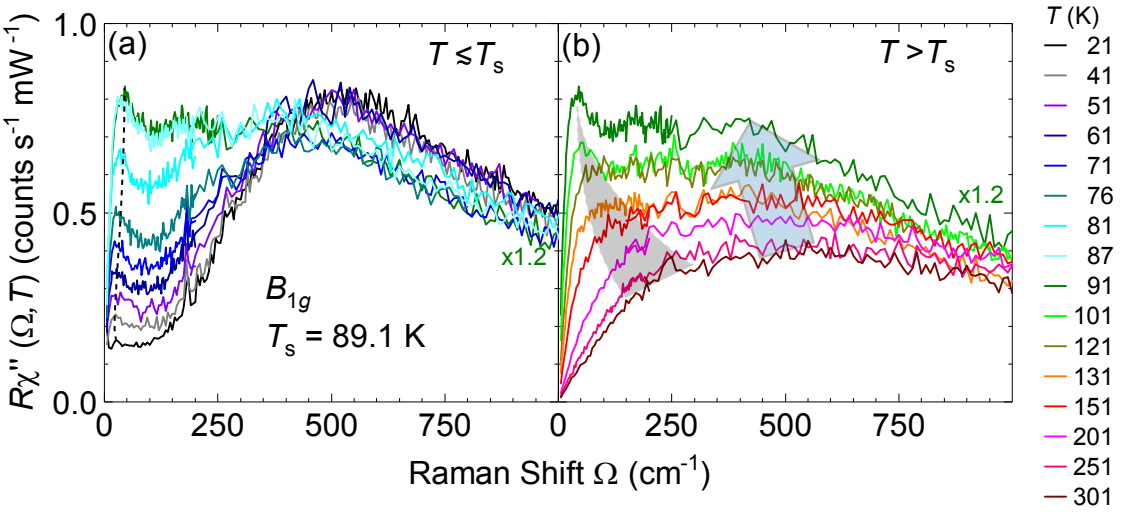

Figure 6.13: Spectra of FeSe in B_{1g} symmetry (a) below and close to, and (b) above the structural transition temperature $T_s = 89.1$ K. Temperatures as given are sample temperatures including the heating by the laser. The black dashed line in panel (a) and grey shaded area in panel (b) show the approximate position of the low energy ($\Omega < 250\,\mathrm{cm}^{-1}$) peak from fluctuations. The blue arrow indicates the approximate temperature dependence of the response from localized spins. Below T_s the Se phonon at $180\,\mathrm{cm}^{-1}$ is visible as sharp peak as discussed in Sec. 6.1.2.

$530\,\mathrm{cm}^{-1}$. This behaviour resembles the temperature dependence of the two-magnon excitation in cuprates [Fig. 6.11(a)].

As the contributions to the B_{1g} response can be discerned by their temperature dependence one can attempt a decomposition of the B_{1g} spectra as shown in Fig. 6.14. Three types of excitations are included:

(i) The existence of a continuum of electron-hole excitations is backed by the superconductivity induced changes to the spectra shown in Fig. 4.8. Here the B_{2g} response shown in the insets is used to obtain an analytic approximation for the particle-hole spectrum in B_{1g} symmetry (blue dashed lines)

(ii) Based on its temperature dependence shown above the low energy excitation ($\Omega < 250\,\mathrm{cm}^{-1}$) can be identified as response from fluctuations diverging at or slightly below T_s. Different types of fluctuations having finite momentum as entailed by the B_{1g} Raman vertex [118] can be considered such as quadrupolar fluctuations [124, 126]. In the collision-limited regime the momentum of the fluctuations can be carried away by impurities [119]. In the clean limit the excitation of a pair of fluctuations having opposing momenta to maintain the $\mathbf{q} \approx 0$ selection rule was considered by Caprara *et al.* [181]. Based on their work the response from fluctuations is modelled using Aslamazov-Larkin

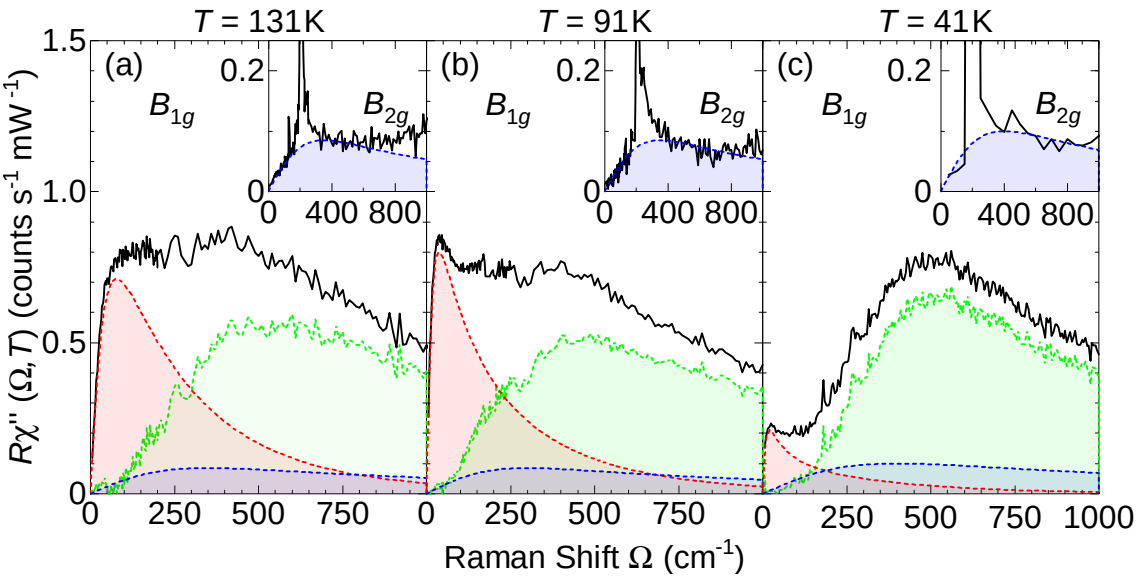

Figure 6.14: Decomposition of the B_{1g} spectra for temperatures (a) above, (b) at, and (c) below the phase transition at $T_s = 89.1\,\mathrm{K}$. Experimental spectra are shown as black lines. The inset shows the B_{2g} spectra at the corresponding temperature and an analytic approximation to the electron-hole continuum (dashed blue line), which is also used for B_{1g} symmetry. The low energy peak from fluctuations is modelled via AL-type diagrams (red). Subtracting these two contributions from the experimental B_{1g} spectra recovers the approximate shape of the response from localized spins (green).

(AL) type diagrams, suitable for charge and spin excitations [118, 181], and is shown in red. The temperature dependence is captured qualitatively with the contribution from fluctuations reaching its maximum close to T_s. The apparent opening of a gap at $\Omega < 250\,\mathrm{cm}^{-1}$ in the B_{1g} spectra below T_s can be attributed to the diminishing spectral weight from this contribution.

(iii) The response from neighbouring spins then can be recovered by subtracting the particle-hole response (i) and the response from fluctuations (ii) from the experimental spectra (black lines). This difference is shown as green area in Fig. 6.14 and can be considered a good approximation to the two-magnon peak.

6.2.2 Putative fluctuations in A_{1g} symmetry

Viewed on a large scale the response in A_{1g} symmetry [Fig. 6.12(a)] is composed of the narrow phonon line at $\Omega^{(\mathrm{Se})} \approx 180\,\mathrm{cm}^{-1}$ superposed on a rather flat and temperature-independent continuum. Only in the range from $500\,\mathrm{cm}^{-1}$ to $1200\,\mathrm{cm}^{-1}$

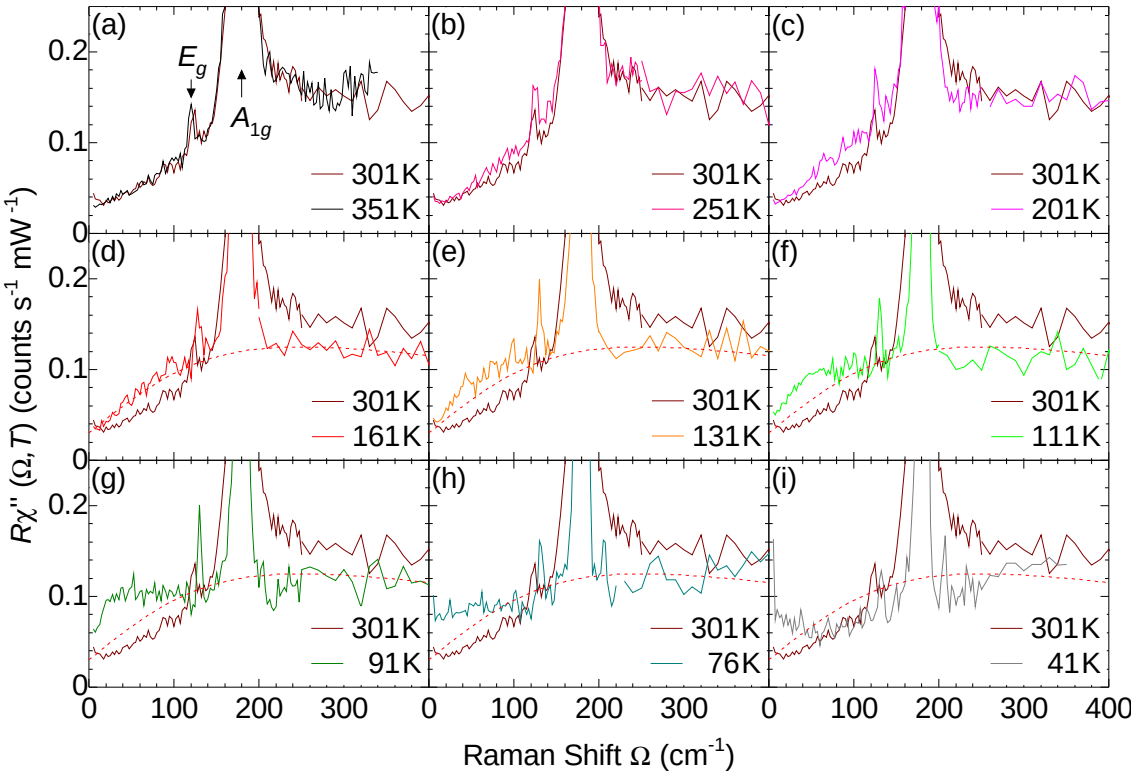

Figure 6.15: Low energy Raman spectra in A_{1g} symmetry. The increase in intensity towards $\Omega \to 0$ is due to elastic scattering. Sharp lines at 130 cm^{-1} and 180 cm^{-1} are phonons. Upon cooling the spectral weight at $\Omega > 180\,\mathrm{cm}^{-1}$ decreases and the Se phonon acquires a more symmetric line shape. The initial slope and the spectral weight at $\Omega < 130\,\mathrm{cm}^{-1}$ increase when approaching $T_s = 89.1\,\mathrm{K}$, but decrease below. The red dashed line is a description of the electron-hole continuum at $T = 160\,\mathrm{K}$.

a small peak arises below T_s. Focusing onto the low energy part ($\Omega < 250\,\mathrm{cm}^{-1}$), however, reveals additional features shown in Fig. 6.15. The steep increase of all spectra for $\Omega \to 0$ can be attributed to elastic scattering of the laser light due to surface layers. This effect increases below T_s (Fig. 4.10). At room temperature the spectrum consists of a smooth continuum which increases almost linearly at low energies and saturates above 250 cm^{-1}. Onto this continuum the E_g and A_{1g} phonons are superposed, which are not a subject of this section.

At low energies ($\Omega < 130\,\mathrm{cm}^{-1}$) the continuum shows an increase in spectral weight and of the initial slope when cooling towards T_s. One can model the continuum at 160 K with an analytic function (red dashed line in Fig. 6.15) similar to Fig. 6.14. This illustrates that the intensity of the continuum above 180 cm^{-1} changes little for $T \leq 160\,\mathrm{K}$ and suggests that the additional spectral weight found below 130 cm^{-1} is due to an additional scattering channel with a similar temperature

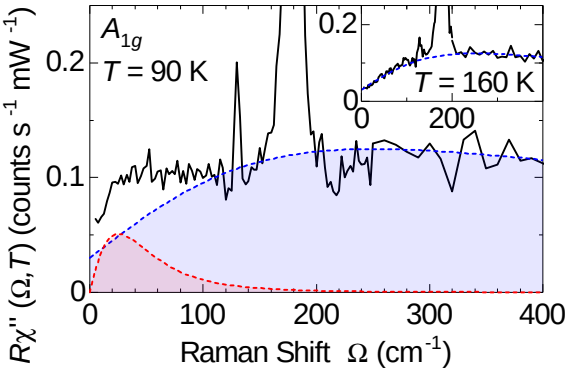

Figure 6.16: Decomposition of the A_{1g} Raman spectrum at $T = 90\,\mathrm{K}$. Black lines are experimental spectra, dashed blue lines depict an analytic approximation to the particle-hole-continuum at $T = 160\,\mathrm{K}$ (inset). The red dashed line models the low energy peak via AL-type diagrams.

dependence as the fluctuations in B_{1g} symmetry (Fig. 6.14) and in $Ba(Fe_{1-x}Co_x)_2As_2$ [31, 117, 118].

As shown in Fig. 6.16 for the $T = 90\,\mathrm{K}$ spectrum (excluding the phonon lines) a quantitative decomposition into two contributions is possible.

(i) The particle-hole continuum is approximated at $T = 160\,\mathrm{K}$ by the analytic function used previously for the B_{2g}/B_{1g} continuum (with different parameters), as shown in the inset.

(ii) The response from fluctuations is modelled via AL-type diagrams similar to B_{1g} symmetry. With the particle-hole continuum being virtually constant at $T \leq 160\,\mathrm{K}$, as can be seen from Fig. 6.15, the main temperature dependence at low energies is found in these fluctuations which exhibit a maximum in intensity at $T \approx T_\mathrm{s}$ before vanishing again upon further cooling.

6.2.3 Fluctuations and selection rules

The description via AL-type diagrams does not distinguish the type of fluctuations. With the peak from fluctuations persisting below T_s one can rule out critical fluctuations of the nematic phase, as those are expected to diverge and vanish at T_s. One can further narrow down the fluctuations to be considered by their wave vectors $\mathbf{q}$. These need to connect parts of the Fermi surface (FS) where the Raman vertex of the respective symmetry has the same sign, otherwise their contribution is cancelled out by the average over the FS [31]. For FeSe, fluctuations having zero momentum as well as $(\pi, 0)$, (π, π), and $(\pi, \pi/2)$ vectors are likely candidates. These cases are

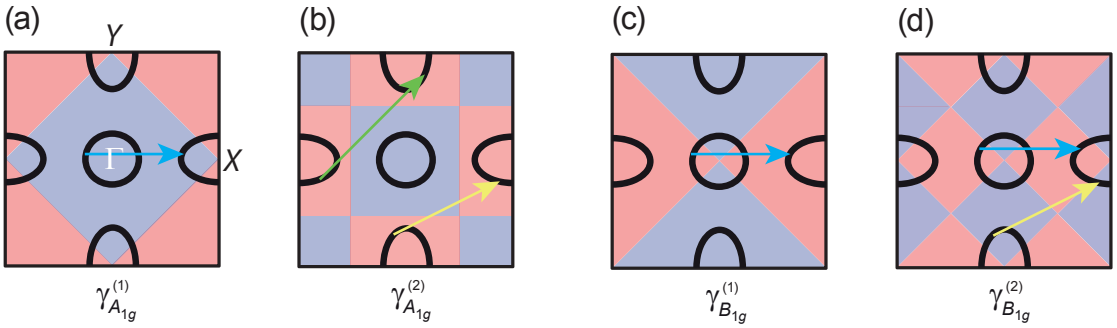

Figure 6.17: Raman vertices projected onto the 1-Fe Brillouin zone of the IBS [31]. (a) and (c) show first order, (b) and (d) show second order vertices, respectively. Blue and red areas denote positive and negative sign of the vertices. Black solid lines depict the simplified Fermi surface of the IBS with hole-like bands around the Γ-point and electron-like bands around the X and Y points. Blue, green, and yellow arrows point out $(\pi, 0)$, (π, π), and $(\pi, \pi/2)$ vectors, respectively.

depicted in Fig. 6.17 for the A_{1g} and B_{1g} vertices projected onto the 1-Fe Fermi surface of the IBS.

(i) Only charge, not spin fluctuations, can have zero momentum [31]. These $q = 0$ charge fluctuations can be projected in both orders of the A_{1g} scattering channel but not in B_{1g} symmetry. Therefore, if the fluctuations in A_{1g} symmetry (Fig. 6.16) are zero-momentum charge fluctuations they need to be different from those appearing in B_{1g} symmetry (Fig. 6.14).

(ii) Spin fluctuations with $(\pi, \pi/2)$ ordering vector (yellow arrow) can connect the electron-like bands around the X and Y points. They can be projected by the second order A_{1g} vertex [Fig. 6.17(b)] and possibly the second order B_{1g} vertex [Fig. 6.17(d)]. However, a recent neutron scattering study [236] found no appreciable intensity for $(\pi, \pi/2)$ at low energies.

(iii) Néel fluctuations (green arrow) can be considered for the peak appearing in A_{1g} symmetry via the second order vertex [Fig. 6.17(b)]. Neutron scattering experiments show [236] that the intensity found for (π, π) at 110 K vanishes upon cooling to 4 K. This is in qualitative agreement with the behaviour seen in the A_{1g} Raman spectra (Fig. 6.15). Then, if the fluctuations in the A_{1g} channel are of Néel type those seen in B_{1g} symmetry must be of different origin.

(iv) Stripe-like fluctuations with $(\pi, 0)$ ordering vector (blue arrow) can be projected by the first order A_{1g} vertex as well as in B_{1g} symmetry in both orders.

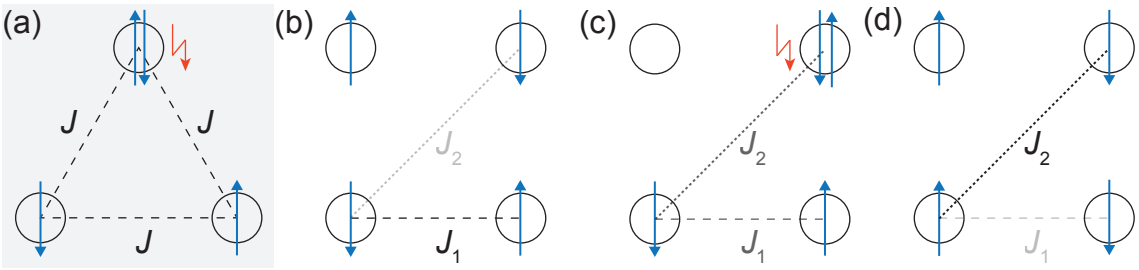

Figure 6.18: Frustration in the Heisenberg model. (a) Geometrical frustration on a triangular lattice with nearest neighbour interaction J. (b-d) J_1-J_2 model on a square lattice. If J_1 or J_2 prevails (b) Néel or (d) stripe order are established, respectively. (c) For $J_2 \approx J_1/\sqrt{2}$ the system is frustrated and long range order is suppressed.

$(\pi, 0)$ fluctuations were found in the Ba-122 compounds in B_{1g} but not A_{1g} symmetry [31, 118, 223]. In FeSe they may be related to the $(\pi, 0)$ frustrated ground state [153]. In neutron scattering experiments [236] the intensity at $(\pi, 0)$ is higher than for all other momenta at energies below 60 meV.

6.2.4 Frustration and the J_1-J_2-J_3-K model

The shape of the main peak in B_{1g} symmetry at $\Omega \approx 500\,\mathrm{cm}^{-1}$ [Fig. 6.12(c)] resembles the two-magnon peak in cuprates [Fig. 6.11(a)] and suggests that the response from localized spins may be a dominating effect in FeSe. However, the energies of this response differ by a factor of six to seven between FeSe and the cuprates whereas the nearest-neighbour exchange interaction $J_1 \sim 130\,\mathrm{meV}$ [46, 237] is similar. This motivated a study of FeSe in terms of frustrated magnetism of localized spins.

Frustration refers to the inability of a system to minimize its energy [238]. The simplest frustrated magnetic system is a triangular lattice with an interaction J between neighbouring spins [239] as shown in Fig. 6.18(a). While two of the spins can align antiferromagnetically the third spin can only conform to one of the two bonds. As no alignment of the spins is favoured no long range order can be established and the system becomes frustrated. This case is called geometrical frustration.

On a square lattice frustration can occur due to competition between the nearest-neighbour interaction J_1 and the next-nearest-neighbour interaction J_2 as shown in Fig. 6.18. For $J_1 \gg J_2$ [Fig. 6.18(b)] Néel order is established. This is the case for cuprates. Increasing J_2 from zero progressively destabilizes the Néel order as the energy required for flipping a spin is decreased. Maximum frustration is found for $J_2 \approx J_1/\sqrt{2}$ [Fig. 6.18(c)] when no alignment of the spins is favoured energetically

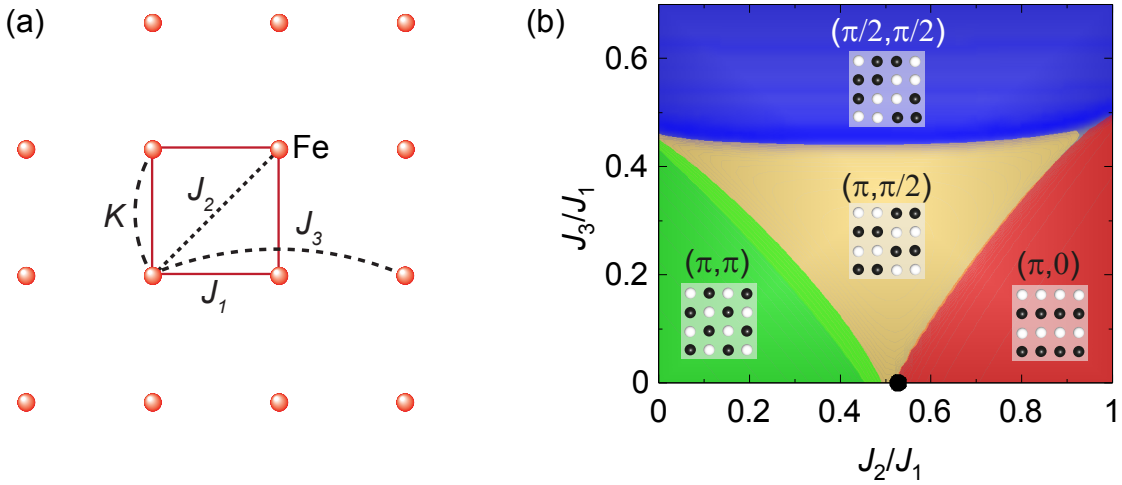

Figure 6.19: J_1-J_2-J_3-K-model on a square lattice. (a) J_i with $i = 1, 2, 3$ denote nearest, next-nearest, and next-next-nearest-neighbour interactions between the spins $\mathbf{S}_i$ with $S = 1$ localized on the iron atoms (red spheres). K is the coefficient of the biquadratic term. (b) J_2-J_3 phase diagram for $K = 0.1J_1$. Four competing phases exist. The corresponding spin alignments are shown in the insets whereby white and black spheres depict spin up and down, respectively. The black dot denotes the parameters $J_2 = 0.528J_1$ and $J_3 = 0$ used for the simulations. Adopted from Refs. [46, 153].

and hence long range order is suppressed. By further increasing J_2 the system is driven away from frustration again towards $(\pi, 0)$ stripe order [Fig. 6.18(d)].

This model can be extended to include further interactions such as J_3 between next-next-nearest-neighbours or biquadratic terms K (Dipole interaction) as shown in Fig. 6.19(a). Accordingly such a model is named J_1-J_2-J_3-K-model. Within this model for a spin-1 system simulations using exact diagonalization (ED) [240, 241] on a 4×4 cluster [Fig. 6.19(a)] were performed by H. Ruiz and co-workers and compared with the experimental results from this work [153]. Using ED a $J_2 - J_3$ phase diagram can be determined which is shown in Fig. 6.19(b) for $K = 0.1J_1$. The set of parameters giving the best agreement to the experiment ($J_2 = 0.528J_1$, $J_3 = 0$, and $K = 0.1J_1$) is denoted by the black dot. Four competing types of magnetic order are found. Qualitatively the phase diagram agrees with results from DFT calculations of the same model shown in Fig. 2.6 [46].

J_2 dependence

The main energy scale of the $J_1 - J_2 - J_3 - K$ model is given by the relative size J_2/J_1. Hence, the value for J_2 which best describes the experimental results needs

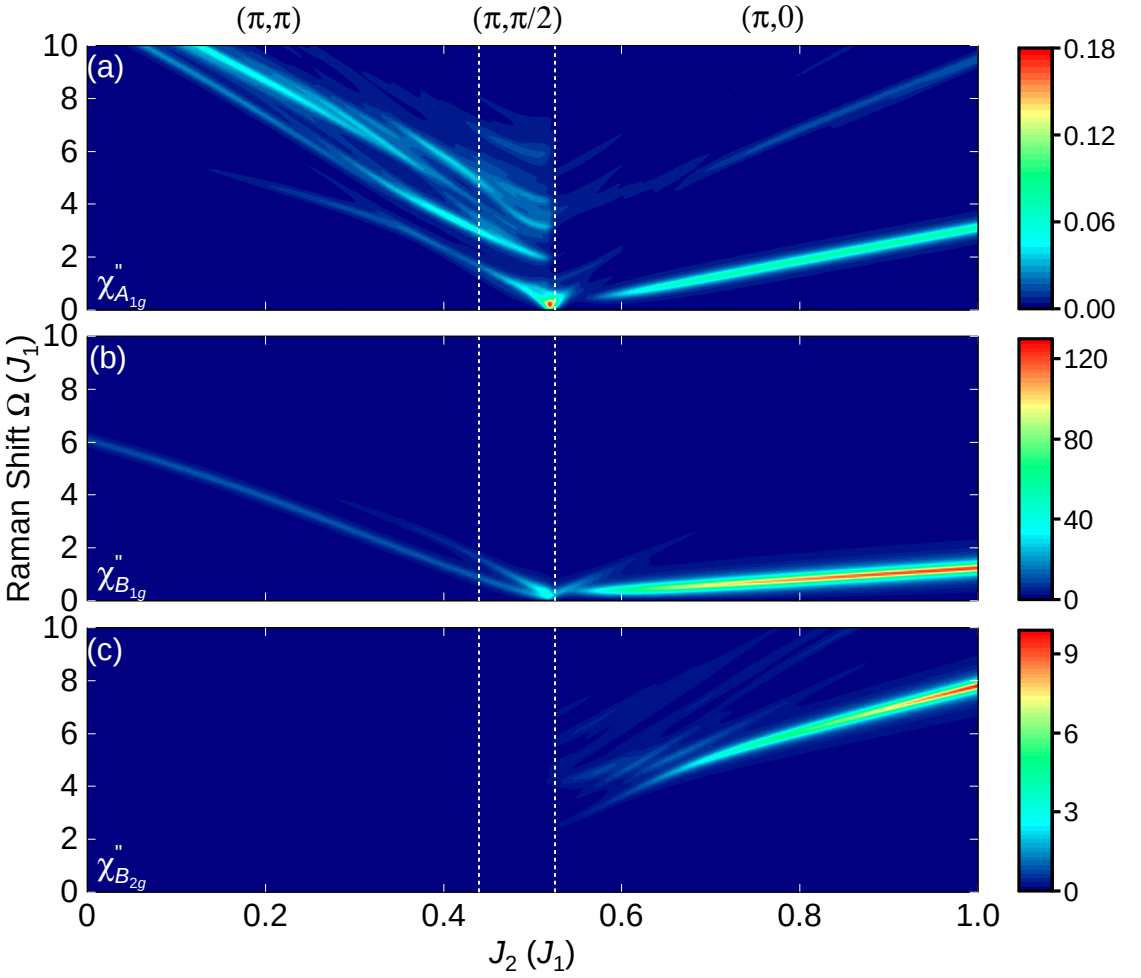

Figure 6.20: Simulated J_2 dependence of the Raman response χ''_μ for (a) $\mu = A_{1g}$, (b) $\mu = B_{1g}$, and (c) $\mu = B_{2g}$ symmetry as a function of the Raman shift Ω in units of J_1. The magnitude of χ''_μ is given by the respective colour scale. Vertical white dashed lines denote the boundaries between (π, π), $(\pi, \pi/2)$, and $(\pi, 0)$ ordered phases as shown on top. Courtesy of H. Ruiz.

to be found. To this end the Raman response χ''_μ for the three relevant symmetries $\mu = A_{1g}$, B_{1g}, and B_{2g} was calculated as a function of J_2 and the Raman shift Ω at $T = 0$ as shown in Fig. 6.20. This simulation can be compared to the experimental results at low temperatures ($T = 40\,\mathrm{K}$) shown in Fig. 6.12. A non-zero response in B_{2g} symmetry is only found in the $(\pi, 0)$ phase, i.e. $J_2 \gtrsim 0.525$. In this phase the experimentally observed weaker peak in A_{1g} symmetry and much stronger peak in B_{1g} symmetry are also present in the simulations. Their energies increase with J_2, therefore a value $J_2 \approx 0.525$ close to the phase boundary between the $(\pi, 0)$ and the $(\pi, \pi/2)$ phase is expected to give the best agreement between theory and experiment.

J_3 dependence

The degree of frustration is given by the proximity of the chosen point in the phase diagram to a phase boundary. As shown above the relevant phase is the $(\pi, 0)$ state having a boundary to the $(\pi, \pi/2)$ phase. To test the influence of J_3 several points close to the $(\pi, 0)$-$(\pi, \pi/2)$ border were sampled as shown in Fig. 6.21(f). For every point in the phase diagram the temperature dependence of the Raman response in B_{1g} symmetry, $\chi''_{B_{1g}}$, was simulated. Increasing J_3 to $0.01J_1$ slightly enhances the softening of the peak around $T \sim 0.1J_1$ as shown in Fig. 6.21(b), which still reproduces the experimental results within the margin of error. Any further increase to $J_3 \geq 0.05$ [Fig. 6.21(c-e)] quickly destroys the agreement between simulations and experiment. This B_{1g} response then exhibits a considerably broadened peak without noticeable temperature dependence. For $J_3 = 0.05J_1$ a second weaker peak at higher energies appears which is not observed in the experiment. Therefore $J_3 \leq 0.01J_1$ is required to reproduce the experimentally observed temperature dependence of the B_{1g} response (Fig. 6.13). This indicates that the proximity of the $(\pi, 0)$ and (π, π) phases, but not of $(\pi, 0)$ and $(\pi, \pi/2)$, is at the origin of the frustration. Results from neutron scattering also show that the response for $(\pi, \pi/2)$ is small compared to (π, π) and $(\pi, 0)$ [236].

6.2.5 Temperature dependence of the response from localized spins

The Raman spectra simulated within the presented model can be directly compared to the experimental results. Fig. 6.22 shows these spectra for three temperatures $40\,\mathrm{K} < T_\mathrm{s}$, $91\,\mathrm{K} \gtrsim T_\mathrm{s}$, and $301\,\mathrm{K} \gg T_\mathrm{s}$. Two additional temperatures are shown for the B_{1g} response. The experimental spectra are duplicated from Figs. 6.12 and 6.13. Using $J_1 = 123\,\mathrm{meV}$ [2][46] a semi-quantitative comparison of experiment and simulations is possible.

The temperature dependence of the response from localized spins in B_{1g} symmetry is well captured by the simulations [Fig. 6.22(b)]. This includes the softening and the increase in peak height upon cooling from room temperature to T_s as well as the hardening and slight growth below. At intermediate temperatures a weak shoulder forms on the low energy side of the magnon peak. The low-energy excitation which was identified as fluctuations (Sec. 6.2.3) is not captured by the simulations on a

[2] 123 meV correspond to a Raman shift of approximately $990\,\mathrm{cm}^{-1}$ or a temperature of approximately 1500 K, respectively.

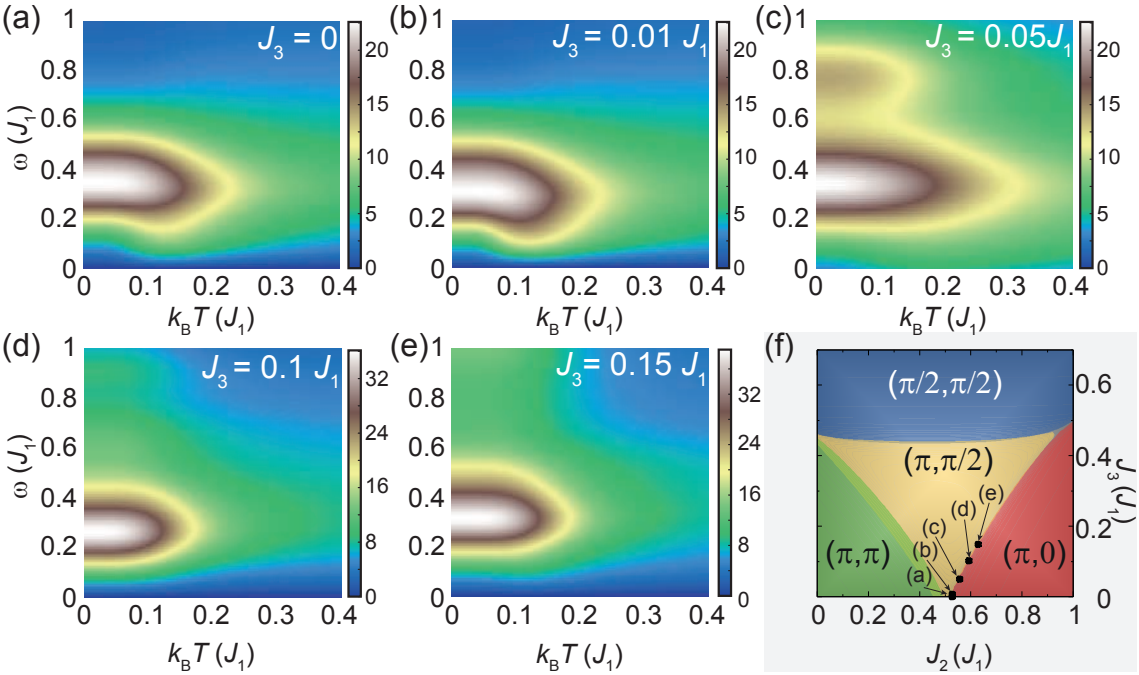

Figure 6.21: Simulated J_3 dependence of the Raman response in B_{1g} symmetry. (a-e) $\chi''_{B_{1g}}$ as a function of temperature T and Raman shift Ω in units of J_1. The magnitude of $\chi''_{B_{1g}}$ is given by the respective colour scale. (f) $J_2 - J_3$ phase diagram. The labelled black dots mark the positions where the response shown in panels (a-e) was sampled. Courtesy of H. Ruiz.

4×4 cluster, which is small compared to the correlation length.

In A_{1g} symmetry [Fig. 6.22(c-d)] the simulations reproduce the small peak (blue shaded area) which arises at low temperatures at an energy slightly above the maximum of the B_{1g} peak. The low energy peak from putative fluctuations (Sec. 6.2.2) is not captured by the simulations due to the cluster size.

For B_{2g} symmetry [Fig. 6.22(e-f)] the gain in spectral weight at high energies (blue shaded area) and the opening of a (pseudo-)gap at intermediate energies (red shaded area) are also found in the simulated spectra.

For all symmetries the simulations predict a continuous evolution of the spectral weight. In the experiment the gap in B_{2g} symmetry is already fully developed at T_s whereas the additional peaks in A_{1g} and B_{2g} symmetry only form below T_s. This suggests that the magnetism couples to the structural transition which is not included in the simulations on a square lattice [Fig. 6.19(a)].

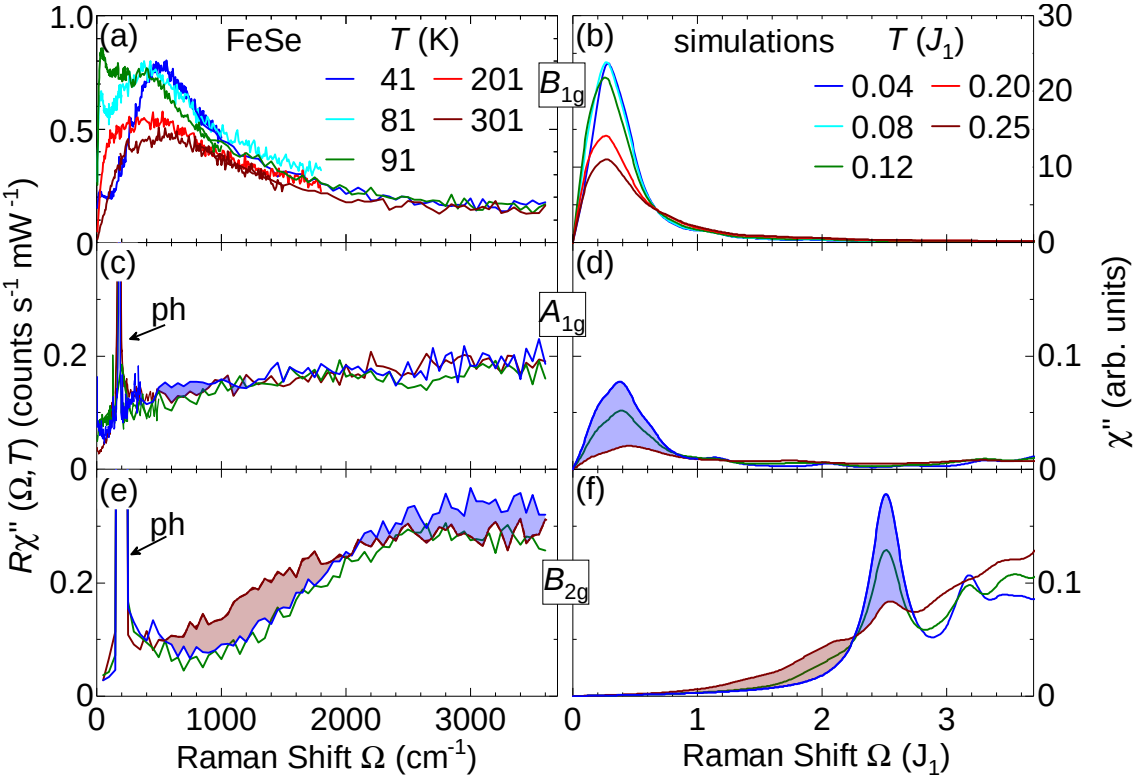

Figure 6.22: Temperature dependence of (a,c,e) experimental and (b,d,f) simulated Raman spectra for (a,b) B_{1g}, (c,d) A_{1g}, and (e,f) B_{2g} symmetry at temperatures as given in the legend. Gain and loss of spectral weight upon cooling in A_{1g} and B_{2g} symmetry are indicated as blue and red shaded areas, respectively. Sharp peaks marked by 'ph' are phonons. Simulations adopted from Ref. [153].

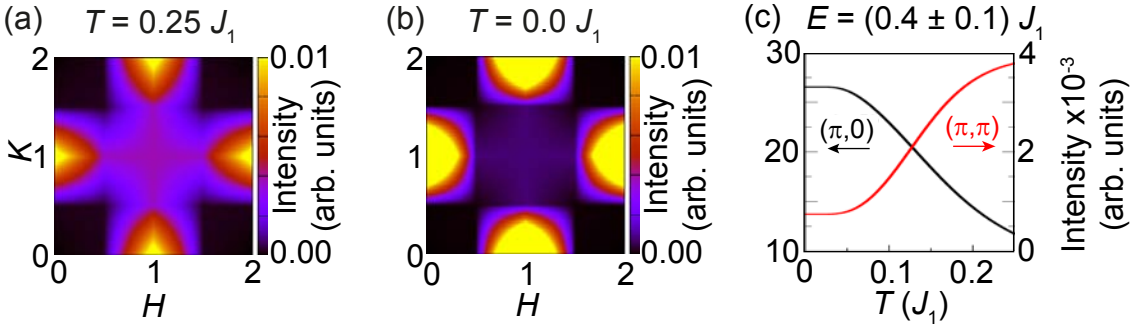

Figure 6.23: Simulations of the dynamical structure factor of localized spin excitations for an energy window of $(0.4 \pm 0.1)J_1$. (a,b) Cuts through the first BZ at $T = 0.25J_1$ and $0J_1$, respectively. The intensity at (π, π) vanishes upon cooling, whereas at $(\pi, 0)$ the intensity increases. (c) Integrated (π, π) and $(\pi, 0)$ intensities as a function of temperature. Adapted from Ref. [153].

6.2.6 Structure factor

To test the theoretical model beyond Raman spectroscopy the dynamical spin structure factor was simulated for an energy window of $(0.4 \pm 0.1)J_1$ and can be compared to results from neutron scattering [236]. The simulated structure factor is shown in Fig. 6.23(a) and (b) for two characteristic temperatures. At high temperatures the intensity is highest around $(\pi, 0)$. Along the line $(\pi, 0)$-(π, π) the intensity is smaller and rather uniform. Upon cooling spectral weight is shifted from around (π, π) to $(\pi, 0)$. In Fig. 6.23 the evolution of the spectral weight at $(\pi, 0)$ and (π, π) as a function of temperature is shown. The progression is similar to the experimental results [236]. In the neutron scattering experiment, the most pronounced change of the spectral weight occurs at T_s. The simulations do not include the structural change and provide a smooth progression of the spectral weight. In the simulations the slope of this change is maximal at the temperature where the simulated B_{1g} response [Fig. 6.22(b)] shows the most pronounced shoulder and where the intensity starts to decrease upon heating.

Chapter 7

Summary

This thesis describes the interrelation of magnetism, lattice dynamics, nematic fluctuations and order, and superconductivity in iron-based systems. The main experimental technique was inelastic scattering of light (Raman effect). In addition to the Raman measurements several instrumental developments including the diamond anvil pressure technique and susceptibility measurements in the pressure cell were put forward and are described in the appendix.

Three compounds of iron based systems were studied. The experimental data were complemented by theoretical calculations obtained in collaborations with groups in Belgrade, Frankfurt, and Stanford.

In tetragonal FeS, the phonon modes were studied as a function of temperature and polarization, and were used predominantly to search for phase transitions. The Raman-active sulphur and iron phonons having A_{1g} and B_{1g} symmetry, respectively, were identified. In addition to the Raman-active modes two excitations with A_{1g} and mixed $A_{1g} + B_{1g}$ selection rules were observed. The A_{1g} mode at $265\,\mathrm{cm}^{-1}$ discovered in a gap of the phonon density of states could be traced back to second order scattering. The peak with mixed symmetry at $301\,\mathrm{cm}^{-1}$ was attributed to first-order defect-induced scattering. The temperature dependences of the widths and the energies of the phonons were analysed in terms of phonon-phonon interaction and Grüneisen theory, respectively. The Grüneisen parameters are in the usual range between 2 and 3. The phonon-phonon coupling governing the width of the A_{1g} sulphur mode is six times stronger than those of the other modes. This observation along with the appearance of second order scattering suggests an enhanced electron-phonon coupling which may even be sufficient to support a transition temperature to superconductivity T_c in the range of 5 K. Below 20 K the energies of all phonons increase in agreement with the unit cell volume. This anomaly may have its origin in

the onset of short-ranged magnetic order at 20 K as proposed by μSR measurements.

The phonons in $BaFe_2As_2$ were studied on a de-twinned crystal to further pin down the origin of the magneto-structural transition at T_{SDW}. Both E_g phonons split into two non-degenerate modes below T_{SDW}. The de-twinning allowed the first unambiguous assignment of the B_{2g} and B_{3g} phonons in the orthorhombic phase. Lattice-dynamical calculations using density functional theory showed that the large splitting of the low-energy $E_g^{(1)}$ phonon is linked to the $(\pi, 0)$ magnetic order below T_{SDW}. The study of the A_g As mode as a function of the incident photon energy revealed a strongly anisotropic resonance effect which could be traced back to the band structure reconstruction induced by $(\pi, 0)$ magnetic order.

The purpose of the studies of FeSe, which lacks long-range magnetic order, was to scrutinize the role of magnetism for the structural transition at 90 K. To this end spectra were measured in an energy range of up to 1 eV as a function of polarization and temperature. The full symmetry analysis goes beyond previous studies and provides evidence for the magnetic origin of most of the intensity in B_{1g} symmetry and part of the spectral weight in A_{1g} and B_{2g} symmetry. The temperature dependence of the spectra at medium and high energies exhibits similarities with the cuprates rather than $BaFe_2As_2$. Simulations using exact diagonalization of a spin-only model agree well with results from Raman and neutron scattering, and show that FeSe is best described within a spin-1 system of mainly local moments where long-range order is quenched by frustration. The analysis of the low energy response provides evidence of fluctuations in B_{1g} and presumably in A_{1g} symmetry. The exact type of these fluctuations could not be pinned down, but $(\pi, 0)$ spin fluctuations are a likely candidate for the response seen in both symmetries.

The results in $BaFe_2As_2$ and FeSe suggest that local spins can be of central importance for modelling the properties even of metallic systems. Both phonon anomalies in $BaFe_2As_2$ can be well explained using local density approximation and localized spins when an orbital-selective renormalization of the band structure is applied. The results in FeSe demonstrate that Raman spectroscopy can efficiently distinguish between itinerant and local magnetism. Thus the experimental results presented in this thesis suggest that the iron based systems may be best described as Hund's metals, where Hund's rule coupling is responsible for orbital-dependent localization of spins.

Appendix A

High pressure experiment

In the IBS high pressure can serve as a tuning parameter. As opposed to atomic substitution, pressure does not change the sample quality and is reversible. Already quite early in the history of condensed matter physics the application of hydrostatic high pressure to a sample was found to be a gateway to control its properties in a well defined manner. Experimentally its advantages lie in the fact that often clean stoichiometric samples can be used whereas the substitution of atoms always induces deviations from the lattice periodicity and the growth of homogeneously doped samples is challenging. Additionally, the applied pressure can be controlled continuously and in fine steps. From the theoretical perspective the application of pressure is equivalent to modifying the lattice parameters and thus can be modelled straightforwardly. The diamond anvil cell (DAC) stands out as it creates the highest pressures achieved so far while providing access for a wide range of measurement methods [242].

In the IBS the whole phase diagram can be accessed. In the 122 systems the application of hydrostatic pressure in the range up to 10 GPa produces a phase diagram similar to atomic substitution [18, 20, 243, 244].

For the 11 systems pressure is even more valuable as the phase diagram of FeSe differs greatly when changing the control parameter from isovalent substitution of sulphur (Fig. 2.5), i.e. chemical pressure, to external high pressure. Notably the application of pressure leads to a triplication of the critical temperature [40] and gives rise to a magnetically ordered phase [41, 245], both of which are not seen in the sulphur substituted material.

To explore this advantage high pressure Raman experiments on $BaFe_2As_2$ were performed in collaboration with A. Walter [188] and experiments on pristine FeSe were prepared. This work required further improvement of the setup, in particular

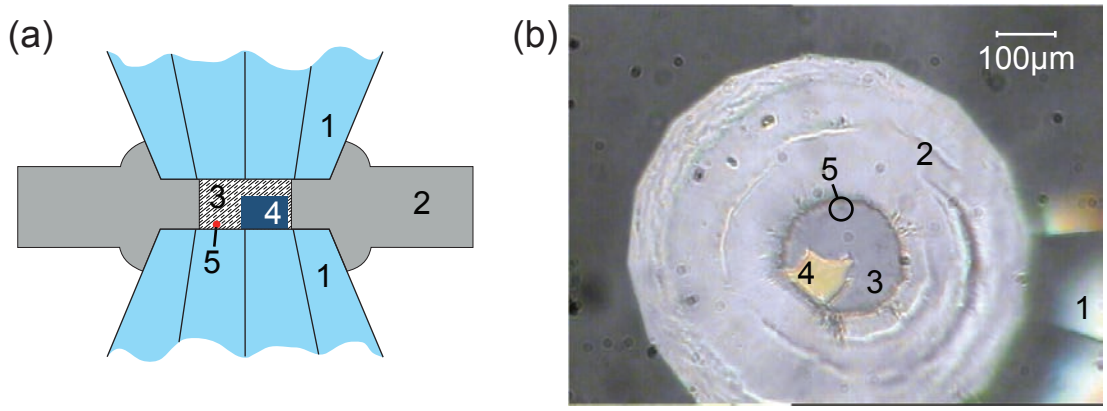

Figure A.1: Principle of the DAC. (a) Schematic section of the DAC (side view). (b) Photograph taken through the lower diamond anvil. (1) diamond anvils, (2) stainless steel gasket, (3) sample volume filled with He, (4) sample, (5) ruby sphere. From Ref. [247]

the combination of high pressure equipment and susceptibility measurement to track the variation of the phase transition lines. The experiment on FeSe could not be finished due to a loss of sensitivity of the CCD detector [246] which could not be repaired in time.

A.1 Principle of the DAC

The basic working principle of a diamond anvil cell is shown in the schematic drawing in Fig. A.1(a). Two diamond anvils (1) are aligned so that the opposing surfaces are parallel. The gasket (2) between the two anvils contains a hole that forms the sample volume (3) which is filled with the pressure transmission medium. This medium is compressed by the anvils and exerts (quasi-)hydrostatic pressure on the sample (4). To determine this pressure a ruby sphere (5) is placed inside the sample volume. The pressure dependent shift of the ruby fluorescence line serves as pressure gauge [248].

The working setup is shown in the photograph in Fig. A.1(b), which also illustrates a main advantage of the DAC, namely the easy optical access to the sample. Helium is an ideal candidate for the pressure transmission medium as it remains liquid over a large range of temperatures and pressures, and its solid form is still sufficiently soft to maintain almost hydrostatic pressure [242, 249]. The pressure cell used during this work was built by L. Tassini [250] and was improved over time. For a more technical description of the recent DAC setup the reader is referred to the PhD thesis of H.-M. Eiter [247]. A detailed presentation of the optical setup

for high pressure experiments and its alignment is given in the Master's thesis of M. Mitschek [251].

A.2 Magnetic susceptibility in a DAC

The latest augmentation of the high pressure setup was the addition of the in situ susceptibility measurement implemented by R. Roßner [187]. The basic principle is identical to the setup described in Sec. 4.2. The following changes need to be addressed:

(i) The small volume of the sample (typically around $100\,\mu m \times 100\,\mu m \times 30\,\mu m$) and the low filling factor (details see Ref. [187]) entail a very low voltage of only a few nanovolts to be measured.

(ii) The noise and background signals must be minimized. Both problems were solved during the Master's thesis of A. Walter [188].

Even if the the frequencies of the excitation and detection signals differ by a factor of three the presence of the first harmonic induces an overload of the lock-in amplifier at the required sensitivity. This can be overcome by setting up a gradiometer of two identical pairs of coils as shown in Fig. A.3. Wiring the primary coils in the same and the pick-up coils in opposite direction compensates the signal. In an ideal system the compensation leaves only the difference in the signal generated by the magnetization of the sample placed in one of the two systems. In a real setup one can only achieve a significant suppression of the signals at both the first and the third harmonic but the spurious signal is still by far too high at nanovolt sensitivity. In the setup built by R. Roßner [187] the principal compensation is accomplished by having two concentrically wound pairs of coils as shown in Fig. A.2(a). Both pairs of coils are glued on a Kapton foil. The first pair of coils (L3 and L4) is centred around one diamond of the cell and picks up the signal from the sample. The second pair (L2 and L5) is placed on the copper beryllium support. The compensation achieved by this setup still required additional filtering to perform measurements at the third harmonic. To further reduce the background signal modifications as shown in Fig. A.2(b) were made during the master's thesis of A. Walter [188]. The magnetic environment of the first pair of coils (L3 and L4) is given by the (insulating) diamond and the stainless steel gasket, whereas the second pair of coils (L2 and L5) is placed on the CuBe disk. To provide a more symmetric magnetic environment a hole was drilled into the CuBe disk, as air and helium are closer in conductivity to

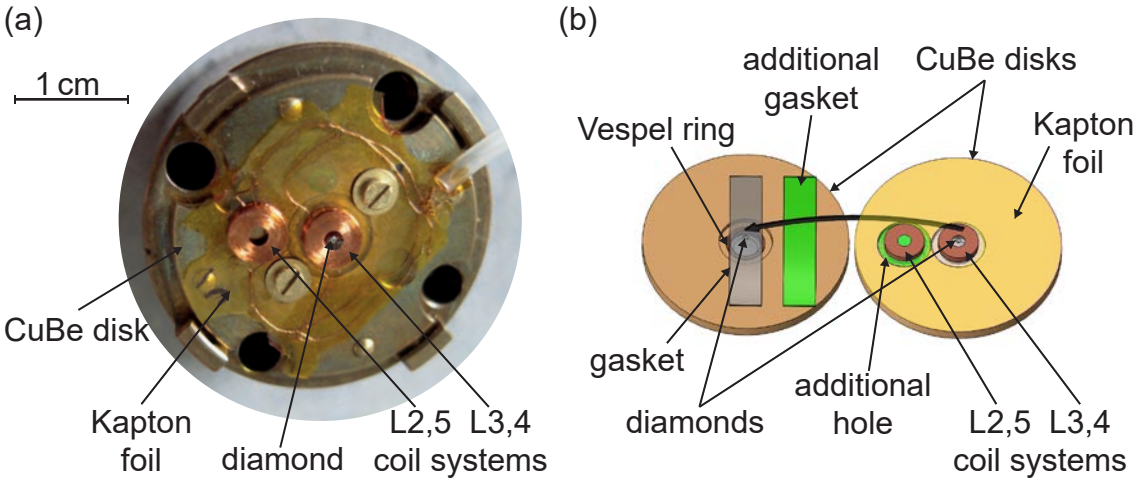

Figure A.2: Coil system for the susceptibility measurement inside the DAC. (a) Photograph of the setup built by R. Roßner showing the coil system mounted in the DAC. Taken from Ref. [187]. (b) Schematic of the modified coil system realized during the master's thesis of A. Walter [188]. On the left the lower part of the DAC with one of the diamonds is shown. On the upper part of the DAC (right side) the coil system (glued on Kapton foil) is centred around the second diamond. An additional gasket and hole (green) provide a more symmetric magnetic environment. The diamonds are centred by Vespel rings. The broad black arrow depicts the assembly of the cell which puts the two halves on top of each other. Adopted from Ref. [188].

the diamond than CuBe is. Additionally, a second stainless steel gasket was placed below L2 and L5. The mounting of the coil pairs on Kapton foil remains an issue as the foil easily bends and tends to deform when the temperature is changed. Sapphire plates, if not found to be too brittle, could be an alternative to the Kapton foil to be considered in future modifications.

Complementary to the mechanical changes compensation can also be achieved by augmenting the electric setup. To this end the magnetic fields generated by the two primary coils are adjusted relative to each other to cancel out the remaining asymmetries of L2,5 and L3,4. This can be achieved using the electric setup shown in Fig. A.3. The coils L2-5 are identical to the previous setup but are reconnected as follows. The primary coils L2,3 are wired in series externally. R1-4 are multi-turn potentiometers. The potentiometer R4 replaces the previously used fixed series resistor $R4^* \approx 134\,\Omega$ and connects the common connector of the primary coils to the sine wave generator. The current through L3 is set by R3. Similarly, the current through L2 is set using R1 for coarse and R2 for fine grained control. Here, R2 is used as a fine adjustment to the parallel $1\,\Omega$ resistor. The variable coil L1 serves as phase shifter for the current through L2. L1 is custom-made and is wound on a

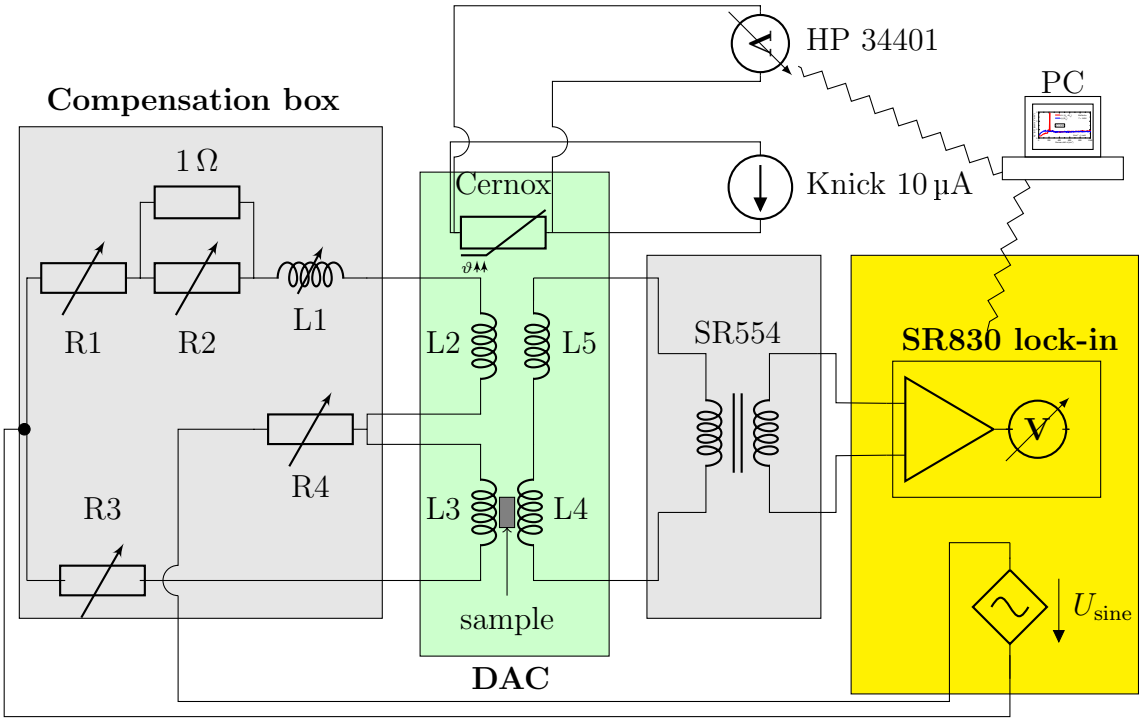

Figure A.3: Equivalent circuit of the susceptibility setup. Parts mounted inside the DAC are shown on a green background. Amplitudes and relative phase of the magnetic fields generated by L2 and L3 are controlled by regulating the input from the sine voltage source (part of the SR830 lock-in) via the potentiometers R1-4 and the variable coil L1 inside the compensation box (grey shaded area). L4 and L5 are wired in opposite direction for compensation. The net voltage is stepped up by the SR554 transformer and fed into the lock-in amplifier (yellow area). The temperature of the DAC is monitored by four-probe readout of a Cernox resistor using a Knick current source and a HP 34401 multimeter.

support containing a ferrite rod which can be moved using a micrometer screw, thus changing the inductance of the coil.

This setup for external compensation is installed into a copper box as shown in Fig. A.4. The temperature of this box is stabilized by an Oxford ITC503 temperature controller. The copper box, together with the SR554 transformer preamplifier, is integrated into a steel case using PVC spacers to reduce the thermal coupling to the exterior. Without this additional temperature stabilization the compensation drifts from less than 10 nV to several microvolts when the room temperature changes by as little as 0.2 K. Operation of the control elements (R1-4, L1) from outside is facilitated by additional PVC axes.

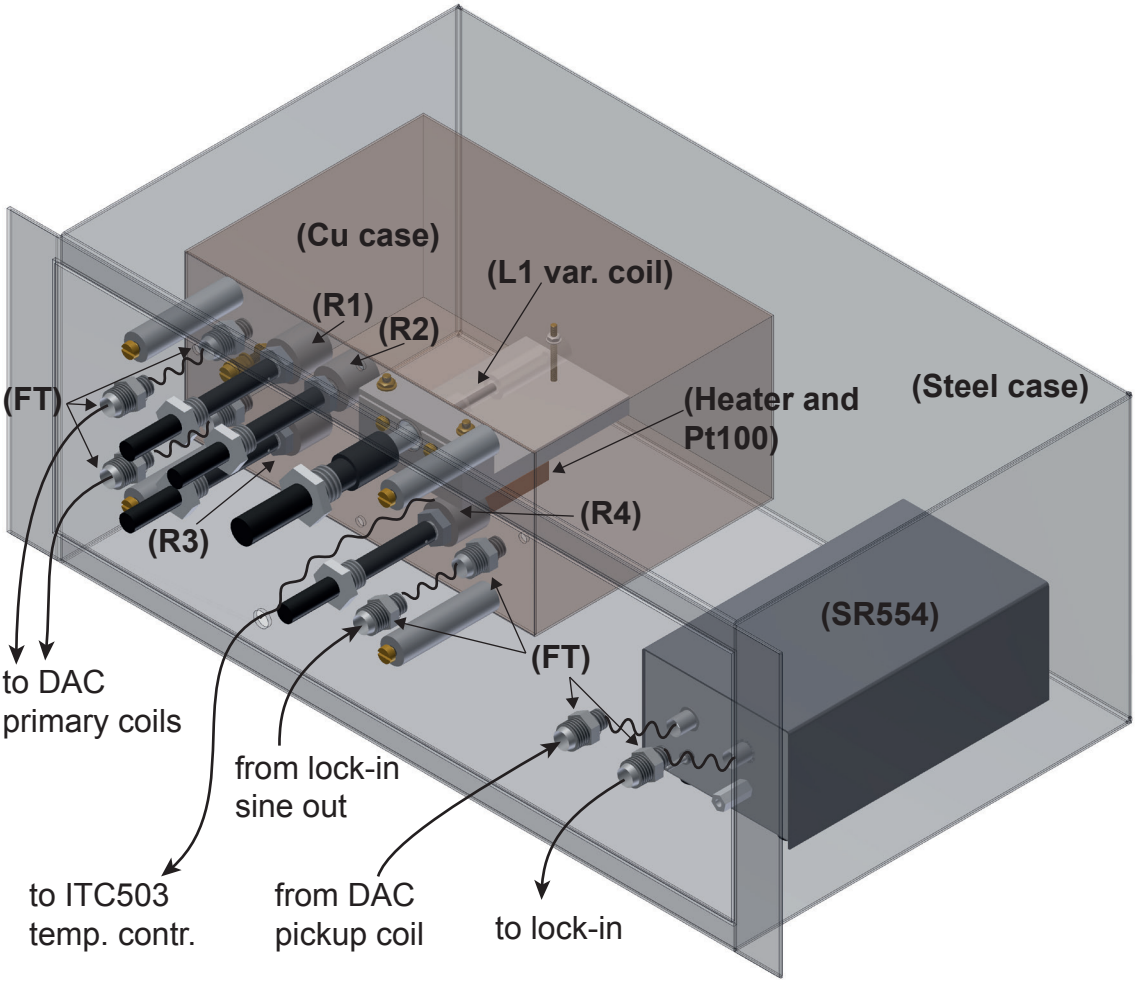

Figure A.4: Picture of the setup for the external compensation of the susceptibility measurement. Amplitude and relative phase of the magnetic field created by the primary coils are controlled by the potentiometers (R1-4) and the variable coil (L1), which are placed inside a copper case. The temperature of this case is controlled externally from an ITC503 temperature controller using the Pt100 sensor and heater. The copper box and the SR554 preamp-transformer are both placed inside a steel case to maintain a stable temperature. Access to the control elements is provided by PVC rods (black rods). Cables are routed through feedthroughs (FT). The internal wiring is mostly omitted for clarity and is shown in the schematics in Fig. A.3.

A.3 Preparatory measurements on FeSe

High pressure experiments on FeSe can open new vistas into the magnetic order which arises [41, 245] and its interplay to superconductivity [81]. Unlike in the 122 pnictides, where applied hydrostatic pressure and chemical pressure by isovalent substitution yield similar results [18, 20, 243, 244], the phase diagrams are fundamentally different for FeSe (Fig. 2.5 and Ref. [40, 41, 81, 245]). Early experiments showed a triplication of the critical temperature T_c [40], which is not seen when substituting S for Se. Additionally, FeSe develops long range magnetic order under pressure [41] whereas magnetism is suppressed by pressure in the 122 pnictides [20]. In the light of the findings presented in Sec. 6.2, showing that long range magnetic order in FeSe is found to be suppressed by frustration while putatively effects from both localized and itinerant electrons coexist, external pressure is expected to provide a promising access to study the interplay of these phenomena. One may speculate that the magnetic order found in FeSe at high pressure arises when the system is driven away from frustration. In the framework of orbital-selective Mottness [57, 58] changes to the structure between different types of IBS may be the parameter that distinguishes between itinerant and localized magnetism. A recent Raman study on FeSe found a suppression of the low energy peak from fluctuations by pressure [252], which may then indicate that the compression of the lattice tunes the system in favour of stronger localization. The main question to be answered is whether the long range order found under pressure arises from localized or itinerant electrons. As shown in the previous sections, Raman spectroscopy can distinguish between these different types of order.

Here susceptibility and Raman measurements are shown which were performed on a FeSe sample from batch TWOX1555 in the open DAC. A defect of the CCD detector [246] hampered Raman measurements of the low intensity excitations. Additionally the measurements performed highlighted issues regarding the sample quality. The preliminary work shows that the intended study outlined above is feasible and promising once these technical issues are taken care of.

A.3.1 Magnetic susceptibility of FeSe in the DAC

The non-linear susceptibility of the FeSe sample was determined and is shown in Fig. A.5. The two measurements were recorded upon cooling (blue line) and heating (red line). In both cases one strong and several smaller peaks and shoulders are found in U_3. The curves indicate that T_c is not entirely uniform. The large discrepancy in

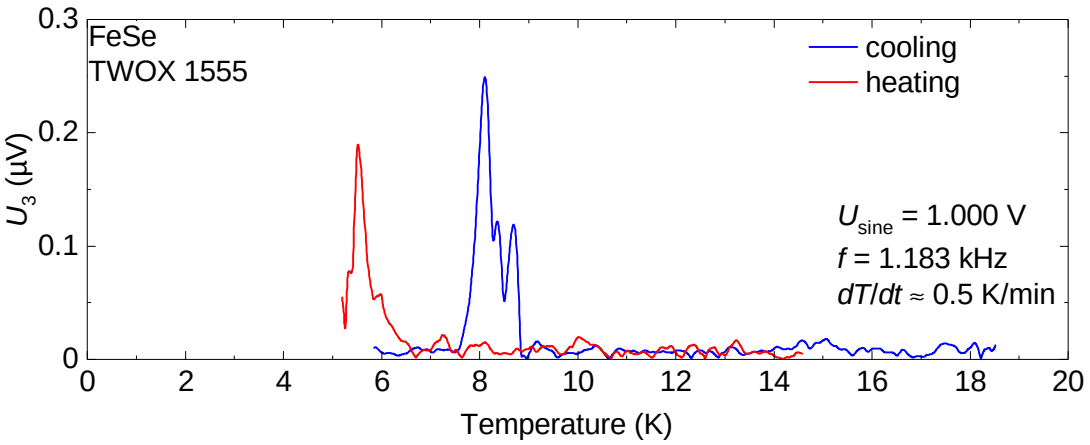

Figure A.5: Non-linear magnetic susceptibility of the FeSe sample in the open DAC upon heating (red) and cooling (blue).

temperature between the main peaks in the two measurements is most likely due to thermal hysteresis caused by the large mass of the pressure cell. The temperature shown is measured using a Cernox resistor mounted at the top of the pressure cell [247] at roughly 3 cm distance from the sample.

A.3.2 Raman spectra of FeSe in the DAC

Raman spectra of the FeSe sample were taken at three temperatures as shown in Fig. A.6. Each spectrum shown is an average of at least ten exposures after spikes were removed. A single exposure of the same duration would result in spectra filled with spikes. The large amount of spikes encountered in this set-up may also be related to the defect of the CCD. The spectra were taken with a wavelength of the incident laser $\lambda_i = 532\,\mathrm{nm}$ and are normalized to the absorbed power and the Bose factor. To cover the energy range shown two spectra need to be measured with different positions of the spectrometer. Between these settings, as can be seen in the range from $370\,\mathrm{cm}^{-1}$ to $470\,\mathrm{cm}^{-1}$, for some measurements the intensity exhibits jumps which are of roughly the same magnitude for all three occurrences shown and are also likely an artefact due to technical issues.

The sample was aligned along the crystal edges. The appearance of the B_{1g} phonon at $215\,\mathrm{cm}^{-1}$ identifies the orientation as $(x, y)||(a, b)$. The second mode at $180\,\mathrm{cm}^{-1}$ is the Se phonon in A_{1g} symmetry. Upon cooling both phonon lines harden and sharpen as expected. The background shows a continuous increase at 295 K but its initial slope decreases for low temperatures, possibly due to an additional amount of elastically scattered light. As can be seen by comparing the two sets of

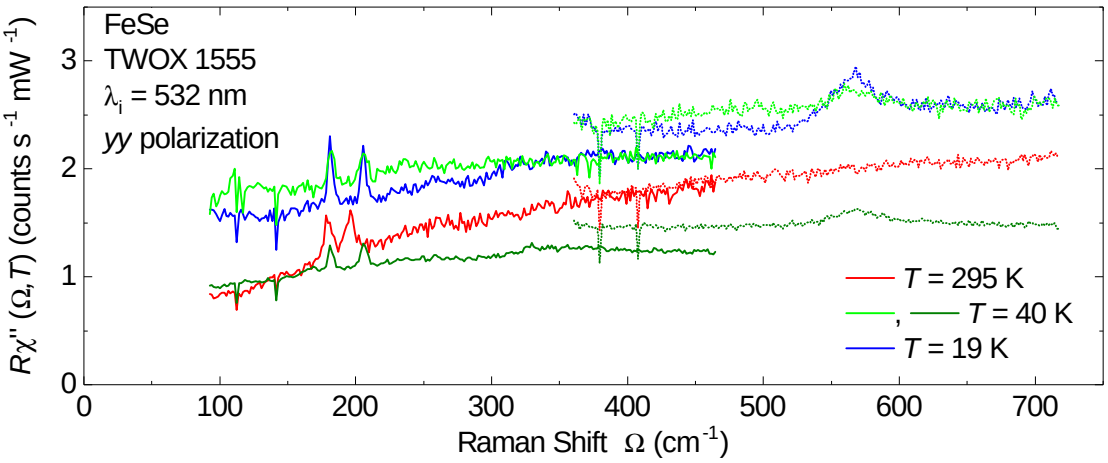

Figure A.6: Raman spectra of FeSe in the open DAC at temperatures as given in the legend. The spectra shown for each temperature are averages of multiple exposures with spikes removed. To span the energy range the spectrometer was set to two different positions. Between those settings the overall intensity exhibits a jump for some measurements as visible in the range from $370\,\mathrm{cm}^{-1}$ to $470\,\mathrm{cm}^{-1}$. The sharp peaks at $180\,\mathrm{cm}^{-1}$ and $215\,\mathrm{cm}^{-1}$ are the A_{1g} and B_{1g} phonon, respectively. At low temperatures a broad peak centred around $570\,\mathrm{cm}^{-1}$ arises.

measurements at $T = 40\,\mathrm{K}$ the overall intensity of the spectra is not reproduced. At low temperatures an additional broad peak around $570\,\mathrm{cm}^{-1}$ arises. Based on the selection rules, and because its intensity is comparable to the phonon lines, this peak cannot be the two-magnon excitation discussed in Sec. 6.2. Most likely it stems from issues of the sample quality.

A.4 Symmetry crossover in $BaFe_2As_2$

The high temperature tetragonal phase of $BaFe_2As_2$ was studied by Raman spectroscopy at pressures up to 10 GPa in collaboration with A. Walter [188]. To this end Raman spectra were measured in RL and RR polarizations as shown in Fig A.7, projecting $B_{1g} + B_{2g}$ and $A_{1g} + A_{2g}$ symmetries, respectively. At zero pressure (blue lines) both spectra have a flat background in the measured energy range. In RL polarizations the B_{1g} Fe phonon (see Fig. 2.3) appears at $\Omega \approx 215\,\mathrm{cm}^{-1}$. When the pressure is increased the background for both polarizations increases strongly. The Fe phonon hardens and its spectral weight decreases, making it almost indistinguishable for the highest pressures. In RR polarizations the A_{1g} phonon expected at $180\,\mathrm{cm}^{-1}$ for 0 GPa is not resolved. Starting at $p \approx 5.6\,\mathrm{GPa}$ a peak appears and hardens.

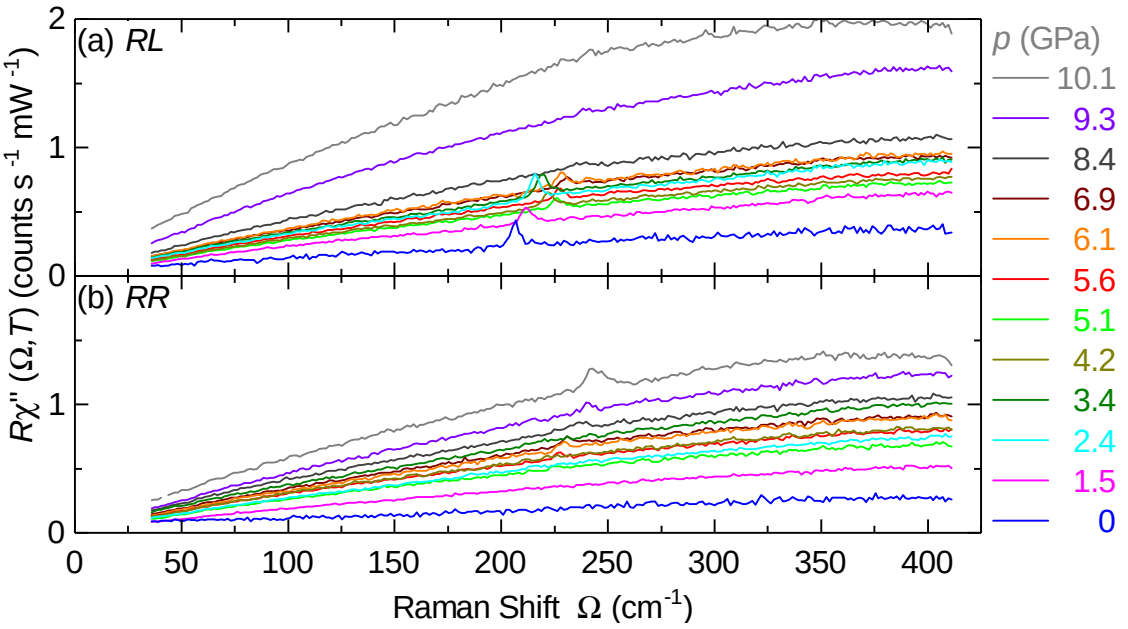

Figure A.7: High-temperature Raman spectra of $BaFe_2As_2$ at pressures as indicated for (a) RL and (b) RR polarization. The B_{1g} phonon found at $\Omega \approx 215\,\mathrm{cm}^{-1}$ in RL at $p = 0\,\mathrm{GPa}$ shifts to higher energies and vanishes when the pressure is increased. In RR polarization a peak at similar energy as the phonon appears at medium pressure and gains strength and energy when the pressure is raised further. In both polarizations the smooth background increases with p. Adopted from Ref. [188].

Fig. A.8(a) and (b) show the spectra in RL and RR polarizations, respectively, for a selected set of pressures. The spectra focus on the energy range relevant for phonons and are shifted for clarity. The dashed lines denote the lowest and highest observed peak positions of the Fe phonon in RL polarization. By fitting Voigt profiles to the peaks the pressure dependence of their energies and spectral weight can be extracted and is shown in Figs. A.8(c) and (d), respectively. The energy of the B_{1g} phonon in RL polarizations increases linearly with pressure. Above $p \approx 5\,\mathrm{GPa}$ the peak in RR polarizations is observed at an energy which is identical to that of the B_{1g} phonon within the experimental error. While the phonon in RL polarization vanishes as the pressure is increased, the peak in RR gains intensity. The total spectral weight of both modes, as shown in Fig. A.8(d), however, can be seen as varying around a constant value for pressures up to 8 GPa. Combining these observations leads to the indication that the mode in RR polarizations is in fact connected to the B_{1g} Fe phonon which apparently emerges in A_{1g} symmetry at high pressures while at the same time vanishing in B_{1g} symmetry.

This continuous crossover of the phonon mode from lower (B_{1g}) to higher (A_{1g}) symmetry is a puzzling effect. From the technical perspective the question arises

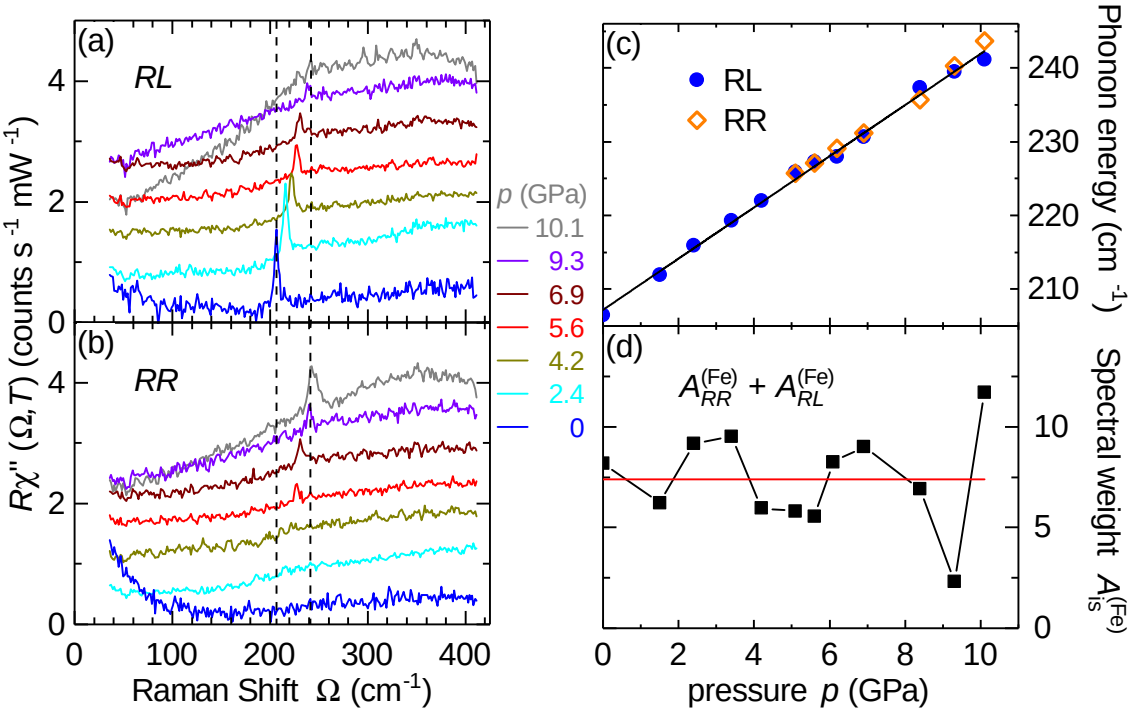

Figure A.8: High pressure symmetry crossover of the Fe B_{1g} phonon in $BaFe_2As_2$. (a,b) Raman spectra at selected pressures in (a) *RL* and (b) *RR* polarizations. The dashed lines mark the lowest and highest observed phonon position. The spectra are shifted for better visibility. (c,d) Phonon energies and sum of the spectral weights as a function of the applied pressure. The values were extracted from the raw spectra (Fig. A.7) by fitting a Voigt profile to the phonon peak. Adapted from Ref. [188].

on how this change can be described on the basis of the Raman tensor. In a purely tetragonal system the B_{1g} Raman tensor has the form shown in Eq. 6.3 with $\hat{\alpha}_{22} = -\hat{\alpha}_{11}$ and cannot change continuously to A_{1g} symmetry ($\hat{\alpha}_{22} = \hat{\alpha}_{11}$). Lowering the symmetry from D_{4h} to D_{2h} allows this transition by changing the two tensors elements with respect to each other. Taking the concept of a complex Raman tensor as introduced in Sec. 6.1.2 facilitates the creation of a 'pseudo-tetragonal' tensor where the two tensor elements have the same amplitude, $\|\hat{\alpha}_{11}\| = \|\hat{\alpha}_{22}\|$, but differ by a phase factor $\exp(-\imath\Delta\Theta)$. Tuning this phase difference as a function of pressure then creates the continuous change as observed in the experiment.

This purely technical description does not, however, answer the physical questions regarding the origin of the necessary reduction in symmetry and the driving force behind the change in the tensor elements. Changes to the lattice can be ruled out as $BaFe_2As_2$ at room temperature has a tetragonal crystal structure for all relevant pressures [253–255]. At higher pressures $p > 17\,\mathrm{GPa}$ a phase transition to a collapsed tetragonal (cT) phase is observed [254, 255], which reduces the unit cell

volume but does not bring about any change to the lattice symmetry.

Therefore the symmetry breaking must be decoupled from the lattice, making also a relationship to the low-temperature orthorhombic SDW phase unlikely. Effects of this phase extend to higher temperatures in the form of spin-fluctuations, which can be observed up to a temperature $T_f < 300\,\mathrm{K}$ [118]. This onset temperature for the fluctuations decreases upon doping as T_{SDW} is decreased and therefore any effect at room temperature for high pressures is unlikely as all experiments so far show a similar suppression of T_{SDW} by pressure [20, 256–258].

From a magnetic point of view a theoretical study [259] suggested the existence of a Lifshitz transition from a tetragonal paramagnetic to a tetragonal non-magnetic phase as a function of pressure even at high temperatures. It seems, however, unlikely that the quenching of magnetic moments would create a lowering of the symmetry which is necessary for the observed crossover.

While electronic nematicity is a prevalent property of IBS, the nematic phase of 122-type materials at $T < T_{\mathrm{s}}$ comes along with a structural distortion and, similarly to the SDW phase it precedes, is suppressed by pressure [20, 256–258]. A nematic phase above T_{s} was found in $BaFe_2(As_{1-x}P_x)_2$ [260], but too does not exist above $T^* < 200\,\mathrm{K}$ and T^* decreases when the chemical pressure is increased. The only electronic peculiarity that might have an effect at high temperatures is a non-Fermi liquid (nFL) regime [261, 262] above a quantum critical point. This feature was found in $BaFe_2(As_{1-x}P_x)_2$ where chemical pressure serves as control parameter and leads to properties comparable to applied hydrostatic pressure [243, 263]. The existence of the nFL was determined by transport and magneto-transport measurements [261] and it is found up to room temperature. Its microscopic properties regarding putative anisotropies are, however, unknown.

Regarding high energy effects, a resonance may cause a breakdown of the selection rules. With the band structure changed continuously by the external pressure one could observe a resonance profile even for a constant excitation energy $\hbar\omega_{\mathrm{i}}$. However, the breakdown of the selection rules only occurs for $\hbar\omega_{\mathrm{i}}$ close to the resonance energy, and there, one expects an increase in spectral weight of the relevant excitation which is not observed in the experiment. In fact the total spectral weight $A_{\mathrm{tot}}^{(\mathrm{Fe})} = A_{RR}^{(\mathrm{Fe})} + A_{RL}^{(\mathrm{Fe})}$ varies around a constant mean value over a wide pressure range [Fig. A.8(d)]. Comparing the raw data (Fig. A.7) to experiments outside the DAC [97], one has to note that the electronic continuum is below the measurement threshold as is the A_{1g} phonon mode. The visible change to the background intensity in Fig. A.7 is ascribed to a changing fluorescence background rather than a resonant

increase of the electronic continuum.

Therefore the origin of the putative continuous symmetry breaking in $BaFe_2As_2$ at high pressure remains unknown. Given the broad pressure range and rather continuous development of the observed anomaly, it is likely linked not to a single phase transition but rather to the continuous change of the electronic structure by pressure.

Appendix B

Sensitivity of the optical set-up

The sensitivity $s(\tilde{\nu})$ of the set-up refers to the transmission of the collection optics [(O1), $\frac{\lambda}{4}$, (P2) and $\frac{\lambda}{2}$], the spectrometer, and the CCD with its optics [(L2), (O2)] (see Fig. 4.1 for component definitions). This transmission was determined experimentally in 1997 [182] as a function of the energy $\tilde{\nu}$ and was approximated by a 5^{th} order polynomial. To normalize spectra across a wide energy range they need to be divided by this function. In 2012 the Photometrics 200 detector equipped with a TK 512 CCD chip was replaced by a Roper Scientific Pylon 100BR_eXcelon. This new CCD has a higher quantum efficiency (QE) as shown in Fig. B.1(a) and thus required an update to the sensitivity function. Additionally, a gain conversion

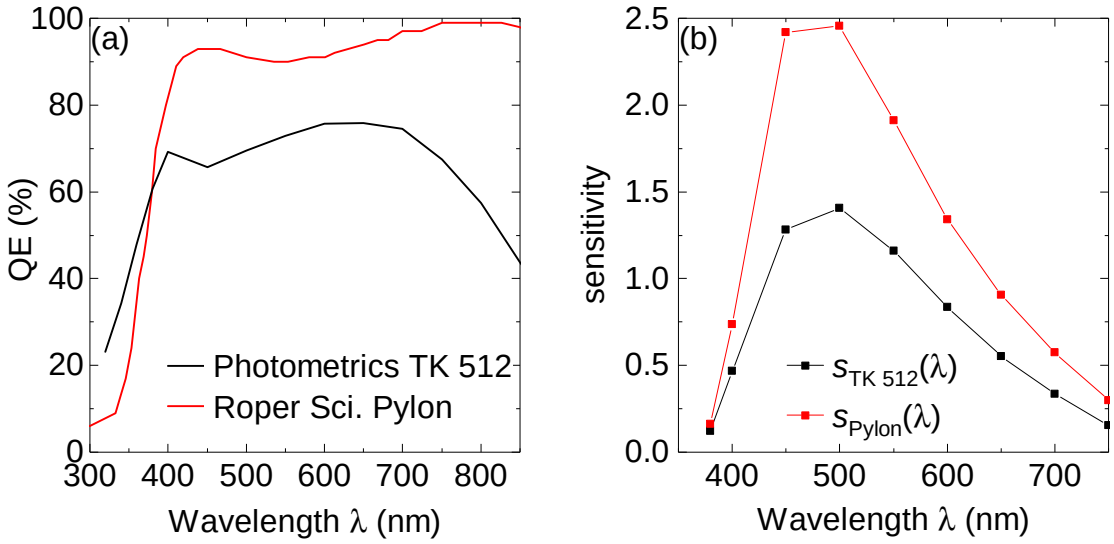

Figure B.1: (a) Quantum efficiencies of the Photometrics 200 (TK 512) CCD (black) and the Roper Scientific Pylon CCD (red) as a function of the wavelength of the detected light. (b) Sensitivity using the Photometrics TK 512 CCD (black) and the Roper Pylon CCD (red). Data based on Ref. [182]

factor of 0.75 needs to be accounted for. This factor depends on the gain setting of the CCD and has the unit electrons (and, correspondingly, photons) per count. For the Photometrics CCD the respective gain ($1.41^{e^-}/_{count}$) was already taken care of in the calibration.

Dividing the sensitivity $s_{TK512}(\tilde{\nu})$ of the set-up with the Photometrics detector [182] shown as black line in Fig. B.1(b) by the QE of the Photometrics CCD [black line in Fig. B.1(a)] yields the contribution from the collection optics and spectrometer $s^*(\tilde{\nu})$. By multiplying $s^*(\tilde{\nu})$ with the QE of the Pylon CCD [red line in Fig. B.1(a)] and the new gain factor $1/0.75$ the new sensitivity $s_{Pylon}(\tilde{\nu})$ is obtained [red dots and line in Fig. B.1(b)]. $s_{Pylon}(\tilde{\nu})$ can again be approximated by a 5^{th} order polynomial. Here the energy $\tilde{\nu}$ is in units of absolute wave numbers (abs. cm^{-1}).

$$s(\tilde{\nu}) = -362.33571 + 0.10232 * \tilde{\nu} - 1.1424 \cdot 10^{-5} \cdot \tilde{\nu}^2 + 6.28268 \cdot 10^{-10} \cdot \tilde{\nu}^3 \\ -1.69303 \cdot 10^{-14} \cdot \tilde{\nu}^4 + 1.78365 \cdot 10^{-19} \cdot \tilde{\nu}^5 \quad \text{(B.1)}$$

Appendix C

Resolution of the spectrometer

The energy of the exciting photons and the resolution of the spectrometer must be determined experimentally. The resolution $\Delta\tilde{\nu}$ of the double-monochromator is given by the width M of the intermediate slit (see Fig. 4.1) and depends on the wavelength. Both, λ_i to be used as reference ($\Omega = 0\,\mathrm{cm}^{-1}$), and the resolution $\Delta\tilde{\nu}(\lambda_\mathrm{i},\mathrm{M})$ can be determined by measuring the laser line. To this end the laser light is diffusively scattered by blocking its path by a sheet of paper. Another diffusion disc is placed in front of the spectrometer entrance slit [(SL1) in Fig. 4.1] leading to a uniform illumination of the entrance slit. Then, the intensity of the transmitted light is determined (similar to measuring a spectrum) in a range of $\pm 15\,\mathrm{cm}^{-1}$ around the expected value of λ_i. As the width of the laser light is narrow ($\Gamma_\mathrm{las} = \mathcal{O}(10\,\mathrm{MHz})$ or better) and the dispersion by the gratings is negligible for M in the range of 500 µm the measurement at various grating positions (corresponding to the $\pm 15\,\mathrm{cm}^{-1}$) can be seen as shifting the rectangular entrance slit with respect to the intermediate slit, which yields a triangular profile. The center position of this profile is λ_i, and its FWHM is a good approximation to the spectrometer resolution $\Delta\tilde{\nu}(\lambda_\mathrm{i})$ for a fixed width M of the intermediate slit. Typically $M = 550\,\mu\mathrm{m}$ is used. The corresponding resolution $\Delta\tilde{\nu}(\lambda_\mathrm{i}, M = 550\,\mu\mathrm{m})$ was determined for all laser lines used and is compiled in Table C.1.

Approx. wavelength (nm)	Exp. energy ν (abs. cm^{-1})	$\Delta\tilde{\nu}(\lambda_i, M = 550\,\mu m)$ (cm^{-1})
407	24577	11.6
413	24199	10.9
458	21834	8.9
476	20987	8.3
488	20490	7.9
496	20135	7.4
514	19434	6.4
521	19198	6.2
531	18835	6.1
532	18797	6.0
568	17596	4.9
575	17391	4.7
646	15453	3.4
660	15165	3.4
676	14780	2.8

Table C.1: Laser lines and the corresponding resolution $\Delta\tilde{\nu}(\lambda_i)$ of the spectrometer for a width $M = 550\,\mu m$ of the intermediate slit.

List of publications

- A. Baum, Y. Li, M. Tomić, N. Lazarević, D. Jost, F. Löffler, B. Muschler, T. Böhm, J.-H. Chu, I. R. Fisher, R. Valentí, I. I. Mazin, and R. Hackl. Interplay of lattice, electronic, and spin degrees of freedom in detwinned $BaFe_2As_2$: A Raman scattering study. *Phys. Rev. B* **98**, 075113 (2018)

- A. Baum, A. Milosavljević, N. Lazarević, M. M. Radonjić, B. Nikolić, M. Mitschek, Z. I. Maranloo, M. Šćepanović, M. Grujić-Brojčin, N. Stojilović, M. Opel, A. Wang, C. Petrovic, Z. V. Popović, and R. Hackl. Phonon anomalies in FeS. *Phys. Rev. B* **97**, 054306 (2018)

- N. Chelwani, A. Baum, T. Böhm, M. Opel, F. Venturini, L. Tassini, A. Erb, H. Berger, L. Forró, and R. Hackl. Magnetic excitations and amplitude fluctuations in insulating cuprates. *Phys. Rev. B* **97**, 024407 (2018)

- T. Böhm, R. Hosseinian Ahangharnejhad, D. Jost, A. Baum, B. Muschler, F. Kretzschmar, P. Adelmann, T. Wolf, H.-H. Wen, J.-H. Chu, I. R. Fisher, and R. Hackl. Superconductivity and fluctuations in $Ba_{1-p}K_pFe_2As_2$ and $Ba(Fe_{1-n}Co_n)_2As_2$. *physica status solidi (b)* **254**, 1600308 (2017)

- U. Ralević, N. Lazarević, A. Baum, H.-M. Eiter, R. Hackl, P. Giraldo-Gallo, I. R. Fisher, C. Petrovic, R. Gajić, and Z. V. Popović. Charge density wave modulation and gap measurements in $CeTe_3$. *Phys. Rev. B* **94**, 165132 (2016)

- F. Kretzschmar, T. Böhm, U. Karahasanovic, B. Muschler, A. Baum, D. Jost, J. Schmalian, S. Caprara, M. Grilli, C. Di Castro, J. G. Analytis, J.-H. Chu, I. R. Fisher, and R. Hackl. Critical spin fluctuations and the origin of nematic order in $Ba(Fe_{1-x}Co_x)_2As_2$. *Nat. Phys.* **12**, 560 (2016)

- F. Kretzschmar, B. Muschler, T. Böhm, A. Baum, R. Hackl, H.-H. Wen, V. Tsurkan, J. Deisenhofer, and A. Loidl. Raman-Scattering Detection of

Nearly Degenerate s-Wave and d-Wave Pairing Channels in Iron-Based $Ba_{0.6}K_{0.4}Fe_2As_2$ and $Rb_{0.8}Fe_{1.6}Se_2$ Superconductors. *Phys. Rev. Lett.* **110**, 187002 (2013)

Submitted

- S. Djurdjić-Mijin, A. Šolajić, J. Pešić, M. Šćepanović, Y. Liu, A. Baum, C. Petrovic, N. Lazarević, and Z. V. Popović. Lattice dynamics and phase transition in CrI_3 single crystals (2018). arXiv e-print 1807.03259v1
  accepted for publication in Phys. Rev. B

- A. Baum, H. N. Ruiz, N. Lazarević, Y. Wang, T. Böhm, R. Hosseinian Ahangharnejhad, P. Adelmann, T. Wolf, Z. V. Popović, B. Moritz, T. P. Devereaux, and R. Hackl. Frustrated spin order and stripe fluctuations in FeSe (2018). arXiv e-print 1709.08998v2
  accepted for publication in Commun. Phys.

- T. Böhm, F. Kretzschmar, A. Baum, M. Rehm, D. Jost, R. Hosseinian Ahangharnejhad, R. Thomale, C. Platt, T. A. Maier, W. Hanke, B. Moritz, T. P. Devereaux, D. J. Scalapino, S. Maiti, P. J. Hirschfeld, P. Adelmann, T. Wolf, H.-H. Wen, and R. Hackl. Microscopic pairing fingerprint of the iron-based superconductor $Ba_{1-x}K_xFe_2As_2$ (2017). arXiv e-print 1703.07749
  accepted for publication in npj Quantum Mater.

Bibliography

[1] Titus Lucretius Carus. De Rerum Natura. Poem (1st century BC). URL `https://la.wikisource.org/wiki/De_rerum_natura_(Titus_Lucretius_Carus)/Liber_VI`.

[2] W. Gilbert. *De Magnete, Magneticisque Corporibus, et de Magno Magnete Tellure*. Peter Short, London (1600).

[3] J.-L. Lagrange. Sur l'Attraction des Sphéroïdes Elliptiques. In *Œuvres de Lagrange*, volume 125, chapter 14, page 619. Mémoires de l'Académie de Berlin (1773).

[4] A.-M. Ampère and J. Babinet. *Exposé des nouvelles découvertes sur l'électricité et le magnétisme*. Méquignon-Marvis Paris, Rue de l'école de médecine 3 (1822).

[5] M. Faraday. *Experimental Researches in Electricity*, volume 1–2. J. M. Dent & Sons Ltd. (1839).

[6] H. C. Ørsted. Experimenta circa effectum conflictus electrici in acum magneticam. self published (1820).

[7] J. C. Maxwell. *The dynamical theory of the electromagnetic field*. Wipf and Stock (1865).

[8] C. F. Gauss. *Theoria attractionis corporum sphaeroidicorum ellipticorum homogeneorum methodo nova tractata* (1813).

[9] J.-B. Biot and F. Savart. Note sur le Magnétisme de la pile de Volta. *Ann. Chim. Phys.* **15**, 222 (1820).

[10] N. Bohr. *Studier over Metallernes Elektrontheori*. Dissertation, Københavens Universitet (1911). URL `http://dx.doi.org/10.1016/S1876-0503(08)70015-X`.

[11] H.-J. van Leeuwen. Problèmes de la théorie électronique du magnétisme. *J. Phys. Radium* **2**, 361 (1921).

[12] S. Goudsmit and G. Uhlenbeck. Opmerking over de Spectra van Watersof en Helium. *Physica (Utrecht)* **5**, 266 (1925).

[13] P. A. M. Dirac. The quantum theory of dispersion. *Proc. R. Soc. Lond. A* **114**, 710 (1927).

[14] W. Pauli. Über den Zusammenhang des Abschlusses der Elektronengruppen im Atom mit der Komplexstruktur der Spektren. *Z. Phys.* **31**, 765 (1925).

[15] F. Hund. Zur Deutung der Molekelspektren. I. *Z. Phys.* **40**, 742 (1927).

[16] F. Hund. Zur Deutung der Molekelspektren. II. *Z. Phys.* **42**, 93 (1927).

[17] J.-H. Chu, J. G. Analytis, C. Kucharczyk, and I. R. Fisher. Determination of the phase diagram of the electron-doped superconductor $Ba(Fe_{1-x}Co_x)_2As_2$. *Phys. Rev. B* **79**, 014506 (2009).

[18] S. Jiang, H. Xing, G. Xuan, C. Wang, Z. Ren, C. Feng, J. Dai, Z. Xu, and G. Cao. Superconductivity up to 30 K in the vicinity of the quantum critical point in $BaFe_2(As_{1-x}P_x)_2$. *J. Phys.: Condens. Matter* **21**, 382203 (2009).

[19] D. Johrendt and R. Pöttgen. Superconductivity, magnetism and crystal chemistry of $Ba_{1-x}K_xFe_2As_2$. *Physica C* **469**, 332 (2009).

[20] E. Colombier, S. L. Bud'ko, N. Ni, and P. C. Canfield. Complete pressure-dependent phase diagrams for $SrFe_2As_2$ and $BaFe_2As_2$. *Phys. Rev. B* **79**, 224518 (2009).

[21] Q. Huang, Y. Qiu, W. Bao, M. A. Green, J. W. Lynn, Y. C. Gasparovic, T. Wu, G. Wu, and X. H. Chen. Neutron-Diffraction Measurements of Magnetic Order and a Structural Transition in the Parent $BaFe_2As_2$ Compound of FeAs-Based High-Temperature Superconductors. *Phys. Rev. Lett.* **101**, 257003 (2008).

[22] M. Rotter, M. Pangerl, M. Tegel, and D. Johrendt. Superconductivity and Crystal Structures of $(Ba_{1-x}K_x)Fe_2As_2$ (x=0-1). *Angew. Chem. Int. Ed.* **47**, 7949 (2008).

[23] M. Rotter, M. Tegel, D. Johrendt, I. Schellenberg, W. Hermes, and R. Pöttgen. Spin-density-wave anomaly at 140 K in the ternary iron arsenide $BaFe_2As_2$. *Phys. Rev. B* **78**, 020503 (2008).

[24] R. M. Fernandes and J. Schmalian. Manifestations of nematic degrees of freedom in the magnetic, elastic, and superconducting properties of the iron pnictides. *Supercond. Sci. Technol.* **25**, 084005 (2012).

[25] J.-H. Chu, J. G. Analytis, K. D. Greve, P. L. McMahon, Z. Islam, Y. Yamamoto, and I. R. Fisher. In-Plane Resistivity Anisotropy in an Underdoped Iron Arsenide Superconductor. *Science* **329**, 824 (2010).

[26] J. J. Ying, X. F. Wang, T. Wu, Z. J. Xiang, R. H. Liu, Y. J. Yan, A. F. Wang, M. Zhang, G. J. Ye, P. Cheng, J. P. Hu, and X. H. Chen. Measurements of the Anisotropic In-Plane Resistivity of Underdoped FeAs-Based Pnictide Superconductors. *Phys. Rev. Lett.* **107**, 067001 (2011).

[27] A. Dusza, A. Lucarelli, F. Pfuner, J.-H. Chu, I. R. Fisher, and L. Degiorgi. Anisotropic charge dynamics in detwinned $Ba(Fe_{1-x}Co_x)_2As_2$. *EPL* **93**, 37002 (2011).

[28] A. Dusza, A. Lucarelli, A. Sanna, S. Massidda, J.-H. Chu, I. R. Fisher, and L. Degiorgi. Anisotropic in-plane optical conductivity in detwinned $Ba(Fe_{1-x}Co_x)_2As_2$. *New J. Phys.* **14**, 023020 (2012).

[29] M. Nakajima, T. Liang, S. Ishida, Y. Tomioka, K. Kihou, C. H. Lee, A. Iyo, H. Eisaki, T. Kakeshita, T. Ito, and S. Uchida. Unprecedented anisotropic metallic state in undoped iron arsenide $BaFe_2As_2$ revealed by optical spectroscopy. *Proc. Natl. Acad. Sci.* **108**, 12238 (2011).

[30] M. Yi, D. Lu, J.-H. Chu, J. G. Analytis, A. P. Sorini, A. F. Kemper, B. Moritz, S.-K. Mo, R. G. Moore, M. Hashimoto, W.-S. Lee, Z. Hussain, T. P. Devereaux, I. R. Fisher, and Z.-X. Shen. Symmetry-breaking orbital anisotropy observed for detwinned $Ba(Fe_{1-x}Co_x)_2As_2$ above the spin density wave transition. *Proc. Natl. Acad. Sci.* **108**, 6878 (2011).

[31] T. U. Böhm. *The case for Spin-fluctuation induced pairing in* $Ba_{1-x}K_xFe_2As_2$. Dissertation, Technische Universität München (2017).

[32] T. Böhm, F. Kretzschmar, A. Baum, M. Rehm, D. Jost, R. Hosseinian Ahangharnejhad, R. Thomale, C. Platt, T. A. Maier, W. Hanke, B. Moritz, T. P.

Devereaux, D. J. Scalapino, S. Maiti, P. J. Hirschfeld, P. Adelmann, T. Wolf, H.-H. Wen, and R. Hackl. Microscopic pairing fingerprint of the iron-based superconductor $Ba_{1-x}K_xFe_2As_2$ (2017). arXiv e-print 1703.07749.

[33] E. Uykur, T. Kobayashi, W. Hirata, S. Miyasaka, S. Tajima, and C. A. Kuntscher. Optical investigation of $BaFe_2(As_{0.77}P_{0.23})_2$: Spin-fluctuation-mediated superconductivity under pressure. *Phys. Rev. B* **95**, 214512 (2017).

[34] U. Pachmayr, N. Fehn, and D. Johrendt. Structural transition and superconductivity in hydrothermally synthesized FeX (X = S, Se). *Chem. Commun.* **52**, 194 (2016).

[35] X. Lai, H. Zhang, Y. Wang, X. Wang, X. Zhang, J. Lin, and F. Huang. Observation of Superconductivity in Tetragonal FeS. *J. Am. Chem. Soc.* **137**, 10148 (2015).

[36] T. M. McQueen, A. J. Williams, P. W. Stephens, J. Tao, Y. Zhu, V. Ksenofontov, F. Casper, C. Felser, and R. J. Cava. Tetragonal-to-Orthorhombic Structural Phase Transition at 90 K in the Superconductor $Fe_{1.01}Se$. *Phys. Rev. Lett.* **103**, 057002 (2009).

[37] H. Kotegawa, S. Masaki, Y. Awai, H. Tou, Y. Mizuguchi, and Y. Takano. Evidence for Unconventional Superconductivity in Arsenic-Free Iron-Based Superconductor FeSe: A ^{77}Se-NMR Study. *J. Phys. Soc. Jpn.* **77**, 113703 (2008).

[38] S.-H. Baek, D. V. Efremov, J. M. Ok, J. S. Kim, J. van den Brink, and B. Büchner. Orbital-driven nematicity in FeSe. *Nat. Mater.* **14**, 210 (2015).

[39] F.-C. Hsu, J.-Y. Luo, K.-W. Yeh, T.-K. Chen, T.-W. Huang, P. M. Wu, Y.-C. Lee, Y.-L. Huang, Y.-Y. Chu, D.-C. Yan, and M.-K. Wu. Superconductivity in the PbO-type structure α-FeSe. *Proc. Natl. Acad. Sci.* **105**, 14262 (2008).

[40] Y. Mizuguchi, F. Tomioka, S. Tsuda, T. Yamaguchi, and Y. Takano. Superconductivity at 27K in tetragonal FeSe under high pressure. *Appl. Phys. Lett.* **93**, 152505 (2008).

[41] M. Bendele, A. Amato, K. Conder, M. Elender, H. Keller, H.-H. Klauss, H. Luetkens, E. Pomjakushina, A. Raselli, and R. Khasanov. Pressure Induced Static Magnetic Order in Superconducting $FeSe_{1-x}$. *Phys. Rev. Lett.* **104**, 087003 (2010).

[42] M. Bendele, A. Ichsanow, Y. Pashkevich, L. Keller, T. Strässle, A. Gusev, E. Pomjakushina, K. Conder, R. Khasanov, and H. Keller. Coexistence of superconductivity and magnetism in $FeSe_{1-x}$ under pressure. *Phys. Rev. B* **85**, 064517 (2012).

[43] C. de la Cruz, Q. Huang, J. Lynn, J. Li, W. R. II, J. Zarestky, H. Mook, G. Chen, J. Luo, N. Wang, and P. Dai. Magnetic order close to superconductivity in the iron-based layered $LaO_{1-x}F_xFeAs$ systems. *Nature* **453**, 899 (2008).

[44] W. Bao, Y. Qiu, Q. Huang, M. A. Green, P. Zajdel, M. R. Fitzsimmons, M. Zhernenkov, S. Chang, M. Fang, B. Qian, E. K. Vehstedt, J. Yang, H. M. Pham, L. Spinu, and Z. Q. Mao. Tunable $(\delta\pi, \delta\pi)$-Type Antiferromagnetic Order in α-Fe(Te,Se) Superconductors. *Phys. Rev. Lett.* **102**, 247001 (2009).

[45] Y. Qiu, W. Bao, Y. Zhao, C. Broholm, V. Stanev, Z. Tesanovic, Y. C. Gasparovic, S. Chang, J. Hu, B. Qian, M. Fang, and Z. Mao. Spin Gap and Resonance at the Nesting Wave Vector in Superconducting $FeSe_{0.4}Te_{0.6}$. *Phys. Rev. Lett.* **103**, 067008 (2009).

[46] J. K. Glasbrenner, I. I. Mazin, H. O. Jeschke, P. J. Hirschfeld, R. M. Fernandes, and R. Valenti. Effect of magnetic frustration on nematicity and superconductivity in iron chalcogenides. *Nat. Phys.* **11**, 953 (2015).

[47] I. I. Mazin, M. D. Johannes, L. Boeri, K. Koepernik, and D. J. Singh. Problems with reconciling density functional theory calculations with experiment in ferropnictides. *Phys. Rev. B* **78**, 085104 (2008).

[48] V. Anisimov, I. Nekrasov, D. Kondakov, T. Rice, and M. Sigrist. Orbital-selective Mott-insulator transition in $Ca_{2-x}Sr_xRuO_4$. *Eur. Phys. J. B* **25**, 191 (2002).

[49] L. de' Medici, S. R. Hassan, M. Capone, and X. Dai. Orbital-Selective Mott Transition out of Band Degeneracy Lifting. *Phys. Rev. Lett.* **102**, 126401 (2009).

[50] I. Leonov, S. L. Skornyakov, V. I. Anisimov, and D. Vollhardt. Correlation-Driven Topological Fermi Surface Transition in FeSe. *Phys. Rev. Lett.* **115**, 106402 (2015).

[51] K. M. Stadler, Z. P. Yin, J. von Delft, G. Kotliar, and A. Weichselbaum. Dynamical Mean-Field Theory Plus Numerical Renormalization-Group Study of Spin-Orbital Separation in a Three-Band Hund Metal. *Phys. Rev. Lett.* **115**, 136401 (2015).

[52] F. Wang, S. A. Kivelson, and D.-H. Lee. Nematicity and quantum paramagnetism in FeSe. *Nat. Phys.* **11**, 959 (2015).

[53] S. L. Skornyakov, V. I. Anisimov, D. Vollhardt, and I. Leonov. Effect of electron correlations on the electronic structure and phase stability of FeSe upon lattice expansion. *Phys. Rev. B* **96**, 035137 (2017).

[54] K. Haule and G. Kotliar. Coherence-incoherence crossover in the normal state of iron oxypnictides and importance of Hund's rule coupling. *New J. Phys.* **11**, 025021 (2009).

[55] Q. Si. Electrons on the verge. *Nat. Phys.* **5**, 629 (2009).

[56] Z. P. Yin, K. Haule, and G. Kotliar. Magnetism and charge dynamics in iron pnictides. *Nat. Phys.* **7**, 294 (2011).

[57] L. de' Medici, G. Giovannetti, and M. Capone. Selective Mott Physics as a Key to Iron Superconductors. *Phys. Rev. Lett.* **112**, 177001 (2014).

[58] C. F. Hirjibehedin. Magnetic atoms: The makings of a Hund's metal. *Nat. Nanotechnol.* **10**, 914 (2015).

[59] M. Yi, Y. Zhang, Z.-X. Shen, and D. Lu. Role of the orbital degree of freedom in iron-based superconductors. *npj Quantum Mater.* **2**, 57 (2017).

[60] C. Mirri, A. Dusza, S. Bastelberger, M. Chinotti, J.-H. Chu, H.-H. Kuo, I. R. Fisher, and L. Degiorgi. Electrodynamic response in the electronic nematic phase of $BaFe_2As_2$. *Phys. Rev. B* **93**, 085114 (2016).

[61] Z.-G. Chen, L. Wang, Y. Song, X. Lu, H. Luo, C. Zhang, P. Dai, Z. Yin, K. Haule, and G. Kotliar. Two-Dimensional Massless Dirac Fermions in Antiferromagnetic $A Fe_2As_2$ (A=Ba, Sr). *Phys. Rev. Lett.* **119**, 096401 (2017).

[62] F. Venturini, M. Opel, T. P. Devereaux, J. K. Freericks, I. Tüttő, B. Revaz, E. Walker, H. Berger, L. Forró, and R. Hackl. Observation of an Unconventional Metal-Insulator Transition in Overdoped CuO_2 Compounds. *Phys. Rev. Lett.* **89**, 107003 (2002).

[63] H.-M. Eiter, M. Lavagnini, R. Hackl, E. A. Nowadnick, A. F. Kemper, T. P. Devereaux, J.-H. Chu, J. G. Analytis, I. R. Fisher, and L. Degiorgi. Alternative route to charge density wave formation in multiband systems. *Proc. Natl. Acad. Sci.* **110**, 64 (2013).

[64] P. A. Fleury and R. Loudon. Scattering of Light by One- and Two-Magnon Excitations. *Phys. Rev.* **166**, 514 (1968).

[65] Y. Kamihara, H. Hiramatsu, M. Hirano, R. Kawamura, H. Yanagi, T. Kamiya, and H. Hosono. Iron-Based Layered Superconductor: LaOFeP. *J. Am. Chem. Soc.* **128**, 10012 (2006).

[66] Y. Kamihara, T. Watanabe, M. Hirano, and H. Hosono. Iron-Based Layered Superconductor La[$O_{1-x}F_x$]FeAs (x = 0.05-0.12) with T_c = 26 K. *J. Am. Chem. Soc.* **130**, 3296 (2008).

[67] M. Rotter, M. Tegel, and D. Johrendt. Superconductivity at 38 K in the Iron Arsenide ($Ba_{1-x}K_x$)Fe_2As_2. *Phys. Rev. Lett.* **101**, 107006 (2008).

[68] H. Takahashi, K. Igawa, K. Arii, Y. Kamihara, M. Hirano, and H. Hosono. Superconductivity at 43 K in an iron-based layered compound $LaO_{1-x}F_xFeAs$. *Nature* **453**, 376 (2008).

[69] X. H. Chen, T. Wu, G. Wu, R. H. Liu, H. Chen, and D. F. Fang. Superconductivity at 43 K in $SmFeAsO_{1-x}F_x$. *Nature* **453**, 761 (2008).

[70] Z.-A. Ren, J. Yang, W. Lu, W. Yi, X.-L. Shen, Z.-C. Li, G.-C. Che, X.-L. Dong, L.-L. Sun, F. Zhou, and Z.-X. Zhao. Superconductivity in the iron-based F-doped layered quaternary compound Nd[$O_{1-x}F_x$]FeAs. *EPL* **82**, 57002 (2008).

[71] N. D. Zhigadlo, S. Katrych, Z. Bukowski, S. Weyeneth, R. Puzniak, and J. Karpinski. Single crystals of superconducting $SmFeAsO_{1-x}F_y$ grown at high pressure. *J. Phys.: Condens. Matter* **20**, 342202 (2008).

[72] K. Ishida, Y. Nakai, and H. Hosono. To What Extent Iron-Pnictide New Superconductors Have Been Clarified: A Progress Report. *J. Phys. Soc. Jpn.* **78**, 062001 (2009).

[73] D. C. Johnston. The Puzzle of High Temperature Superconductivity in Layered Iron Pnictides and Chalcogenides . *Adv. Phys.* **59**, 803 (2010).

[74] D. N. Basov and A. V. Chubukov. Manifesto for a higher T_c. *Nat. Phys.* **7**, 272 (2011).

[75] I. Mazin. Iron Superconductivity Weathers Another Storm. *Phys.* **4**, 26 (2011).

[76] J. G. Bednorz and K. A. Müller. Possible high T_c superconductivity in the Ba-La-Cu-O System. *Z. Phys. B* **64**, 189 (1986).

[77] J. G. Bednorz and K. A. Müller. Perovskite-type oxides -The new approach to high-T_c superconductivity. *Rev. Mod. Phys.* **60**, 585 (1988).

[78] R. M. Fernandes, A. V. Chubukov, and J. Schmalian. What drives nematic order in iron-based superconductors? *Nat. Phys.* **10**, 97 (2014).

[79] A. V. Chubukov, R. M. Fernandes, and J. Schmalian. Origin of nematic order in FeSe. *Phys. Rev. B* **91**, 201105 (2015).

[80] A. V. Chubukov, M. Khodas, and R. M. Fernandes. Magnetism, Superconductivity, and Spontaneous Orbital Order in Iron-Based Superconductors: Which Comes First and Why? *Phys. Rev. X* **6**, 041045 (2016).

[81] A. E. Böhmer and A. Kreisel. Nematicity, magnetism and superconductivity in FeSe. *J. Phys.: Condens. Matter* **30**, 023001 (2018).

[82] J. Paglione and R. L. Greene. High-temperature superconductivity in iron-based materials. *Nat. Phys.* **6**, 645 (2010).

[83] G. R. Stewart. Superconductivity in iron compounds. *Rev. Mod. Phys.* **83**, 1589 (2011).

[84] D. J. Singh. Electronic structure and doping in $BaFe_2As_2$ and LiFeAs: Density functional calculations. *Phys. Rev. B* **78**, 094511 (2008).

[85] V. Vildosola, L. Pourovskii, R. Arita, S. Biermann, and A. Georges. Bandwidth and Fermi surface of iron oxypnictides: Covalency and sensitivity to structural changes. *Phys. Rev. B* **78**, 064518 (2008).

[86] A. Baum, Y. Li, M. Tomić, N. Lazarević, D. Jost, F. Löffler, B. Muschler, T. Böhm, J.-H. Chu, I. R. Fisher, R. Valentí, I. I. Mazin, and R. Hackl. Interplay of lattice, electronic, and spin degrees of freedom in detwinned $BaFe_2As_2$: A Raman scattering study. *Phys. Rev. B* **98**, 075113 (2018).

[87] A. Subedi, L. Zhang, D. J. Singh, and M. H. Du. Density functional study of FeS, FeSe, and FeTe: Electronic structure, magnetism, phonons, and superconductivity. *Phys. Rev. B* **78**, 134514 (2008).

[88] M. A. Tanatar, N. Ni, G. D. Samolyuk, S. L. Bud'ko, P. C. Canfield, and R. Prozorov. Resistivity anisotropy of AFe_2As_2 (A=Ca, Sr, Ba): Direct versus Montgomery technique measurements. *Phys. Rev. B* **79**, 134528 (2009).

[89] X. F. Wang, T. Wu, G. Wu, H. Chen, Y. L. Xie, J. J. Ying, Y. J. Yan, R. H. Liu, and X. H. Chen. Anisotropy in the Electrical Resistivity and Susceptibility of Superconducting $BaFe_2As_2$ Single Crystals. *Phys. Rev. Lett.* **102**, 117005 (2009).

[90] X. H. Chen, M. Yu, K. Q. Ruan, S. Y. Li, Z. Gui, G. C. Zhang, and L. Z. Cao. Anisotropic resistivities of single-crystal $Bi_2Sr_2CaCu_2O_{8+\delta}$ with different oxygen content. *Phys. Rev. B* **58**, 14219 (1998).

[91] M. Nakajima, S. Ishida, T. Tanaka, K. Kihou, Y. Tomioka, T. Saito, C. H. Lee, H. Fukazawa, Y. Kohori, T. Kakeshita, A. Iyo, T. Ito, H. Eisaki, and S. Uchida. Normal-state charge dynamics in doped $BaFe_2As_2$: Roles of doping and necessary ingredients for superconductivity. *Sci. Rep.* **4**, 5873 (2014).

[92] V. Zinth and D. Johrendt. The interplay of electron doping and chemical pressure in $Ba(Fe_{1-y}Co_y)_2(As_{1-x}P_x)_2$. *EPL* **98**, 57010 (2012).

[93] A. E. Böhmer, F. Hardy, F. Eilers, D. Ernst, P. Adelmann, P. Schweiss, T. Wolf, and C. Meingast. Lack of coupling between superconductivity and orthorhombic distortion in stoichiometric single-crystalline FeSe. *Phys. Rev. B* **87**, 180505 (2013).

[94] M. A. Tanatar, A. Kreyssig, S. Nandi, N. Ni, S. L. Bud'ko, P. C. Canfield, A. I. Goldman, and R. Prozorov. Direct imaging of the structural domains in the iron pnictides AFe_2As_2 (A=Ca,Sr,Ba). *Phys. Rev. B* **79**, 180508 (2009).

[95] C. Dhital, Z. Yamani, W. Tian, J. Zeretsky, A. S. Sefat, Z. Wang, R. J. Birgeneau, and S. D. Wilson. Effect of Uniaxial Strain on the Structural and Magnetic Phase Transitions in $BaFe_2As_2$. *Phys. Rev. Lett.* **108**, 087001 (2012).

[96] T. Liang, M. Nakajima, K. Kihou, Y. Tomioka, T. Ito, C. Lee, H. Kito, A. Iyo, H. Eisaki, T. Kakeshita, and S. Uchida. Effects of uniaxial pressure and

annealing on the resistivity of $Ba(Fe_{1-x}Co_x)_2As_2$. *J. Phys. Chem. Solids* **72**, 418 (2011).

[97] A. Baum. *Untersuchung des Spindichtewellen-Übergangs in $BaFe_2As_2$*. Diplomarbeit, Technische Universität München (2012).

[98] T. Yildirim. Frustrated magnetic interactions, giant magneto-elastic coupling, and magnetic phonons in iron-pnictides. *Physica C* **469**, 425 (2009).

[99] A. E. Böhmer, P. Burger, F. Hardy, T. Wolf, P. Schweiss, R. Fromknecht, H. v. Löhneysen, C. Meingast, H. K. Mak, R. Lortz, S. Kasahara, T. Terashima, T. Shibauchi, and Y. Matsuda. Thermodynamic phase diagram, phase competition, and uniaxial pressure effects in $BaFe_2(As_{1-x}P_x)_2$ studied by thermal expansion. *Phys. Rev. B* **86**, 094521 (2012).

[100] M. R. Norman. The Challenge of Unconventional Superconductivity. *Science* **332**, 196 (2011).

[101] S. Aswartham, G. Behr, L. Harnagea, D. Bombor, A. Bachmann, I. V. Morozov, V. B. Zabolotnyy, A. A. Kordyuk, T. K. Kim, D. V. Evtushinsky, S. V. Borisenko, A. U. B. Wolter, C. Hess, S. Wurmehl, and B. Büchner. Suppressed superconductivity in charge-doped $Li(Fe_{1-x}Co_x)As$ single crystals. *Phys. Rev. B* **84**, 054534 (2011).

[102] S. J. Zhang, X. C. Wang, Q. Q. Liu, Y. X. Lv, X. H. Yu, Z. J. Lin, Y. S. Zhao, L. Wang, Y. Ding, H. K. Mao, and C. Q. Jin. Superconductivity at 31 K in the "111"-type iron arsenide superconductor $Na_{1-x}FeAs$ induced by pressure. *EPL* **88**, 47008 (2009).

[103] A. S. Sefat and D. J. Singh. Chemistry and electronic structure of iron-based superconductors. *MRS Bull.* **36**, 614 (2011).

[104] S. Hosoi, K. Matsuura, K. Ishida, H. Wang, Y. Mizukami, T. Watashige, S. Kasahara, Y. Matsuda, and T. Shibauchi. Nematic quantum critical point without magnetism in $FeSe_{1-x}S_x$ superconductors. *Proc. Natl. Acad. Sci.* **113**, 8139 (2016).

[105] T. M. McQueen, Q. Huang, V. Ksenofontov, C. Felser, Q. Xu, H. Zandbergen, Y. S. Hor, J. Allred, A. J. Williams, D. Qu, J. Checkelsky, N. P. Ong, and R. J. Cava. Extreme sensitivity of superconductivity to stoichiometry in $Fe_{1+\delta}Se$. *Phys. Rev. B* **79**, 014522 (2009).

[106] S. Chiba. The Magnetic Properties and Phase Diagram of Iron Tellurium System. *J. Phys. Soc. Jpn.* **10**, 837 (1955).

[107] S. Li, C. de la Cruz, Q. Huang, Y. Chen, J. W. Lynn, J. Hu, Y.-L. Huang, F.-C. Hsu, K.-W. Yeh, M.-K. Wu, and P. Dai. First-order magnetic and structural phase transitions in $Fe_{1+y}Se_xTe_{1-x}$. *Phys. Rev. B* **79**, 054503 (2009).

[108] K.-W. Yeh, T.-W. Huang, Y. lin Huang, T.-K. Chen, F.-C. Hsu, P. M. Wu, Y.-C. Lee, Y.-Y. Chu, C.-L. Chen, J.-Y. Luo, D.-C. Yan, and M.-K. Wu. Tellurium substitution effect on superconductivity of the α-phase iron selenide. *EPL* **84**, 37002 (2008).

[109] D. Vaughan and M. Ridout. Mössbauer studies of some sulphide minerals. *J. Inorg. Nucl. Chem.* **33**, 741 (1971).

[110] S. Holenstein, U. Pachmayr, Z. Guguchia, S. Kamusella, R. Khasanov, A. Amato, C. Baines, H.-H. Klauss, E. Morenzoni, D. Johrendt, and H. Luetkens. Coexistence of low-moment magnetism and superconductivity in tetragonal FeS and suppression of T_c under pressure. *Phys. Rev. B* **93**, 140506 (2016).

[111] F. K. K. Kirschner, F. Lang, C. V. Topping, P. J. Baker, F. L. Pratt, S. E. Wright, D. N. Woodruff, S. J. Clarke, and S. J. Blundell. Robustness of superconductivity to competing magnetic phases in tetragonal FeS. *Phys. Rev. B* **94**, 134509 (2016).

[112] S. Kuhn, M. Kidder, D. Parker, C. dela Cruz, M. McGuire, W. Chance, L. Li, L. Debeer-Schmitt, J. Ermentrout, K. Littrell, M. Eskildsen, and A. Sefat. Structure and property correlations in FeS. *Physica C* **534**, 29 (2017).

[113] L. Chauvière, Y. Gallais, M. Cazayous, M. A. Méasson, A. Sacuto, D. Colson, and A. Forget. Raman scattering study of spin-density-wave order and electron-phonon coupling in $Ba(Fe_{1-x}Co_x)_2As_2$. *Phys. Rev. B* **84**, 104508 (2011).

[114] B. Muschler. *Carrier dynamics of $Ba(Fe_{1-x}Co_x)_2As_2$ as a function of doping.* Dissertation, Technische Universität München (2012).

[115] S. Sugai, Y. Mizuno, R. Watanabe, T. Kawaguchi, K. Takenaka, H. Ikuta, Y. Takayanagi, N. Hayamizu, and Y. Sone. Spin-Density-Wave Gap with Dirac Nodes and Two-Magnon Raman Scattering in $BaFe_2As_2$. *J. Phys. Soc. Jpn.* **81**, 024718 (2012).

[116] Y.-X. Yang, Y. Gallais, R. M. Fernandes, I. Paul, L. Chauvière, M.-A. Méasson, M. Cazayous, A. Sacuto, D. Colson, and A. Forget. Raman Scattering as a Probe of Charge Nematic Fluctuations in Iron Based Superconductors. In *Proceedings of the International Conference on Strongly Correlated Electron Systems (SCES2013)*, volume 3 of *JPS Conf. Proc.*, page 015001 (2014). URL `http://dx.doi.org/10.7566/JPSCP.3.015001`.

[117] F. Kretzschmar. *Nematic Fluctuations, Fermiology and the Pairing Potential in Iron-Based Superconductors*. Dissertation, Technische Universität München (2015).

[118] F. Kretzschmar, T. Böhm, U. Karahasanovic, B. Muschler, A. Baum, D. Jost, J. Schmalian, S. Caprara, M. Grilli, C. Di Castro, J. G. Analytis, J.-H. Chu, I. R. Fisher, and R. Hackl. Critical spin fluctuations and the origin of nematic order in $Ba(Fe_{1-x}Co_x)_2As_2$. *Nat. Phys.* **12**, 560 (2016).

[119] Y. Gallais and I. Paul. Charge nematicity and electronic Raman scattering in iron-based superconductors. *C. R. Phys.* **17**, 113 (2016).

[120] T. Böhm, R. Hosseinian Ahangharnejhad, D. Jost, A. Baum, B. Muschler, F. Kretzschmar, P. Adelmann, T. Wolf, H.-H. Wen, J.-H. Chu, I. R. Fisher, and R. Hackl. Superconductivity and fluctuations in $Ba_{1-p}K_pFe_2As_2$ and $Ba(Fe_{1-n}Co_n)_2As_2$. *physica status solidi (b)* **254**, 1600308 (2017).

[121] A. Hinojosa, J. Cai, and A. V. Chubukov. Raman resonance in iron-based superconductors: The magnetic scenario. *Phys. Rev. B* **93**, 075106 (2016).

[122] S.-F. Wu, P. Richard, H. Ding, H.-H. Wen, G. Tan, M. Wang, C. Zhang, P. Dai, and G. Blumberg. Superconductivity and electronic fluctuations in $Ba_{1-x}K_xFe_2As_2$ studied by Raman scattering. *Phys. Rev. B* **95**, 085125 (2017).

[123] Y. Gallais, R. M. Fernandes, I. Paul, L. Chauvière, Y.-X. Yang, M.-A. Méasson, M. Cazayous, A. Sacuto, D. Colson, and A. Forget. Observation of Incipient Charge Nematicity in $Ba(Fe_{1-X}Co_X)_2As_2$. *Phys. Rev. Lett.* **111**, 267001 (2013).

[124] V. K. Thorsmølle, M. Khodas, Z. P. Yin, C. Zhang, S. V. Carr, P. Dai, and G. Blumberg. Critical quadrupole fluctuations and collective modes in iron pnictide superconductors. *Phys. Rev. B* **93**, 054515 (2016).

[125] U. F. Kaneko, P. F. Gomes, A. F. García-Flores, J.-Q. Yan, T. A. Lograsso, G. E. Barberis, D. Vaknin, and E. Granado. Nematic fluctuations and phase transitions in LaFeAsO: A Raman scattering study. *Phys. Rev. B* **96**, 014506 (2017).

[126] P. Massat, D. Farina, I. Paul, S. Karlsson, P. Strobel, P. Toulemonde, M.-A. Méasson, M. Cazayous, A. Sacuto, S. Kasahara, T. Shibauchi, Y. Matsuda, and Y. Gallais. Charge-induced nematicity in FeSe. *Proc. Natl. Acad. Sci.* **113**, 9177 (2016).

[127] M. A. Tanatar, E. C. Blomberg, A. Kreyssig, M. G. Kim, N. Ni, A. Thaler, S. L. Bud'ko, P. C. Canfield, A. I. Goldman, I. I. Mazin, and R. Prozorov. Uniaxial-strain mechanical detwinning of $CaFe_2As_2$ and $BaFe_2As_2$ crystals: Optical and transport study. *Phys. Rev. B* **81**, 184508 (2010).

[128] A. E. Böhmer, P. Burger, F. Hardy, T. Wolf, P. Schweiss, R. Fromknecht, M. Reinecker, W. Schranz, and C. Meingast. Nematic Susceptibility of Hole-Doped and Electron-Doped $BaFe_2As_2$ Iron-Based Superconductors from Shear Modulus Measurements. *Phys. Rev. Lett.* **112**, 047001 (2014).

[129] C. Dhital, T. Hogan, Z. Yamani, R. J. Birgeneau, W. Tian, M. Matsuda, A. S. Sefat, Z. Wang, and S. D. Wilson. Evolution of antiferromagnetic susceptibility under uniaxial pressure in $BaFe_{1-x}Co_x)_2As_2$. *Phys. Rev. B* **89**, 214404 (2014).

[130] H. Luetkens, H.-H. Klauss, M. Kraken, F. J. Litterst, T. Dellmann, R. Klingeler, C. Hess, R. Khasanov, A. Amato, C. Baines, M. Kosmala, O. J. Schumann, M. Braden, J. Hamann-Borrero, N. Leps, A. Kondrat, G. Behr, J. Werner, and B. Büchner. The electronic phase diagram of the $LaO_{1-x}F_xFeAs$ superconductor. *Nat. Mater.* **8**, 305 (2009).

[131] K. Kirshenbaum, S. R. Saha, T. Drye, and J. Paglione. Superconductivity and magnetism in platinum-substituted $SrFe_2As_2$ single crystals. *Phys. Rev. B* **82**, 144518 (2010).

[132] L. Harnagea, S. Singh, G. Friemel, N. Leps, D. Bombor, M. Abdel-Hafiez, A. U. B. Wolter, C. Hess, R. Klingeler, G. Behr, S. Wurmehl, and B. Büchner. Phase diagram of the iron arsenide superconductors $Ca(Fe_{1-x}Co_x)_2As_2(0 \leqslant x \leqslant 0.2)$. *Phys. Rev. B* **83**, 094523 (2011).

[133] C. Lester, J.-H. Chu, J. G. Analytis, S. C. Capelli, A. S. Erickson, C. L. Condron, M. F. Toney, I. R. Fisher, and S. M. Hayden. Neutron scattering study of the interplay between structure and magnetism in $Ba(Fe_{1-x}Co_x)_2As_2$. *Phys. Rev. B* **79**, 144523 (2009).

[134] N. Mannella. The magnetic moment enigma in Fe-based high temperature superconductors. *J. Phys.: Condens. Matter* **26**, 473202 (2014).

[135] W.-J. Hu, H.-H. Lai, S.-S. Gong, R. Yu, A. H. Nevidomskyy, and Q. Si. Frustrated magnetism and quantum transitions of nematic phases in FeSe (2016). arXiv e-print 1606.01235.

[136] P. Bilbao Ergueta, W.-J. Hu, and A. H. Nevidomskyy. Unified spin model for magnetic excitations in iron chalcogenides. *Phys. Rev. B* **96**, 174403 (2017).

[137] K. Liu, Z.-Y. Lu, and T. Xiang. Nematic antiferromagnetic states in bulk FeSe. *Phys. Rev. B* **93**, 205154 (2016).

[138] G. Grüner. *Density waves in Solids.* Addison-Wesley (1994).

[139] R. M. Fernandes and A. J. Millis. Suppression of Superconductivity by Néel-Type Magnetic Fluctuations in the Iron Pnictides. *Phys. Rev. Lett.* **110**, 117004 (2013).

[140] A. Lucarelli, A. Dusza, F. Pfuner, P. Lerch, J. G. Analytis, J.-H. Chu, I. R. Fisher, and L. Degiorgi. Charge dynamics of Co-doped $BaFe_2As_2$. *New J. Phys.* **12**, 073036 (2010).

[141] G. F. Chen, Z. Li, J. Dong, G. Li, W. Z. Hu, X. D. Zhang, X. H. Song, P. Zheng, N. L. Wang, and J. L. Luo. Transport and anisotropy in single-crystalline $SrFe_2As_2$ and $A_{0.6}K_{0.4}Fe_2As_2$ (A = Sr, Ba) superconductors. *Phys. Rev. B* **78**, 224512 (2008).

[142] C. Hess, A. Kondrat, A. Narduzzo, J. E. Hamann-Borrero, R. Klingeler, J. Werner, G. Behr, and B. Büchner. The intrinsic electronic phase diagram of iron-oxypnictide superconductors. *EPL* **87**, 17005 (2009).

[143] K. Okazaki, S. Sugai, S. Niitaka, and H. Takagi. Phonon, two-magnon, and electronic Raman scattering of $Fe_{1+y}Te_{1-x}Se_x$. *Phys. Rev. B* **83**, 035103 (2011).

[144] C.-C. Chen, C. J. Jia, A. F. Kemper, R. R. P. Singh, and T. P. Devereaux. Theory of Two-Magnon Raman Scattering in Iron Pnictides and Chalcogenides. *Phys. Rev. Lett.* **106**, 067002 (2011).

[145] F. Hardy, P. Burger, T. Wolf, R. A. Fisher, P. Schweiss, P. Adelmann, R. Heid, R. Fromknecht, R. Eder, D. Ernst, H. v. Löhneysen, and C. Meingast. Doping evolution of superconducting gaps and electronic densities of states in $Ba(Fe_{1-x}Co_x)_2As_2$ iron pnictides. *EPL* **91**, 47008 (2010).

[146] H. Chen, Y. Ren, Y. Qiu, W. Bao, R. H. Liu, G. Wu, T. Wu, Y. L. Xie, X. F. Wang, Q. Huang, and X. H. Chen. Coexistence of the spin-density wave and superconductivity in $Ba_{1-x}K_xFe_2As_2$. *EPL* **85**, 17006 (2009).

[147] A. E. Böhmer, F. Hardy, L. Wang, T. Wolf, P. Schweiss, and C. Meingast. Superconductivity-induced re-entrance of the orthorhombic distortion in $Ba_{1-x}K_xFe_2As_2$. *Nat. Commun.* **6**, 7911 (2015).

[148] S. Avci, O. Chmaissem, J. M. Allred, S. Rosenkranz, I. Eremin, A. V. Chubukov, D. E. Bugaris, D. Y. Chung, M. G. Kanatzidis, J.-P. Castellan, J. A. Schlueter, H. Claus, D. D. Khalyavin, P. Manuel, A. Daoud-Aladine, and R. Osborn. Magnetically driven suppression of nematic order in an iron-based superconductor. *Nat. Commun.* **5**, 3845 (2014).

[149] T. Yildirim. Strong Coupling of the Fe-Spin State and the As-As Hybridization in Iron-Pnictide Superconductors from First-Principle Calculations. *Phys. Rev. Lett.* **102**, 037003 (2009).

[150] A. Akrap, J. J. Tu, L. J. Li, G. H. Cao, Z. A. Xu, and C. C. Homes. Infrared phonon anomaly in $BaFe_2As_2$. *Phys. Rev. B* **80**, 180502 (2009).

[151] M. Rahlenbeck, G. L. Sun, D. L. Sun, C. T. Lin, B. Keimer, and C. Ulrich. Phonon anomalies in pure and underdoped $R_{1-x}K_xFe_2As_2$ (R = Ba, Sr) investigated by Raman light scattering. *Phys. Rev. B* **80**, 064509 (2009).

[152] L. Chauvière, Y. Gallais, M. Cazayous, A. Sacuto, M. A. Measson, D. Colson, and A. Forget. Doping dependence of the lattice dynamics in $Ba(Fe_{1-x}Co_x)_2As_2$ studied by Raman spectroscopy. *Phys. Rev. B* **80**, 094504 (2009).

[153] A. Baum, H. N. Ruiz, N. Lazarević, Y. Wang, T. Böhm, R. Hosseinian Ahangharnejhad, P. Adelmann, T. Wolf, Z. V. Popović, B. Moritz, T. P. Devereaux,

and R. Hackl. Frustrated spin order and stripe fluctuations in FeSe (2018). arXiv e-print 1709.08998v2.

[154] A. Baum, A. Milosavljević, N. Lazarević, M. M. Radonjić, B. Nikolić, M. Mitschek, Z. I. Maranloo, M. Šćepanović, M. Grujić-Brojčin, N. Stojilović, M. Opel, A. Wang, C. Petrovic, Z. V. Popović, and R. Hackl. Phonon anomalies in FeS. *Phys. Rev. B* **97**, 054306 (2018).

[155] B. Zimmer. *Darstellung und Charakterisierung ternärer Phosphide und quaternärer Phosphid-Oxide der Seltenerdelemente und des Thoriums mit Übergangsmetallen.* Dissertation, Universität Münster (1996).

[156] G. Wu, Y. L. Xie, H. Chen, M. Zhong, R. H. Liu, B. C. Shi, Q. J. Li, X. F. Wang, T. Wu, Y. J. Yan, J. J. Ying, and X. H. Chen. Superconductivity at 56 K in samarium-doped SrFeAsF. *J. Phys.: Condens. Matter* **21**, 142203 (2009).

[157] W. Qing-Yan, L. Zhi, Z. Wen-Hao, Z. Zuo-Cheng, Z. Jin-Song, L. Wei, D. Hao, O. Yun-Bo, D. Peng, C. Kai, W. Jing, S. Can-Li, H. Ke, J. Jin-Feng, J. Shuai-Hua, W. Ya-Yu, W. Li-Li, C. Xi, M. Xu-Cun, and X. Qi-Kun. Interface-Induced High-Temperature Superconductivity in Single Unit-Cell FeSe Films on $SrTiO_3$. *Chin. Phys. Lett.* **29**, 037402 (2012).

[158] P. J. Hirschfeld, M. M. Korshunov, and I. I. Mazin. Gap symmetry and structure of Fe-based superconductors. *Rep. Prog. Phys.* **74**, 124508 (2011).

[159] L. Boeri, O. V. Dolgov, and A. A. Golubov. Is $LaFeAsO_{1-x}F_x$ an Electron-Phonon Superconductor? *Phys. Rev. Lett.* **101**, 026403 (2008).

[160] L. Boeri, M. Calandra, I. I. Mazin, O. V. Dolgov, and F. Mauri. Effects of magnetism and doping on the electron-phonon coupling in $BaFe_2As_2$. *Phys. Rev. B* **82**, 020506 (2010).

[161] T. Hanaguri, S. Niitaka, K. Kuroki, and H. Takagi. Unconventional *s*-Wave Superconductivity in Fe(Se,Te). *Science* **328**, 474 (2010).

[162] M. Xu, Q. Q. Ge, R. Peng, Z. R. Ye, J. Jiang, F. Chen, X. P. Shen, B. P. Xie, Y. Zhang, A. F. Wang, X. F. Wang, X. H. Chen, and D. L. Feng. Evidence for an *s*-wave superconducting gap in $K_xFe_{2-y}Se_2$ from angle-resolved photoemission. *Phys. Rev. B* **85**, 220504 (2012).

[163] X. Yang, Z. Du, G. Du, Q. Gu, H. Lin, D. Fang, H. Yang, X. Zhu, and H.-H. Wen. Strong-coupling superconductivity revealed by scanning tunneling microscope in tetragonal FeS. *Phys. Rev. B* **94**, 024521 (2016).

[164] J. K. Dong, S. Y. Zhou, T. Y. Guan, H. Zhang, Y. F. Dai, X. Qiu, X. F. Wang, Y. He, X. H. Chen, and S. Y. Li. Quantum Criticality and Nodal Superconductivity in the FeAs-Based Superconductor KFe_2As_2. *Phys. Rev. Lett.* **104**, 087005 (2010).

[165] R. Thomale, C. Platt, W. Hanke, J. Hu, and B. A. Bernevig. Exotic *d*-Wave Superconducting State of Strongly Hole-Doped $K_xBa_{1-x}Fe_2As_2$. *Phys. Rev. Lett.* **107**, 117001 (2011).

[166] J.-P. Reid, M. A. Tanatar, A. Juneau-Fecteau, R. T. Gordon, S. R. de Cotret, N. Doiron-Leyraud, T. Saito, H. Fukazawa, Y. Kohori, K. Kihou, C. H. Lee, A. Iyo, H. Eisaki, R. Prozorov, and L. Taillefer. Universal Heat Conduction in the Iron Arsenide Superconductor KFe_2As_2: Evidence of a *d*-Wave State. *Phys. Rev. Lett.* **109**, 087001 (2012).

[167] J. Xing, H. Lin, Y. Li, S. Li, X. Zhu, H. Yang, and H.-H. Wen. Nodal superconducting gap in tetragonal FeS. *Phys. Rev. B* **93**, 104520 (2016).

[168] Y. Yang, W.-S. Wang, H.-Y. Lu, Y.-Y. Xiang, and Q.-H. Wang. Electronic structure and $d_{x^2-y^2}$-wave superconductivity in FeS. *Phys. Rev. B* **93**, 104514 (2016).

[169] F. Kretzschmar, B. Muschler, T. Böhm, A. Baum, R. Hackl, H.-H. Wen, V. Tsurkan, J. Deisenhofer, and A. Loidl. Raman-Scattering Detection of Nearly Degenerate *s*-Wave and *d*-Wave Pairing Channels in Iron-Based $Ba_{0.6}K_{0.4}Fe_2As_2$ and $Rb_{0.8}Fe_{1.6}Se_2$ Superconductors. *Phys. Rev. Lett.* **110**, 187002 (2013).

[170] T. Böhm, A. F. Kemper, B. Moritz, F. Kretzschmar, B. Muschler, H.-M. Eiter, R. Hackl, T. P. Devereaux, D. J. Scalapino, and H.-H. Wen. Balancing Act: Evidence for a Strong Subdominant *d*-Wave Pairing Channel in $Ba_{0.6}K_{0.4}Fe_2As_2$. *Phys. Rev. X* **4**, 041046 (2014).

[171] M. P. Allan, K. Lee, A. W. Rost, M. H. Fischer, F. Massee, K. Kihou, C.-H. Lee, A. Iyo, H. Eisaki, T.-M. Chuang, J. C. Davis, and E.-A. Kim. Identifying the 'fingerprint' of antiferromagnetic spin fluctuations in iron pnictide superconductors. *Nat. Phys.* **11**, 177 (2014).

[172] Q. Si, R. Yu, and E. Abrahams. High-temperature superconductivity in iron pnictides and chalcogenides. *Nat. Rev. Mater.* **1**, 16017 (2016).

[173] P. Dai. Antiferromagnetic order and spin dynamics in iron-based superconductors. *Rev. Mod. Phys.* **87**, 855 (2015).

[174] T. Devereaux and R. Hackl. Inelastic light scattering from correlated electrons. *Rev. Mod. Phys.* **79**, 175 (2007).

[175] A. Smekal. Zur Quantentheorie der Dispersion. *Naturwissenschaften* **11**, 873 (1923).

[176] H. Kramers and W. Heisenberg. Über die Streuung von Strahlung durch Atome. *Z. Phys.* **31**, 681 (1925).

[177] G. Landsberg and L. Mandelstam. Eine neue Erscheinung bei der Lichtzerstreuung in Krystallen. *Naturwissenschaften* **16**, 557 (1928).

[178] C. V. Raman and K. Krishnan. A New Type of Secondary Radiation. *Nature* **121**, 501 (1928).

[179] W. Hayes and R. Loudon. *Scattering of Light by Crystals.* John Wiley ans Sons, New York (1978).

[180] J. L. Birman. Scattering tensors for "forbidden" resonance Raman scattering in cubic crystals. *Phys. Rev. B* **9**, 4518 (1974).

[181] S. Caprara, C. Di Castro, M. Grilli, and D. Suppa. Charge-Fluctuation Contribution to the Raman Response in Superconducting Cuprates. *Phys. Rev. Lett.* **95**, 117004 (2005).

[182] C. Hoffmann. Diplomarbeit, Technische Universität München (1997).

[183] T. Böhm. *Raman-Streuung an unkonventionellen Supraleitern.* Diplomarbeit, Technische Universität München (2012).

[184] R. Hackl. *Inelastische Lichtstreuung an A15-Verbindungen.* Dissertation, Technische Universität München (1987).

[185] F. Venturini. *Raman Scattering Study of Electronic Correlations in Cuprates: Observation of an Unconventional Metal-Insulator Transition.* Dissertation, Technische Universität München (2003).

[186] W. Prestel. *Study of the Interaction Processes in Cuprate Superconductors by a Quantitative Comparison of Spectroscopic Experiments.* Dissertation, Technische Universität München (2012).

[187] R. Roßner. *Untersuchung von korrelierten Elektronensystemen unter hohem Druck.* Diplomarbeit, Technische Universität München (2010).

[188] A. Walter. *Untersuchung von $BaFe_2As_2$ unter hydrostatischem Druck.* Masterarbeit, Technische Universität München (2014).

[189] A. Wang, L. Wu, V. N. Ivanovski, J. B. Warren, J. Tian, Y. Zhu, and C. Petrovic. Critical current density and vortex pinning in tetragonal $FeS_{1-x}Se_x$ ($x = 0, 0.06$). *Phys. Rev. B* **94**, 094506 (2016).

[190] A. Williams, T. McQueen, and R. Cava. The stoichiometry of FeSe. *Solid State Commun.* **149**, 1507 (2009).

[191] D. Jost. *Phononen in entzwillingtem $BaFe_2As_2$.* Bachelorarbeit, Technische Universität München (2013).

[192] F. Löffler. *Anisotropie- und Resonanzverhalten des A_g-Phonons in $BaFe_2As_2$.* Masterarbeit, Technische Universität München (2018).

[193] A. Charnukha, D. Pröpper, T. I. Larkin, D. L. Sun, Z. W. Li, C. T. Lin, T. Wolf, B. Keimer, and A. V. Boris. Spin-density-wave-induced anomalies in the optical conductivity of $A Fe_2As_2$, (A = Ca, Sr, Ba) single-crystalline iron pnictides. *Phys. Rev. B* **88**, 184511 (2013).

[194] A. Özkü. *Untersuchung von $BaFe_2As_2$ unter dem Einfluss von uniaxialem Druck.* Bachelorarbeit, Technische Universität München (2013).

[195] Y. J. Um, A. Subedi, P. Toulemonde, A. Y. Ganin, L. Boeri, M. Rahlenbeck, Y. Liu, C. T. Lin, S. J. E. Carlsson, A. Sulpice, M. J. Rosseinsky, B. Keimer, and M. Le Tacon. Anomalous dependence of c-axis polarized Fe B_{1g} phonon mode with Fe and Se concentrations in $Fe_{1+y}Te_{1-x}Se_x$. *Phys. Rev. B* **85**, 064519 (2012).

[196] V. Gnezdilov, Y. Pashkevich, P. Lemmens, A. Gusev, K. Lamonova, T. Shevtsova, I. Vitebskiy, O. Afanasiev, S. Gnatchenko, V. Tsurkan, J. Deisenhofer, and A. Loidl. Anomalous optical phonons in FeTe chalcogenides: Spin state, magnetic order, and lattice anharmonicity. *Phys. Rev. B* **83**, 245127 (2011).

[197] Z. Popović, N. Lazarević, S. Bogdanović, M. Radonjić, D. Tanasković, R. Hu, H. Lei, and C. Petrovic. Signatures of the spin-phonon coupling in $Fe_{1+y}Te_{1-x}Se_x$ alloys. *Solid State Commun.* **193**, 51 (2014).

[198] Z. An-Min and Z. Qing-Ming. Electron-phonon coupling in cuprate and iron-based superconductors revealed by Raman scattering. *Chinese Physics B* **22**, 087103 (2013).

[199] M. Opačić, N. Lazarević, M. Šćepanović, H. Ryu, H. Lei, C. Petrovic, and Z. V. Popović. Evidence of superconductivity-induced phonon spectra renormalization in alkali-doped iron selenides. *J. Phys.: Condens. Matter* **27**, 485701 (2015).

[200] M. R. Opačić and N. v. Lazarević. Lattice dynamics of iron chalcogenides: Raman scattering study. *J. Serb. Chem. Soc.* **82**, 957 (2017).

[201] Y. Hu, X. Ren, R. Zhang, H. Luo, S. Kasahara, T. Watashige, T. Shibauchi, P. Dai, Y. Zhang, Y. Matsuda, and Y. Li. Nematic magnetoelastic effect contrasted between $Ba(Fe_{1-x}Co_x)_2As_2$ and FeSe. *Phys. Rev. B* **93**, 060504 (2016).

[202] L. Yue, X. Ren, T. Han, J. Guo, Z. Wu, Y. Zhang, and Y. Li. Raman scattering study of the tetragonal magnetic phase in $Sr_{1-x}Na_xFe_2As_2$: Structural symmetry and electronic gap. *Phys. Rev. B* **96**, 180505 (2017).

[203] M. I. Aroyo, A. Kirov, C. Capillas, J. M. Perez-Mato, and H. Wondratschek. Bilbao Crystallographic Server. II. Representations of crystallographic point groups and space groups. *Acta Crystallogr. A* **62**, 115 (2006).

[204] P. G. Klemens. Anharmonic Decay of Optical Phonons. *Phys. Rev.* **148**, 845 (1966).

[205] H.-M. Eiter, P. Jaschke, R. Hackl, A. Bauer, M. Gangl, and C. Pfleiderer. Raman study of the temperature and magnetic-field dependence of the electronic and lattice properties of MnSi. *Phys. Rev. B* **90**, 024411 (2014).

[206] R. A. MacDonald and W. M. MacDonald. Thermodynamic properties of fcc metals at high temperatures. *Phys. Rev. B* **24**, 1715 (1981).

[207] M. I. Aroyo, D. Orobengoa, G. de la Flor, E. S. Tasci, J. M. Perez-Mato, and H. Wondratschek. Brillouin-zone database on the *Bilbao Crystallographic Server*. *Acta Crystallogr. A* **70**, 126 (2014).

[208] W. Spengler and R. Kaiser. First and second order Raman scattering in transition metal compounds. *Solid State Commun.* **18**, 881 (1976).

[209] L. Rettig, R. Cortés, H. S. Jeevan, P. Gegenwart, T. Wolf, J. Fink, and U. Bovensiepen. Electron-phonon coupling in 122 Fe pnictides analyzed by femtosecond time-resolved photoemission. *New J. Phys.* **15**, 083023 (2013).

[210] B. Mansart, D. Boschetto, A. Savoia, F. Rullier-Albenque, F. Bouquet, E. Papalazarou, A. Forget, D. Colson, A. Rousse, and M. Marsi. Ultrafast transient response and electron-phonon coupling in the iron-pnictide superconductor $Ba(Fe_{1-x}Co_x)_2As_2$. *Phys. Rev. B* **82**, 024513 (2010).

[211] H. Martinho, C. Rettori, P. Pagliuso, A. Martin, N. Moreno, and J. Sarrao. Role of the E_{2g} phonon in the superconductivity of MgB_2: a Raman scattering study. *Solid State Commun.* **125**, 499 (2003).

[212] Y. Wang, T. Plackowski, and A. Junod. Specific heat in the superconducting and normal state (2-300 K, 0-16 T), and magnetic susceptibility of the 38 K superconductor MgB_2: evidence for a multicomponent gap. *Physica C* **355**, 179 (2001).

[213] T. P. Ying, X. F. Lai, X. C. Hong, Y. Xu, L. P. He, J. Zhang, M. X. Wang, Y. J. Yu, F. Q. Huang, and S. Y. Li. Nodal superconductivity in FeS: Evidence from quasiparticle heat transport. *Phys. Rev. B* **94**, 100504 (2016).

[214] Y. J. Um, J. T. Park, B. H. Min, Y. J. Song, Y. S. Kwon, B. Keimer, and M. Le Tacon. Raman scattering study of the lattice dynamics of superconducting LiFeAs. *Phys. Rev. B* **85**, 012501 (2012).

[215] V. Gnezdilov, Y. G. Pashkevich, P. Lemmens, D. Wulferding, T. Shevtsova, A. Gusev, D. Chareev, and A. Vasiliev. Interplay between lattice and spin states degree of freedom in the FeSe superconductor: Dynamic spin state instabilities. *Phys. Rev. B* **87**, 144508 (2013).

[216] K. D. Kwon, K. Refson, S. Bone, R. Qiao, W.-l. Yang, Z. Liu, and G. Sposito. Magnetic ordering in tetragonal FeS: Evidence for strong itinerant spin fluctuations. *Phys. Rev. B* **83**, 064402 (2011).

[217] X. Ren, L. Duan, Y. Hu, J. Li, R. Zhang, H. Luo, P. Dai, and Y. Li. Nematic Crossover in $BaFe_2As_2$ under Uniaxial Stress. *Phys. Rev. Lett.* **115**, 197002 (2015).

[218] W.-L. Zhang, A. S. Sefat, H. Ding, P. Richard, and G. Blumberg. Stress-induced nematicity in $EuFe_2As_2$ studied by Raman spectroscopy. *Phys. Rev. B* **94**, 014513 (2016).

[219] A. P. Litvinchuk, V. G. Hadjiev, M. N. Iliev, B. Lv, A. M. Guloy, and C. W. Chu. Raman-scattering study of $K_xSr_{1-x}Fe_2As_2$ (x = 0.0,0.4). *Phys. Rev. B* **78**, 060503 (2008).

[220] M. Zbiri, H. Schober, M. R. Johnson, S. Rols, R. Mittal, Y. Su, M. Rotter, and D. Johrendt. Ab initio lattice dynamics simulations and inelastic neutron scattering spectra for studying phonons in $BaFe_2As_2$: Effect of structural phase transition, structural relaxation, and magnetic ordering. *Phys. Rev. B* **79**, 064511 (2009).

[221] S.-F. Wu, W.-L. Zhang, V. K. Thorsmølle, G. F. Chen, G. T. Tan, P. C. Dai, Y. G. Shi, C. Q. Jin, T. Shibauchi, S. Kasahara, Y. Matsuda, A. S. Sefat, H. Ding, P. Richard, and G. Blumberg. Magneto-elastic coupling in Fe-based superconductors (2017). arXiv e-print 1712.01896.

[222] K.-Y. Choi, D. Wulferding, P. Lemmens, N. Ni, S. L. Bud'ko, and P. C. Canfield. Lattice and electronic anomalies of $CaFe_2As_2$ studied by Raman spectroscopy. *Phys. Rev. B* **78**, 212503 (2008).

[223] L. Chauvière, Y. Gallais, M. Cazayous, M. A. Méasson, A. Sacuto, D. Colson, and A. Forget. Impact of the spin-density-wave order on the superconducting gap of $Ba(Fe_{1-x}Co_x)_2As_2$. *Phys. Rev. B* **82**, 180521 (2010).

[224] M. Cardona. *Resonance Phenomena*, volume 50 of *Light Scattering in Solids*, chapter 2, pages 19–178. Springer-Verlag Berlin Heidelberg, Berlin, Heidelberg, 1 edition (1982). ISBN 978-3-540-39075-6. URL `http://dx.doi.org/10.1007/3-540-11380-0_14`.

[225] C. Ambrosch-Draxl, H. Auer, R. Kouba, E. Y. Sherman, P. Knoll, and M. Mayer. Raman scattering in $YBa_2Cu_3O_7$: A comprehensive theoretical study in comparison with experiments. *Phys. Rev. B* **65**, 064501 (2002).

[226] T. Strach, J. Brunen, B. Lederle, J. Zegenhagen, and M. Cardona. Determination of the phase difference between the Raman tensor elements of the A_{1g}-like phonons in $SmBa_2Cu_3O_{7-\delta}$. *Phys. Rev. B* **57**, 1292 (1998).

[227] S. L. Skornyakov, A. V. Efremov, N. A. Skorikov, M. A. Korotin, Y. A. Izyumov, V. I. Anisimov, A. V. Kozhevnikov, and D. Vollhardt. Classification of the electronic correlation strength in the iron pnictides: The case of the parent compound $BaFe_2As_2$. *Phys. Rev. B* **80**, 092501 (2009).

[228] Y. X. Yao, J. Schmalian, C. Z. Wang, K. M. Ho, and G. Kotliar. Comparative study of the electronic and magnetic properties of $BaFe_2As_2$ and $BaMn_2As_2$ using the Gutzwiller approximation. *Phys. Rev. B* **84**, 245112 (2011).

[229] J. Ferber, K. Foyevtsova, R. Valentí, and H. O. Jeschke. LDA + DMFT study of the effects of correlation in LiFeAs. *Phys. Rev. B* **85**, 094505 (2012).

[230] S. Backes, H. O. Jeschke, and R. Valentí. Microscopic nature of correlations in multiorbital AFe_2As_2 (A=K, Rb, Cs: Hund's coupling versus Coulomb repulsion. *Phys. Rev. B* **92**, 195128 (2015).

[231] N. A. García-Martínez, B. Valenzuela, S. Ciuchi, E. Cappelluti, M. J. Calderón, and E. Bascones. Coupling of the As A_{1g} phonon to magnetism in iron pnictides. *Phys. Rev. B* **88**, 165106 (2013).

[232] N. Chelwani, A. Baum, T. Böhm, M. Opel, F. Venturini, L. Tassini, A. Erb, H. Berger, L. Forró, and R. Hackl. Magnetic excitations and amplitude fluctuations in insulating cuprates. *Phys. Rev. B* **97**, 024407 (2018).

[233] C. M. Canali and S. M. Girvin. Theory of Raman scattering in layered cuprate materials. *Phys. Rev. B* **45**, 7127 (1992).

[234] S. A. Weidinger and W. Zwerger. Higgs mode and magnon interactions in 2D quantum antiferromagnets from Raman scattering. *Eur. Phys. J. B* **88**, 237 (2015).

[235] Y.-X. Yang, Y. Gallais, F. Rullier-Albenque, M.-A. Méasson, M. Cazayous, A. Sacuto, J. Shi, D. Colson, and A. Forget. Temperature-induced change in the Fermi surface topology in the spin density wave phase of $Sr(Fe_{1-x}Co_x)_2As_2$. *Phys. Rev. B* **89**, 125130 (2014).

[236] Q. Wang, Y. Shen, B. Pan, X. Zhang, K. Ikeuchi, K. Iida, A. D. Christianson, H. C. Walker, D. T. Adroja, M. Abdel-Hafiez, X. Chen, D. A. Chareev, A. N. Vasiliev, and J. Zhao. Magnetic ground state of FeSe. *Nat. Commun.* **7**, 12182 (2016).

[237] N. S. Headings, S. M. Hayden, R. Coldea, and T. G. Perring. Anomalous High-Energy Spin Excitations in the High-T_c Superconductor-Parent Antiferromagnet La_2CuO_4. *Phys. Rev. Lett.* **105**, 247001 (2010).

[238] J. Knolle, G.-W. Chern, D. L. Kovrizhin, R. Moessner, and N. B. Perkins. Raman Scattering Signatures of Kitaev Spin Liquids in A_2IrO_3 Iridates with A = Na or Li. *Phys. Rev. Lett.* **113**, 187201 (2014).

[239] R. Moessner and A. P. Ramirez. Geometrical frustration. *Phys. Today* **59**, 24 (2006).

[240] H. Q. Lin. Exact diagonalization of quantum-spin models. *Phys. Rev. B* **42**, 6561 (1990).

[241] E. Dagotto. Correlated electrons in high-temperature superconductors. *Rev. Mod. Phys.* **66**, 763 (1994).

[242] M. I. Eremets. *High Pressure Experimental Methods*. Oxford Science Publications. Oxford University Press, USA (1996). ISBN 0198562691.

[243] S. A. J. Kimber, A. Kreyssig, Y.-Z. Zhang, H. O. Jeschke, R. Valenti, F. Yokaichiya, E. Colombier, J. Yan, T. C. Hansen, T. Chatterji, R. J. McQueeney, P. C. Canfield, A. I. Goldman, and D. N. Argyriou. Similarities between structural distortions under pressure and chemical doping in superconducting $BaFe_2As_2$. *Nat. Mater.* **8**, 471 (2009).

[244] S. Drotziger, P. Schweiss, K. Grube, T. Wolf, P. Adelmann, C. Meingast, and H. v. Löhneysen. Pressure versus Concentration Tuning of the Superconductivity in $Ba(Fe_{1-x}Co_x)_2As_2$. *J. Phys. Soc. Jpn.* **79**, 124705 (2010).

[245] K. Kothapalli, A. E. Böhmer, W. T. Jayasekara, B. G. Ueland, P. Das, A. Sapkota, V. Taufour, Y. Xiao, E. Alp, S. L. Bud'ko, P. C. Canfield, A. Kreyssig, and A. I. Goldman. Strong cooperative coupling of pressure-induced magnetic order and nematicity in FeSe. *Nat. Commun.* **7**, 12728 (2016).

[246] U. Zweck. *Electronic and magnetic excitations in underdoped* $YBa_2Cu_3O_{6+x}$. Masterarbeit, Technische Universität München (2018).

[247] H.-M. Eiter. *Carrier and Lattice Dynamics in Systems with Charge and Spin Order*. Dissertation, Technische Universität München (2014).

[248] R. A. Forman, G. J. Piermarini, J. D. Barnett, and S. Block. Pressure Measurement Made by the Utilization of Ruby Sharp-Line Luminescence. *Science* **176**, 284 (1972).

[249] A. Jayaraman. Diamond anvil cell and high-pressure physical investigations. *Rev. Mod. Phys.* **55**, 65 (1983).

[250] L. Tassini. *Charge ordering phenomena and superconductivity in underdoped cuprates*. Dissertation, Technische Universität München (2008).

[251] M. Mitschek. *Magnetismus und Supraleitung in Eisenchalkogeniden*. Masterarbeit, Technische Universität München (2017).

[252] P. Massat, Y. Quan, R. Grasset, M.-A. Méasson, M. Cazayous, A. Sacuto, S. Karlsson, P. Strobel, P. Toulemonde, Z. Yin, and Y. Gallais. Collapse of Critical Nematic Fluctuations in FeSe under Pressure. *Phys. Rev. Lett.* **121**, 077001 (2018).

[253] J.-E. Jørgensen, J. S. Olsen, and L. Gerward. On the compressibility of $BaFe_2As_2$. *Solid State Commun.* **149**, 1161 (2009).

[254] R. Mittal, S. K. Mishra, S. L. Chaplot, S. V. Ovsyannikov, E. Greenberg, D. M. Trots, L. Dubrovinsky, Y. Su, T. Brueckel, S. Matsuishi, H. Hosono, and G. Garbarino. Ambient- and low-temperature synchrotron x-ray diffraction study of $BaFe_2As_2$ and $CaFe_2As_2$ at high pressures up to 56 GPa. *Phys. Rev. B* **83**, 054503 (2011).

[255] W. Uhoya, A. Stemshorn, G. Tsoi, Y. K. Vohra, A. S. Sefat, B. C. Sales, K. M. Hope, and S. T. Weir. Collapsed tetragonal phase and superconductivity of $BaFe_2As_2$ under high pressure. *Phys. Rev. B* **82**, 144118 (2010).

[256] K. Ahilan, F. L. Ning, T. Imai, A. S. Sefat, M. A. McGuire, B. C. Sales, and D. Mandrus. Electronic phase diagram of the iron-based high-T_c superconductor $Ba(Fe_{1-x}Co_x)_2As_2$ under hydrostatic pressure ($0 \leq x \leq 0.099$). *Phys. Rev. B* **79**, 214520 (2009).

[257] H. Fukazawa, N. Takeshita, T. Yamazaki, K. Kondo, K. Hirayama, Y. Kohori, K. Miyazawa, H. Kito, H. Eisaki, and A. Iyo. Suppression of Magnetic Order by Pressure in $BaFe_2As_2$. *J. Phys. Soc. Jpn.* **77**, 105004 (2008).

[258] K. Matsubayashi, N. Katayama, K. Ohgushi, A. Yamada, K. Munakata, T. Matsumoto, and Y. Uwatoko. Intrinsic Properties of AFe$_2$As$_2$ (A = Ba, Sr) Single Crystal under Highly Hydrostatic Pressure Conditions. *J. Phys. Soc. Jpn.* **78**, 073706 (2009).

[259] W. Ji, X.-W. Yan, and Z.-Y. Lu. Pressure- and temperature-induced structural phase transitions of CaFe$_2$As$_2$ and BaFe$_2$As$_2$ studied in the Hund's rule correlation picture. *Phys. Rev. B* **83**, 132504 (2011).

[260] S. Kasahara, H. J. Shi, K. Hashimoto, S. Tonegawa, Y. Mizukami, T. Shibauchi, K. Sugimoto, T. Fukuda, T. Terashima, A. H. Nevidomskyy, and Y. Matsuda. Electronic nematicity above the structural and superconducting transition in BaFe$_2$(As$_{1-x}$P$_x$)$_2$. *Nature* **486**, 382 (2012).

[261] S. Kasahara, T. Shibauchi, K. Hashimoto, K. Ikada, S. Tonegawa, R. Okazaki, H. Shishido, H. Ikeda, H. Takeya, K. Hirata, T. Terashima, and Y. Matsuda. Evolution from non-Fermi- to Fermi-liquid transport via isovalent doping in BaFe$_2$(As$_{1-x}$P$_x$)$_2$ superconductors. *Phys. Rev. B* **81**, 184519 (2010).

[262] T. Shibauchi, A. Carrington, and Y. Matsuda. A Quantum Critical Point Lying Beneath the Superconducting Dome in Iron Pnictides. *Annu. Rev. Cond. Mat. Phys.* **5**, 113 (2014).

[263] L. E. Klintberg, S. K. Goh, S. Kasahara, Y. Nakai, K. Ishida, M. Sutherland, T. Shibauchi, Y. Matsuda, and T. Terashima. Chemical Pressure and Physical Pressure in BaFe$_2$(As$_{1-x}$P$_x$)$_2$. *J. Phys. Soc. Jpn.* **79**, 123706 (2010).

[264] U. Ralević, N. Lazarević, A. Baum, H.-M. Eiter, R. Hackl, P. Giraldo-Gallo, I. R. Fisher, C. Petrovic, R. Gajić, and Z. V. Popović. Charge density wave modulation and gap measurements in CeTe$_3$. *Phys. Rev. B* **94**, 165132 (2016).

[265] S. Djurdjić-Mijin, A. Šolajić, J. Pešić, M. Šćepanović, Y. Liu, A. Baum, C. Petrovic, N. Lazarević, and Z. V. Popović. Lattice dynamics and phase transition in CrI$_3$ single crystals (2018). arXiv e-print 1807.03259v1.

Acknowledgements

Teamwork paves the way to success and hence I'd like to express my gratitude to everyone who supported me during my work. I am indebted to

- Priv. Doz. Dr. Rudi Hackl for supervising this thesis, for introducing me to Raman spectroscopy and scientific work, for his help with words and deeds regarding all lab problems, and for the good teamwork that I could enjoy while working at the WMI for a decade now.
- Prof. Dr. Rudolf Gross for giving me the opportunity to do my doctor's degree at the Walther Meissner Institute.
- Dr. Nenad Lazarević for our prolific joint work and for friendship beyond scientific collaboration.
- our collaborators on all publications for our fruitful joint work; especially Dr. Ying Li and Prof. Dr. Roser Valentí from Frankfurt; Harrison N. Ruiz, Dr. Brian Moritz, and Prof. Dr. Thomas P. Devereaux from Stanford; and Ana Milosavljević and Milos M. Radonjić from Belgrade.
- my colleagues of the Raman group, especially Dr. Thomas Böhm for his friendship since undergraduate times, Dr. Bernhard Muschler for his thorough and patient introduction to the lab, Dr. Hans-Martin Eiter for introducing me to the high pressure technique, and Daniel Jost for proofreading this thesis.
- all Bachelor, Master and working students who contributed a lot to the measurements and technical work.
- Dr. Thomas Wolf, Prof. I. R. Fisher, Prof. C. Petrovic and their groups for providing the high quality samples which are crucial for good experiments.
- Dr. Matthias Opel, Peter Eder, and Dieter Guratzsch for our successful work on keeping the institute's IT systems up and running.

- Prof. Dr. Zoran Popović for his hospitality during my stay in Belgrade.
- my colleagues Karen Helm-Knapp and Astrid Habel for the good atmosphere in our office, for assistance for chemical and technical issues, and for a view of the world beyond the lab.
- the craftsmen of the WMI workshop for quickly creating and fixing many parts of the lab setup that were 'needed yesterday'.
- our lab technicians Sebastian Kammerer and Joachim Geismann for all the help in finding the one connector that is always missing in complex set-ups.
- the staff of the TUM crystal laboratory, especially Susanne Mayr, for the accurate sample preparation.
- the electric engineers of the WMI, Ulrich Guggenberger, Sigi Wanninger, and Christoph Kastl, for their help whenever electrons were not moving as intended.
- the technicians of the He liquefaction for many short-term solutions to keep the cryostats operational.
- Emel Dönertas and Ludwig Ossiander for their help that made all paperwork a lot easier.
- Dr. Michael Kunz for several helpful technical discussions and for initiating the recreational 'Spieleabend'.
- my family who supported me at all times, especially when times were tough.